



HAROKOPIO UNIVERSITY

SCHOOL OF DIGITAL TECHNOLOGY  
DEPARTMENT OF INFORMATICS AND TELEMATICS

**Modeling and design of coupled racetrack and microring structures for  
telecommunication and sensing applications**

Ph.D. Dissertation  
**Leonidas Dogkas**

Athens, 2019

**HAROKOPIO UNIVERSITY**  
**SCHOOL OF DIGITAL TECHNOLOGY**  
**DEPARTMENT OF INFORMATICS AND TELEMATICS**

This dissertation was examined by the following examination committee:

**Thomas Kamalakis, (Supervisor)**

**Associate Professor, Department of Informatics and Telematics, Harokopio  
University**

**Maria Nikolaidou (Advisory committee)**

**Professor, Department of Informatics and Telematics, Harokopio University**

**Georgios Dimitrakopoulos (Advisory committee)**

**Assistant Professor, Department of Informatics and Telematics, Harokopio  
University**

**Nikos Stathopoulos**

**Professor, Department of Electrical and Electronics Engineering, University  
of West Attica**

**Antonis Bogris**

**Professor, Department of Informatics and Computer Engineering,  
University of West Attica**

**Dimitris Alexandropoulos**

**Assistant Professor, Department of Material Science, University of Patras**

**Christina Politi**

**Assistant Professor, Department of Telecommunications Science and  
Technology, University of Peloponnese**

The acceptance of the Ph.D. Dissertation from the Department of Informatics and Telematics of Harokopio University does not imply the acceptance of the author's point of view.

Me, the author of this document, Leonidas Dogkas, solemnly declare that:

1. I am the owner of the copyrights of this original work and this work does not defame any person, neither offend the copyrights of others.
2. I accept that the Library of the Harokopio University can change the contents of this work, deliver this work in electronic format through the Institutional Repository, copy this work using to any format or media and keep more than one copies for maintainability or security reasons.

## **Dedication**

To my wife Olga and daughter Lida.

## **Acknowledgements**

I would like to express my deep gratitude to my supervisor Assoc. Prof. Thomas Kamalakis for his patient guidance, advice, encouragement and continuous efforts on this Ph.D. study. I would not have completed this thesis without his help and support.

I would also like to thank Assist. Prof. Dimitrios Alexandropoulos, for his precise and accurate advice, especially in the research field of sensors, whenever I needed it.

My grateful thanks are also extended to Dr. Panagiotis Kanakis for his valuable contribution to our common research effort on microring resonators.

I am also grateful to my wife Olga, for her love and support especially at the last years of this effort, where the time I could spend with her was limited.

Finally, I would like to thank my parents and brothers for their support and encouragement throughout my study all of these years.

# Contents

<b>1</b>	<b>Foreword</b>	<b>19</b>
1.1	Purpose of the thesis . . . . .	19
1.2	Outline of the thesis . . . . .	21
<b>2</b>	<b>Introduction</b>	<b>22</b>
2.1	Optical communications systems . . . . .	22
2.2	Optical add-drop multiplexers . . . . .	23
2.3	Optical sensors . . . . .	25
2.4	Integrated optics and material platforms . . . . .	27
2.5	Optical waveguides . . . . .	29
2.5.1	Waveguide structure and materials . . . . .	29
2.5.2	Electromagnetic analysis . . . . .	32
2.6	Optical resonators . . . . .	34
2.7	Microring resonators . . . . .	37
2.8	Multiple resonator structures . . . . .	38
2.9	Applications of MRs . . . . .	39
2.10	Racetrack resonators . . . . .	43
<b>3</b>	<b>Design and simulation tools</b>	<b>45</b>
3.1	Introduction . . . . .	45
3.2	Reciprocity relations . . . . .	46
3.3	Coupled mode theory . . . . .	47
3.4	Power flow . . . . .	50
3.5	Lossless coupling region . . . . .	51
3.6	Transfer function calculation . . . . .	53
3.7	Finite difference frequency domain method . . . . .	57

3.7.1	Yee's grid . . . . .	57
3.7.2	Eigenvalue problems . . . . .	59
3.7.3	Boundary conditions and averaging . . . . .	61
3.7.4	Application of the FDFD method . . . . .	62
3.8	Finite difference time domain method analysis . . . . .	64
3.8.1	Yee's grid in 3D . . . . .	64
3.8.2	Perfectly matched layers . . . . .	67
3.8.3	2D structures . . . . .	71
3.9	FDTD in MR structures . . . . .	72
<b>4</b>	<b>Designing MR structures</b>	<b>75</b>
4.1	CMT framework . . . . .	77
4.2	Minimization metric . . . . .	80
4.3	Results and discussion . . . . .	82
4.4	Conclusions . . . . .	88
<b>5</b>	<b>Designing RR structures</b>	<b>89</b>
5.1	Transfer matrix analysis . . . . .	89
5.1.1	Transfer matrix elements approximations . . . . .	91
5.2	Transfer function model . . . . .	94
5.3	Symmetric resonances . . . . .	97
5.3.1	Fano resonance tailoring in the symmetric case . . . . .	98
5.4	Non-symmetric case . . . . .	101
5.5	Relating the design and structural parameters . . . . .	104
5.5.1	Gain parameters . . . . .	104
5.5.2	Structural parameters . . . . .	106
5.6	RR/waveguide structure design . . . . .	106
5.6.1	Metric and restrictions definition . . . . .	107

5.6.2	Design characterization . . . . .	108
5.6.3	Results and discussion . . . . .	109
5.7	Conclusions . . . . .	114
<b>6</b>	<b>Conclusions and outlook</b>	<b>115</b>
6.1	Contribution of this thesis . . . . .	115
6.2	Outlook . . . . .	116
6.3	Thesis publications . . . . .	118

## Abstract

The purpose of this PhD thesis is to present methods of optimally designing microring resonators as well as racetrack resonators for their use in optical filter and optical sensing applications respectively. Using various extensions of the modeling techniques already applied in the literature, namely an alternative form of coupled mode theory (CMT), the transfer matrix method (TMM), we came up with accurate analytical and semi/analytical model for the device transfer function that are more easily applicable, using considerably less resources and time compared to existing models found in literature. We then proposed figure of merits for characterizing the performance of the design in order to finally find the optimal design through optimization techniques.

Initially we considered the optimal microring resonator design case for use in optical filtering applications. Due to the increased number of input parameters in our model, we used an interior point algorithm optimization method, which converts the original minimization problem of figure of merit in a series of similar minimization problems based solely on equalities and other constraints. Such problems are more easily solved by the use of methods such as conjugate gradient etc., the analysis of which is out of the scope of this thesis. The figure of merit we chose in this case was analogous to the difference of our layout transfer function from a sixth degree Gaussian function, which is considered an ideal transfer function for use in filters.

On the other hand, in the case of optimal design of racetrack resonator devices for use in optical sensing applications, where the input parameters of our model are limited in number, we opted to use the exhaustive search method while checking for any restrictions we initially set. With this procedure, if the constraints are satisfied, we calculate the figure of merit for each combination of values and store these values. During the exhaustive search, we keep the combination of parameters for which we calculated the minimum value for the figure of merit, which in this case is proportional to the frequency range of the detection area.

At this point it should be emphasized that in both of the above cases the range of input parameters of our models was chosen in such a way that it is possible to implement the calculated layout based on the state-of-the-art materials and manufacturing methods. Even if these change in the future, with the discovery of new materials and methods, our model can also support them simply by varying the range of input parameters.

After completing our calculations, we came up with optical filters and optical detectors with improved features over the existing ones in the literature, which can be implemented using the materials and manufacturing methods available today.

**Keywords:** Microring Resonators, Racetrack Resonators, Filters, Sensors

## Περίληψη

Σκοπός της Διδακτορικής αυτής διατριβής είναι η παρουσίαση μεθόδων βέλτιστης σχεδίασης διατάξεων συντονιστών μικροδακτυλίων αλλά και συντονιστών τύπου racetrack με στόχο τη χρήση τους σε εφαρμογές οπτικών φίλτρων και οπτικών αισθητήρων αντίστοιχα. Με τη χρήση απλοποιήσεων και προσεγγίσεων στα μαθηματικά μοντέλα που ήδη εφαρμόζονται στη βιβλιογραφία και συγκεκριμένα της εναλλακτικής μορφής της μεθόδου coupled mode theory (CMT), την transfer matrix method (TMM), καταλήξαμε σε μορφές των συναρτήσεων μεταφοράς οι οποίες είναι ευκολότερα χρησιμοποιήσιμες, κερδίζοντας έτσι πόρους και χρόνο συγκριτικά με τα ήδη υπάρχοντα μοντέλα της βιβλιογραφίας. Στη συνέχεια χρησιμοποιήσαμε έναν μαθηματικό τύπο τον οποίο υπολογίσαμε, ως μέτρο ποιότητας (figure of merit) της διάταξής μας, διαφορετικό για κάθε τύπο διάταξης, ώστε να καταλήξουμε στη βέλτιστη σχεδίαση της διάταξής μας. Το figure of merit είναι μιά παράμετρος η τιμή της οποίας είναι αντιστρόφως ανάλογη με την ποιότητα της διάταξής μας, δηλαδή μια τιμή την οποία θέλουμε ιδανικά να μηδενίσουμε.

Αρχικά για την περίπτωση της σχεδίασης της βέλτιστης διάταξης συντονιστών μικροδακτυλίου για χρήση σε εφαρμογές οπτικών φίλτρων, λόγω του αυξημένου αριθμού των παραμέτρων εισόδου του μοντέλου μας, κάναμε χρήση μεθόδου βελτιστοποίησης με βάση τον αλγόριθμο interior point, ο οποίος μετατρέπει το αρχικό πρόβλημα της ελαχιστοποίησης της τιμής του figure of merit σε μια σειρά παρεμφερών προβλημάτων ελαχιστοποίησης τα οποία βασίζονται μόνο σε ισότητες και άλλους περιορισμούς. Τέτοιου είδους προβλήματα λύνονται ευκολότερα με τη χρήση μεθόδων όπως της conjugate gradient κλπ, η ανάλυση των οποίων δεν περιλαμβάνεται στους σκοπούς της παρούσας διατριβής. Το figure of merit που επιλέξαμε στην περίπτωση αυτή ήταν ανάλογο της διαφοράς της συνάρτησης μεταφοράς της διάταξής μας από μια Gaussian συνάρτηση έκτου βαθμού, η οποία θεωρείται ιδανική συνάρτηση μεταφοράς για χρήση σε φίλτρα.

Αντίθετα, στην περίπτωση της σχεδίασης της βέλτιστης διάταξης συντονιστών τύπου racetrack για χρήση σε εφαρμογές οπτικών αισθητήρων, όπου οι παράμετροι εισόδου του μοντέλου μας είναι περιορισμένες σε αριθμό, επιλέξαμε να χρησιμοποιήσουμε τη μέθοδο της εξαντλητικής αναζήτησης, ελέγχοντας ταυτόχρονα αν ικανοποιούνται κάποιοι περιορισμοί που θέσαμε αρχικά. Με τη διαδικασία αυτήν, εφόσον ικανοποιούνται οι περιορισμοί, υπολογίζουμε για κάθε συνδυασμό τιμών την τιμή του figure of merit και αποθηκεύουμε τις τιμές αυτές. Κατά την ολοκλήρωση της εξαντλητικής αναζήτησης κρατάμε εκείνον τον συνδυασμό τιμών παραμέτρων, για τις οποίες υπολογίσαμε την ελάχιστη τιμή για το figure of merit, το οποίο στην περίπτωση αυτή είναι ανάλογο με το εύρος συχνοτήτων της περιοχής ανίχνευσης.

Στο σημείο αυτό πρέπει να τονίσουμε ότι και στις δύο παραπάνω περιπτώσεις το εύρος των τιμών των παραμέτρων εισόδου των μοντέλων μας επιλέχθηκε με τέτοιο τρόπο ώστε να είναι δυνατή η υλοποίηση της υπολογιζόμενης διάταξης με βάση τα υλικά και τις κατασκευαστικές μεθόδους που υφίστανται σήμερα. Ακόμα και αν τα παραπάνω αλλάξουν στο μέλλον, με την ανακάλυψη νέων υλικών και μεθόδων, το μοντέλο μας μπορεί να τα υποστηρίξει απλά μεταβάλλοντας το εύρος των τιμών των παραμέτρων εισόδου.

Μετά το πέρας των υπολογισμών μας, καταλήξαμε σε διατάξεις οπτικών φίλτρων και οπτικών αισθητήρων με βελτιωμένα χαρακτηριστικά σε σχέση με τα υπάρχοντα στη βιβλιογραφία, τα οποία μπορούν να υλοποιηθούν χρησιμοποιώντας τα υλικά και τις κατασκευαστικές μεθόδους που διατίθενται στις μέρες μας.

**Λέξεις κλειδιά:** Συντονιστές Μικροδακτυλίου, Συντονιστές Τύπου Racetrack, Φίλτρα, Αισθητήρες

# List of Figures

1.1	Depiction of a) the analysis process and b) the optimization design process . . . . .	20
2.1	Representation of a typical wavelength-routing network [1] . . . . .	24
2.2	Snell's law . . . . .	30
2.3	Total internal reflection at a slab waveguide . . . . .	31
2.4	Waveguide types: a) slab waveguide, b) strip waveguide c) rib waveguide and d) optical fiber . . . . .	31
2.5	Graphical presentation of the EIM . . . . .	34
2.6	Examples of a) standing wave resonators [2] and b) traveling wave resonator . . . . .	35
2.7	Depiction of a) a simple ring resonator, b) its transfer function in a single and c) multiple FSR range. . . . .	37
2.8	Representation of the simplest form of waveguide/cavity system . . . . .	38
2.9	Multiple resonator structures: a) the SCISSOR geometry and b) the CROW geometry . . . . .	39
2.10	Depiction of a) three-terminal hybrid III–V-on-silicon [3] and b) laser-based on integrating second order gratings on the MRs' waveguide [4] . . . . .	40
2.11	Depiction of an a) AND gate [5] b) OR gate [5] c) NOR gate [5] and d) XOR gate [5] . . . . .	41
2.12	Depiction of the a) p-i-n modulator and its normalized transmission spectra [6] and b) top and cross-section views of a carrier-depletion MR modulator [7] . . . . .	42
2.13	Depiction of a) compact MR-assisted directional couplers in the silicon-on-insulator material system [8] and b) reconfigurable silicon thermo-optical device [9] . . . . .	42
2.14	A multi-segment resonator that employs waveguides of different cross-sections for dispersion compensation. The red and blue curves are the light of longer and shorter wavelengths, respectively. The length of the arrows represent the speed of light for each wavelength in different waveguide sections. Mode profiles in narrow and wide waveguides are also sketched. The group velocity dispersion is either negative or positive depending on the material used [10] . . . . .	43
2.15	Representation of a RR structure . . . . .	43
3.1	Depiction of a) coupling region, b) uncoupled straight and c) uncoupled ring waveguides. . . . .	47
3.2	The distribution $\epsilon_r - \epsilon_s$ along with the modal fields $\mathbf{E}_s$ and $\mathbf{E}_r$ . . . . .	50

3.3	Representation of a simple waveguide/ring system . . . . .	54
3.4	Representation of a single ring MR system transmission coefficient . . . . .	55
3.5	Representation of a double ring MR system where the rings are placed in series . . . . .	55
3.6	Representation of a double ring MR system transmission coefficient . . . . .	57
3.7	The two dimensional Yee's grid . . . . .	58
3.8	FDFD calculation of the number of modes for different values of the width and height of the waveguide for $\lambda =$ a) 1550 nm and b) 1330 nm . . . . .	63
3.9	FDFD calculation of the a) horizontal and b) vertical component of the transverse electric field of the waveguide for the highest $n_{\text{eff}}$ mode, for $\lambda = 1500$ nm . . . . .	63
3.10	FDFD calculation of the a) horizontal and b) vertical component of the transverse electric field of the waveguide for the second highest $n_{\text{eff}}$ mode, for $\lambda = 1500$ nm . . . . .	64
3.11	The three dimensional Yee's grid . . . . .	65
3.12	Depiction of the value of electric field $E_z$ during its first pass, inside an MR device using MEEP for different moments varying from 100 fs to 300 fs . . . . .	73
4.1	Schematic of a) a uniform multiring structure and b) a non uniform multiring structure . . . . .	76
4.2	Transfer function of single micro-ring structure . . . . .	80
4.3	Coupling coefficients $\kappa_i$ obtained for a) $N = 2$ , b) $N = 3$ , c) $N = 4$ , d) $N = 5$ and e) $N = 6$ rings . . . . .	82
4.4	Ring radii $R_i$ obtained for a) $N = 2$ , b) $N = 3$ , c) $N = 4$ , d) $N = 5$ and e) $N = 6$ rings . . . . .	83
4.5	Transfer functions near the pass-band obtained for a) $N = 2$ , b) $N = 3$ , c) $N = 4$ , d) $N = 5$ and e) $N = 6$ rings. Dashed lines indicate the weighting function $w(f)$ . . . . .	83
4.6	Transfer functions in a $\pm 2$ THz frequency region obtained for a) $N = 2$ , b) $N = 3$ , c) $N = 4$ , d) $N = 5$ and e) $N = 6$ rings . . . . .	84
4.7	Ratio $\rho$ of the 30 dB bandwidth to the 5 dB bandwidth for the designs in question as a function of the ring number $N$ . . . . .	85
4.8	Average and maximum crosstalk for the designs as a function of the ring number $N$ . . . . .	86
4.9	Intermediate transfer functions obtained during the minimization process for a three ring structure . . . . .	86
4.10	Chromatic dispersion of the single ring ( $N = 1$ ) and six ring ( $N = 6$ ) design . . . . .	87
4.11	Comparison of the transfer function of a 6 ring design for different loss factors . . . . .	88

5.1	The coupled racetrack resonator / waveguide system. In the figure $A_{in}$ , $A_r$ are the amplitudes of the incident and reflected waves at the input, $A'_{in}$ and $A'_r$ are the corresponding waves at the output, while $R'_{CCW}$ and $R'_{CW}$ are the amplitudes of the counter-clockwise and clockwise propagating fields at the input of the coupling region and $R_{CCW}$ and $R_{CW}$ are the corresponding fields at its output. . . . .	90
5.2	First order approximation for a) the real and b) the imaginary part of the diagonal matrix element $m_{11}$ assuming the parameters of table 5.1. . . . .	94
5.3	Comparison of the transfer functions calculated for by (5.2)-(5.4) and the rational approximation (5.32) for the set of parameters quoted in table 5.1. . . . .	96
5.4	Transfer functions of the original designs outlined in table 5.1 and the optimized design of table 5.2, calculated by the rational first-order approximation and the full transfer matrix model. . . . .	99
5.5	Influence of effective refractive index perturbations $\Delta n_S$ in the power transfer function for the optimized design. . . . .	100
5.6	Example of a RR/waveguide system TF $T = T(\Omega)$ which is symmetric around $\Omega = 0$ . The TF exhibits sharp transitions in regions $A_2$ and $A_4$ switching from a regions of low absorption $A_1$ and $A_5$ to a valley of high absorption $A_3$ . . . . .	102
5.7	Optimized TFs obtained through exhaustive search and for various values of $C_{min}$ . The corresponding design parameters are included in Table 5.3. . . . .	110
5.8	Values of $\mathcal{M} = \delta\omega$ obtained for the various values of $C_{min}$ . . . . .	111
5.9	Design obtained for $C_{min} = 7$ dB: a) the TF in terms of the frequency detuning $\Delta f$ from the resonant frequency, b) the lengths of the straight and the radii of the curved section corresponding to the two roots of (5.73) and c) the gain coefficients corresponding to the roots. . . . .	112
5.10	Design obtained for $C_{min} = 15$ dB: a) the TF in terms of the frequency detuning $\Delta f$ from the resonant frequency, b) the lengths of the straight and the radii of the curved section corresponding to the two roots of (5.73) and c) the gain coefficients corresponding to the roots. . . . .	112
5.11	The effect of the effective index perturbations $\Delta n_S$ in the power transfer function for: a) $C_{min} = 7$ dB and b) $C_{min} = 15$ dB. . . . .	113

## List of Tables

2.1	Roadmap for individual supply chain components results with respect to optical power capacity [11] . . . . .	29
2.2	Refractive indices and index contrasts of the most common integrated optic waveguide materials, assuming SiO <sub>2</sub> cladding with refractive index $n_2 = 1.44$ . . . . .	32
3.1	FDFD parameters . . . . .	63
3.2	MEEP parameters . . . . .	73
4.1	Ratio $\rho$ corresponding to the four loss coefficients . . . . .	87
5.1	Initial racetrack parameters . . . . .	95
5.2	Parameters for optimized design . . . . .	100
5.3	Optimal TF parameters . . . . .	110
5.4	Transfer function sensitivity . . . . .	113

## Acronyms

CCW	Counter-clockwise
CW	Clockwise
CMT	Coupled mode theory
CROW	Coupled resonator optical waveguide
EIM	Effective index method
FDFD	Frequency division frequency domain
FDTD	Frequency division time domain
FFT	Fast Fourier transform
FSR	Free spectral range
FWHM	Full width half max
FWM	Four wave mixing
IP	Internet protocol
KPI	Key performance indicator
MOS	Metal-oxide-semiconductor
MR	Microring resonator
OADM	Optical add drop multiplexer
OLT	Optical line terminal
OXC	Optical cross-connect
PIC	Photonic integrated circuit
PML	Perfectly matched layer
PRC	Photonics reservoir computing
ROADM	Reconfigurable optical add drop multiplexer
RIU	Refractive index unit
RR	Racetrack resonator
SCISSOR	Side-coupled integrated spaced sequence of resonators
SoC	System-on-a-chip
SOI	Silicon on insulator
SONET	Synchronous optical network terminal
TF	Transfer function
TIR	Total internal reflection
TMM	Transfer matrix method
WDM	Wavelength division multiplexing

# 1 Foreword

## 1.1 Purpose of the thesis

The main purpose of this dissertation is to contribute in the modeling and designing of key photonic building blocks including filters and sensors in an efficient manner. This is achieved through design tools which take advantage of the underlying coupling physics of waveguides and micro-ring resonators (MR) or waveguides and racetrack resonators (RR). This approach provides a semi-analytic alternative to full-blown electromagnetic simulations that prove intractable both in the time and frequency domain. The time-domain approach, which is very popular due to recent progress in the finite difference time domain (FDTD) methods, results in particularly long computation time, especially in the weakly coupled regime where it takes many iterations for the wave inside the resonator to fully dissipate. Frequency domain methods such as the finite difference frequency domain method (FDFD) on the other hand typically involve the solution of large linear systems which require huge memory resources in order to accurately capture the device curvature. Our semi-analytical methods however, based on coupled mode theory (CMT) and transfer matrix method (TMM) can quickly produce an accurate estimate of the spectral properties of the device.

Once an efficient model for computing the transfer function of the device is identified, one may apply various techniques for optimizing the performance of a single or multiple coupled resonator device. An initial literature survey revealed that researchers have been focusing on developing tools and methods for simulating the operation of a MR structure rather than seeking the optimal parameters that maximize the performance of the device. In other words, much research was done in the *analysis* front, i.e. in calculating the transfer function  $T(f, \mathbf{P})$  of the device from an initial set of parameters  $\mathbf{P}$  rather than the *design* of the structure itself which consists of choosing  $\mathbf{P}$  so that  $T(f, \mathbf{P})$  will have favorable properties, as illustrated in figure 1.1.

Considering for example uniform resonators structures, where all resonators are identical, one could adopt several filter synthesis techniques already found in the literature [12]. This however may result in a set of predetermined values for the parameters  $\mathbf{P}$ , such as the coupling coefficients, that could very well lie outside the range of feasible values under state-of-the-art fabrication techniques, since there are no means of specifying the allowable range of the parameters.

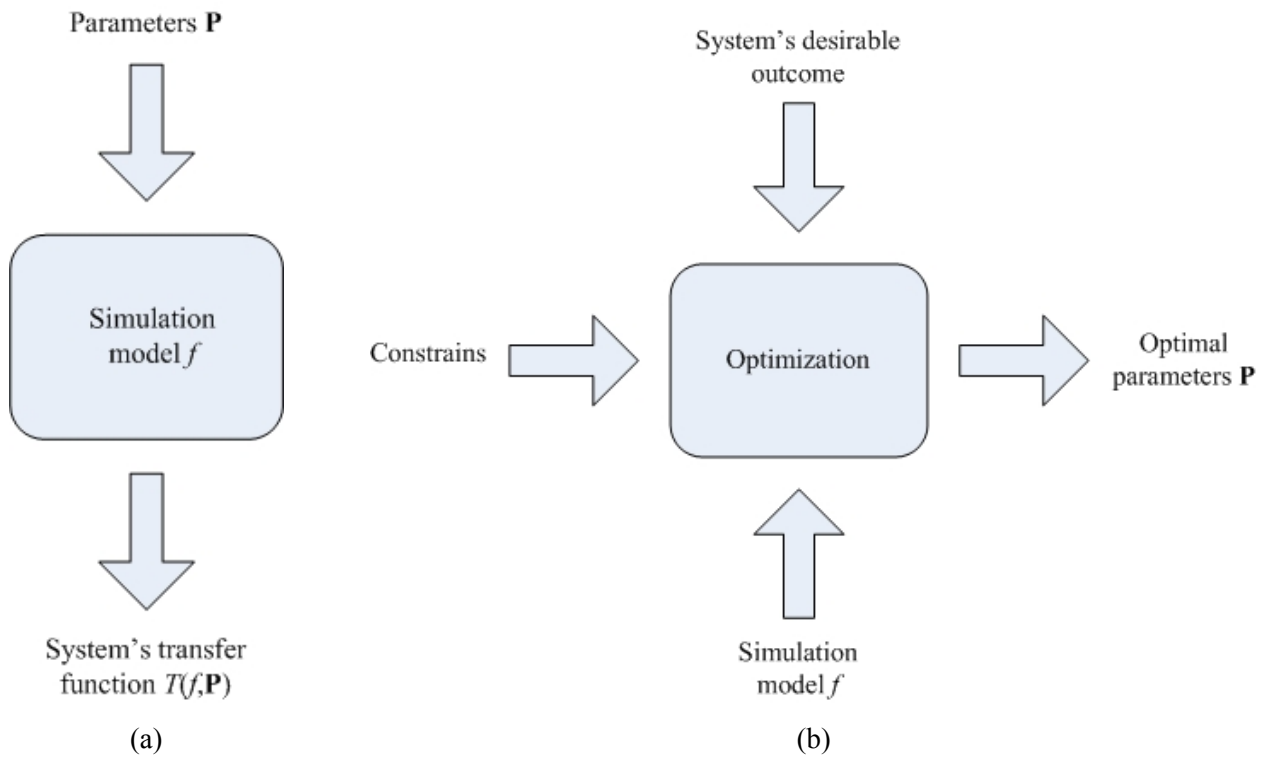


Figure 1.1: Depiction of a) the analysis process and b) the optimization design process

In this thesis, we consider two types of devices each destined for different applications. One is a non-uniform chain of coupled micro-ring resonators where we seek to render  $T(f, \mathbf{P})$  as close to an ideal rectangular box-like transfer function as possible. As we will explain later on, this is of major interest in filtering applications in optical networking. The other type of device is a racetrack resonator where the intra-cavity reflections between the curved and the straight waveguide sections of the resonator may give rise to asymmetric spectral behavior around a resonant frequency involving sharp transitions in one side and smooth transition in the other side of the peak. This is of practical importance in sensing applications. For the first type of device, existing transfer matrix models can be put into use for carrying out our optimizations and obtain the optimal values of  $\mathbf{P}$ . In the racetrack case, we show that under certain reasonable approximations, the transfer matrix model actually leads to a closed form analytical solution for  $T(f, \mathbf{P})$ , thereby rendering the search for the optimal values of  $\mathbf{P}$  much easier.

The components designed can be implemented using a number of state-of-the-art fabrication technologies and widely used materials. This is ensured by initially defining the range of certain parameters so as to reflect the materials and fabrication processes used today. Using the framework developed in this thesis, the range of these parameters can be adjusted in order to include new material and structural parameters reflecting different fabrication processes that may be developed in the future.

## 1.2 Outline of the thesis

The rest of the dissertation is organized as follows:

In chapter 2 we lay the foundations for this thesis, summarizing the pertinent current state-of-the-art in optical communications and sensing. We also present the underlying physics of a basic coupled waveguide/cavity system and then proceed to the case of single cavity and multiple cavity structures. We also briefly review the properties of ring and racetrack resonators.

In chapter 3, we present the various approaches for modelling coupled cavity systems including the coupled mode theory, the finite difference frequency domain and the finite difference time domain methods. CMT differs fundamentally from FDFD and FDTD since it relies on mode expansion while the latter two attempt to brute-force solve Maxwell's equations in the frequency and time domain respectively. Each method comes with its own merits and pitfalls which we attempt to highlight in this chapter. We also briefly consider optimization techniques that can be used for electromagnetic design.

In chapter 4 we present a framework for designing single- and non-uniform multi-cavity coupled micro-ring structures by combining the transfer matrix method and optimization methods. We calculate the optimal parameters  $\mathbf{P}$  so that the transfer function of the device  $T(f)$  resembles a box-like response. Given the number of rings, the design framework can be applied to calculate the required parameters such as ring radii and coupling coefficients which can be kept within specific ranges determined by the fabrication process. We also consider the effect of optical loss and the chromatic dispersion.

In chapter 5 we present a detailed modeling and design framework for racetrack resonators taking into account intra-cavity reflections. We discuss the conditions in which Fano resonances appear and provide analytic expressions for the transfer function  $T(f)$  and validate their accuracy against the more detailed TMM model. This analytic model yields significant insight in the spectral properties of the device which is otherwise lost in the TMM. We then proceed to use the analytic model to design the racetrack structure for sensing applications.

Finally, in the last chapter some conclusions extracted from our experience on the design process are discussed, along with an outlook of the future research that can be done on the subject in the fields of photonic crystal cavities, slow light graphene and neural networks.

## 2 Introduction

In this chapter, we provide a brief introduction to the optical technologies associated with micro-ring and racetrack resonators which constitute a fundamental building block in photonic integrated circuits (PICs) intended for telecommunications and sensing. We also present the material platforms that can be used for the realization of the basic building blocks of a coupled resonator system, the underlying physics and potential applications.

### 2.1 Optical communications systems

The needs for communication and information exchange are rapidly increasing fueled by new applications and concepts such as cloud computing and the internet-of-things. According to CISCO's projections [13], the annual global internet protocol (IP) traffic will reach an impressive 4.8 ZB per year by 2022, or 396 EB per month. In 2017, the annual run rate for global IP traffic was 1.5 ZB per year, or 122 EB per month. This traffic explosion is sustained by the continuous improvement of several data transmission technologies.

Technology has come a long way since the invention of the telegraph in 1830 which marks the beginning of the electronic communications era. A few years later, in 1866, the first transatlantic telegraph cable was successfully installed and started operating. With the use of Morse code, the transmission speed was significantly increased. Ten years later, in 1876, Alexander Graham Bell invented the telephone which allowed the electric signals to be transmitted in an analog manner by constantly alternating electric current in a pair of copper wires. This technology was dominant for more than a century. In the late 1930s, copper wire pairs started being replaced by coaxial cables in an attempt to increase the system's capacity. Although coaxial cables provided much larger bandwidth, the losses, turned out to be proportional to the frequency of operation, introducing many limitations. The late 1940s marked the birth of microwave communication systems and by the mid 1960s optical communication networks started being deployed by gradually replacing classic copper wires with optical fiber cables, allowing high bit rates to be achieved over longer distances through visible or infrared radiation. Optical fiber technology has revolutionized the way in which we can communicate offering several advantages to conventional microwave and coaxial technologies. The merits of optical communication systems are summarized as follows [14], [15], [16]:

- Optical fibers suffer from very low loss ( $\cong 0.2$  dB/km attenuation) implying that very long-reach optical links can be implemented.
- Fibers can offer huge amounts of transmission bandwidth of the order of several tens of THz resulting in aggregate data rates of the order of 10Tb/s over just a single fiber.
- Their weight and size are very small which makes them relatively easy to install in large densities.

- They are immune to electromagnetic interference since fibers are not electrical conductors. This means that they can be installed next to high power sources without any problems or they can even be installed across the already existing electrical grid.
- They are not flammable and can be used in dangerous environments, such as chemical plants, where a spark could easily trigger an explosion if flammable materials are present.
- They are very secure as it is quite difficult for someone to tap into a fiber cable in order to read the data signals without being discovered.
- They alleviate the increasing concern about adverse biological effects of wireless communication radiation on human health.

As in the case of any communication network, optical networks can be envisioned as a collection of several point-to-point links connecting the various network nodes. Each link consists of three main parts, the transmitter, the communication channel and the receiver. Each part consists, in turn, of several opto-electronic components such as light emitters, light detectors, amplifiers, filters, waveguides etc. Although optical fibers suffer from relatively low loss, power loss increases exponentially and hence the use of optical amplification is required, in long-reach systems.

The optical transmitter converts the electrical signal to light and couples it to the optical fiber channel. The resulting optical signal may consist of several separately modulated wavelengths multiplexed together. This is referred to as wavelength division multiplexing (WDM). A key component of the transmitter is the optical source, which is, in most of the cases, a LASER diode. After the signal is transmitted through the communication channel it is coupled to the receiver, where wavelength demultiplexing is performed. Then the signal is converted back to its electrical form with the aid of light detectors. Optical filters are the basic building blocks of a wavelength multiplexer and demultiplexer.

Optical communications traditionally revolved around the telecom arena but recent years have seen a shift towards datacom applications as well. Data center communications now constitute a major driver for photonic technologies since the need for single channel data rates have now exceeded 10 Gb/s both at an inter- and intra-rack level. Copper transmission lines simply can not keep up with these data rates and introduce excessive loss, a fact that highlights the necessity for a transition to photonic interconnects. Data center traffic doubles every year, whereas the silicon-based packet switch chip capacity doubles every two years. As data rates increase and single-chip bandwidth saturates, the scaling out of data center networks becomes increasingly difficult. This inevitably leads to the replacement of silicon switching elements with optical switches which can manage the optical signal directly [17], [11].

## **2.2 Optical add-drop multiplexers**

WDM introduces an additional degree of freedom in the design of optical networks since switching can be done on a wavelength level, with the use of appropriate components. The architecture of such

a typical wavelength-routing network is shown in figure 2.1. A *lightpath* is an optical connection carried from end to end starting from a source node to a destination node over the same wavelength on each intermediate link [1]. These lightpaths can be generated by synchronous optical network terminals (SONET) or IP routers and are routed from one link to another at intermediate nodes in the network. In a wavelength-routing network, the same wavelength can be used in different lightpaths, as long as they do not share any common links. This feature, allows the same wavelength to be spatially reused in different parts of the network. The basic network elements that enable optical networking are the optical line terminals (OLTs), the optical cross-connects (OXC) and the optical add/drop multiplexers (OADMs) as depicted in figure 2.1. The role of an OLT is to multiplex multiple wavelengths into a single fiber and demultiplex a set of wavelengths on a single fiber into separate fibers and is used at the ends of a point-to-point WDM link. OXCs perform a similar function but at much larger sizes. The number of ports they possess ranges from a few tens to thousands and they are capable of switching wavelengths from one input port to another. An OADM receives multiple wavelength signals and selectively drops some of these wavelengths locally while allowing all others to pass through. Also, it selectively adds wavelengths to the complex outbound signal. OADMs use two line ports for the composite WDM signals and a number of local ports for the individual wavelengths that are dropped and added.

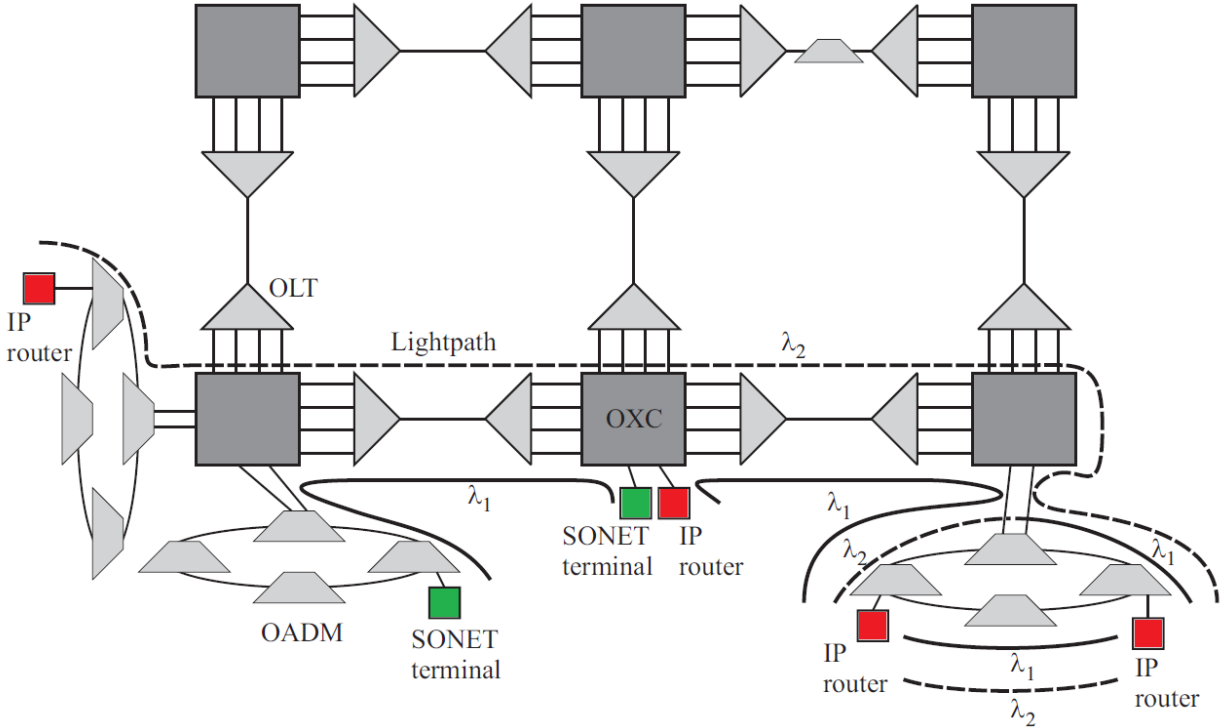


Figure 2.1: Representation of a typical wavelength-routing network [1]

Several key performance indicators (KPIs) are related to OADMs:

- They should present low insertion losses, independent of wavelength and polarization.
- The spectral characteristics (e.g. the positions of the central multiplexed and demultiplexed wavelength) should not depend upon signal polarization and temperature.

- Small wavelength drifts within a specified tolerance range, should not affect the device performance.
- OADMs should reject wavelengths outside this tolerance range in order to avoid crosstalk between adjacent channels.
- Ideally an OADM should be entirely passive (i.e. the power consumption should be negligible).
- OADMs should be fully transparent to all data rates and protocols.
- They should be fabricated using materials which are appropriate for integration.
- Their fabrication process should be cost-effective.

Reconfigurable add-drop multiplexers (ROADMs) enable dynamic (software-driven) provisioning of wavelengths in a WDM network without major network changes or redesign. ROADMs consist of a wavelength selective switch which is a device that can dynamically route a wavelength from one input port to another and several auxiliary elements such as variable optical attenuators in order to provide uniform power distribution of the output wavelengths and the corresponding power monitors. ROADMs provide great flexibility in rerouting optical streams and bypassing damaged connections which allows minimal service disruption and also provides the ability to adapt or upgrade the optical network to different WDM technologies [18]. There are several technologies used in order to fabricate an OADM. The majority of them use a variety of demultiplexer and multiplexer technologies including thin film filters, free space grating devices, fiber Bragg gratings with optical circulators and integrated planar arrayed waveguide gratings. The switching and reconfiguration functions range from the manual fiber patch panel and micromirrors to a variety of switching technologies including microelectromechanical systems, liquid crystal and thermo-optic switches in planar waveguide circuits [19], [20], [21].

## 2.3 Optical sensors

The role of an optical sensor is to detect changes in a specific characteristic of the subject under investigation. During the last decades, optical sensors have been finding their way into an increasing number of applications. The development of the semiconductor industry in the 1940s and '50s led to lower-cost, compact and efficient light-sensing devices. The interest in optical sensors is justified due to the high sensitivity, low-cost, compactness, possibility of integration with other electronic devices and electromagnetic immunity. Integrated photonic sensors include ring resonators [22] and surface plasmons [23].

Resonant photonic structures lend themselves for the realization of optical sensors by means of measuring (a) resonant-wavelength shift and/or (b) intensity variation induced by the substance or physical magnitude under study. Nowadays, sensors are packaged along with tiny integrated circuits resulting in a complete system-on-a-chip (SoC) which is far simpler to use. According

to recent market research reports, the market of light sensors is expected to reach USD 2.14 Billion by 2022, a trend driven by the increasing usage of such devices in smartphones and tablets. Additionally, the image sensor market is expected to reach USD 17.5 Billion by 2020 [24], [25], [11].

Optical bio-sensors based on ring resonators are very intriguing technological platforms [26] since planar waveguide ring resonators are easily integrated, have a small footprint, and can be fabricated by standard techniques, thus enabling mass production at low cost [27]. The operating principle depends on the variation of the effective refractive index of the optical mode propagating into the structure, which is due to the presence of a chemical substance, detected near the sensor's surface. We shall further analyze the notions of the ring resonator and the effective refractive index in later sections. In general, bio-sensors are devices used in order to characterize a chemical quantity, the analyte, determine its concentration and study the kinetics of its chemical reactions. The fundamental idea behind bio-sensing is the usage of the work done by biological evolution in order to create highly selective bio-molecular pairings. Subsequently using one part of the pair as a recognition element the selective measurement of the other part is detected. The biological recognition system provides selectivity and translates information from the biochemical domain into chemical or physical output [28]. According to the international union of pure and applied chemistry, a bio-sensor is a self-contained integrated device that is capable of providing selective quantitative analytical information using a biological recognition element which is in direct spatial contact with a transducer element [29].

Another area where MR-based sensors can be employed, is for the realization of integrated optical gyroscopes which estimate the angular velocity in inertial systems. In this situation, the Sagnac effect is the operating principle which characterizes the photonic sensing mechanism [24]. In more detail, a phase shift between two counter-propagating beams, proportional to the angular velocity at which the device is rotating, is detected. Due to the nature of optical waveguides, optical sensors are suitable devices for various applications which include oil and gas applications, pipeline monitoring, wind turbine blade monitoring, off-shore platform monitoring, power line monitoring, down-hole monitoring and concentration measurement of different compounds by both visible and infrared spectroscopy [25], [11].

The sensitivity of integrated photonic sensors using ring resonator technologies, can be significantly enhanced if the spectral response of the resonator demonstrates asymmetric resonances which would differ from the standard symmetric Lorentzian line-shape of a single cavity. To this purpose, asymmetric Fano lineshapes would be ideal. This can be achieved by either using more than one ring cavity or by using a racetrack shaped cavity structure, as will be explained in detail in chapter 5. Optical sensors that exploit Fano resonances have been already demonstrated in applications such as bio-sensing [30] (see also [31], [32] and [33]) while the available design tools for Fano resonant structures are enriched with the contribution of this dissertation [24], [34].

## 2.4 Integrated optics and material platforms

The major challenges for the photonic component industry include integration (in order for the functionality and cost benefits to be increased), standardization (common framework for manufacture and development), cross-market platforms (to drive research and development) and supply-chain coordination (to coordinate the manufacturing process) [11]. As a consequence, the future needs of the systems and the identification of any gaps or roadblocks which might affect the manufacturing of integrated photonic systems have to be defined, concentrating especially on the aforementioned challenges, which should be addressed in order to achieve commercial success and viability. WDM interconnects are likely to be deployed on a massive scale by 2025, a fact that will define the beginning of commercial chip-to-chip and intra-package photonic interconnects era [11]. Working in this frame, researchers are experimenting with different material platforms in an effort to address the challenges and needs stated above. Those material platforms include [35]:

- **Si-based platforms:** Silicon-based platforms include silicon nitride-on-silica, silica-on-silicon and silicon-on-insulator (SOI) [36]. Silica waveguides are easily interfaced with free-space optics and fibers, resulting in the first demonstrations of integrated circuits [37]. Although the silica-on-silicon platform is being used today, especially for quantum communication experiments [38], [39], for larger-scale information processing purposes, it has been dominated by the SOI technology [40]. Silicon's refractive index is much higher than silica's, which is a fact that allows  $10^3$  times smaller waveguide bend radius compared to that in silica waveguides. Silicon's indirect 1.12 eV band-gap along with its low intrinsic carrier concentration, makes it transparent to photons at the telecommunication wavelength of  $1.55 \mu\text{m}$ . The major advantages of the SOI platform are its compatibility with the CMOS industry [41] along with the well established fabrication techniques already developed for silicon electronics and photonics [42], which has lead to the development of a full range of required components. The combination of silicon nitride and silicon waveguides is a technique that can guarantee temperature-insensitive operation in data transmission systems. The use of titania as a cladding material in a Si waveguide, can control the thermo-optic response. Additional waveguide systems can broaden the applications range of the silicon photonic circuits as silicon nitride waveguides for instance, which are transparent to visible light, can be utilized in order to fabricate compact biosensing systems on small Si chips [43], [44]. Researchers also have to deal with the need for scaling the number of on-chip components and achieving advanced functionalities [45].
- **III-V platforms:** III-V based platforms, such as GaAs and InP, offer radically new capabilities in comparison to the silicon based platforms. Semiconductor laser technology used today, allows on-chip integration of highly tunable pump sources with electrical injection [46]. At present, GaAs is one of the most developed III-V photonic platforms [47] with a high refractive index which allows high density integration, strong light confinement in GaAs/AlGaAs waveguides and fast electro-optic switching. Due to their lack of inversion symmetry, many III-V materials exhibit the electro-optic effect, which allows fast on-chip

switching [48]. Recently, the generation, channeling and detection of single photons on the same chip became possible, with the aid of on-chip integration of superconducting detectors [49], [50].

- **Polymers:** Optical polymer materials possess unique optical and electrical properties, unavailable in other inorganic optical materials. These include structural diversity, large thermo-optic effect with low thermal conductivity, index tunability by solution blending, controllable birefringence and freestanding flexibility [51]. This is the reason behind the boost of such platforms in practical applications. Devices that use polymers include broadband solar cells, ultra-fast electro-optic modulators, efficient white light emitting diodes and flexible displays [52]. Due to the improvements in the fabrication technology, their implementation is now fast, cost-effective and provides flexibility and broad compatibility with other semiconductor processing technologies [53], [54]. Integration of polymers in photonic platforms such as silicon-on-insulator, III-V semiconductors, and silica, and vice versa, has been reported [51].
- **Bulk diamond and diamond-on-insulator:** Diamonds present exceptional mechanical, thermal and optical properties but are quite difficult to synthesize and process. Due to the recent development of various fabrication techniques [55], diamond has proven to be a competitive platform for realizing highly functional photonic integrated circuits [56]. Some of the unique advantages of diamond include wide band-gap, high isotopic purity, high Debye temperature and low free electron concentration [57].
- **Lithium niobate:** This optical material has been used since the beginning of the integrated optics era and is considered highly versatile [58]. Its properties include ferro-electricity, birefringence, electro-optic effect, chemical stability and high transparency. Large-scale wafers are produced commercially and well developed fabrication techniques exist [59].
- **Silicon carbide:** This group IV material is a high band-gap material, which, like diamond, presents a wide variety of color centers. In contrast to diamond, fabrication techniques for SiC structures are better developed [60], [61].

Nowadays, the most popular photonic materials are Si, III-V and LiNbO<sub>3</sub> because of the particularly high degree of integration originating from their long history of development. Among the elementary platforms, only the III-V materials present the full range of required on-chip devices, ranging from pump lasers to photon detectors. This is the reason why such platforms are expected to achieve full integration within the next few years [35], [11].

Table 2.1 depicts the detailed results of the roadmap for individual supply chain components, with respect to optical power capacity.

Key Attribute	Description	2016	2018	2020	2025	2035
Transparency (dB/cm)	attenuation/distance	0.35	0.1	0.05	0.001	0.001
Material (n)	effective index	1.8-4	1.8-4	1.8-4	1.8-4	1.8-4
Index contrast ( $\Delta n$ )	n(core)-n(clad)	$10^{-3} - 3$	$10^{-3} - 3$	$10^{-3} - 3$	$10^{-3} - 3$	$10^{-3} - 3$
Stability (pm/°K)	spectral shift of resonator	25	1	1	0.5	0.01
Power (mW)	optical power capacity	30	30	50	100	500
Wafer uniformity (nm)	layer thickness variation	10	1	1	0.5	0.5
Material system (Core/clad)	waveguide and cladding materials	Si, SiN/SiO <sub>2</sub>	Si, SiN, Ge, ChG/polymer, SiO <sub>2</sub> , ChG	multilayer	multilayer	multilayer

Table 2.1: Roadmap for individual supply chain components results with respect to optical power capacity [11]

As a conclusion one can suggest that the current technology is on the verge of achieving an ultimate technology which will be able to integrate all photonic and electronic functions on a single chip.

## 2.5 Optical waveguides

### 2.5.1 Waveguide structure and materials

The devices designed in this thesis comprise of two fundamental types building blocks: optical waveguides and optical resonators. A dielectric optical waveguide is the basic structure used for the confinement and guiding of light in well-defined discrete propagating *waveguide modes* in photonic integrated circuits. By definition, a waveguide mode is a transverse field pattern whose amplitude and polarization profiles remain constant along the propagation coordinate  $z$  of the waveguide. In dielectric waveguides, total internal reflection (TIR) is a means of achieving this confinement. The simplest dielectric guiding structure can be achieved by embedding a layer of high index  $n_1$  material (core), inside a low index  $n_2$  material (cladding) as shown in figure 2.4a. This structure is referred to as *dielectric slab*. Due to TIR at the interfaces between the high-index core and the lower-index cladding media, light is confined within the core. The degree of confinement is relevant to the refractive index contrast between the core and cladding:

$$\Delta n = \frac{n_1 - n_2}{n_1} \quad (2.1)$$

An optical ray is reflected back and forth between the two interfaces of the core layer, if the angle of incidence between the propagating direction of the light and the perpendicular direction to the material interface, is greater than a critical angle  $\theta_c$ . This angle depends on the index of refraction of the materials. Considering a ray of light moving from a material with refractive index  $n_1$  towards another material with lower refractive index  $n_2$ , with an angle of incidence of  $\theta_1$ , as depicted in

figure 2.2, then Snell's law dictates that:

$$\frac{n_1}{n_2} = \frac{\sin\theta_2}{\sin\theta_1} \quad (2.2)$$

From (2.2), we easily obtain that the angle of the refracted wave is:

$$\theta_2 = \sin^{-1} \left( \frac{n_1 \sin \theta_1}{n_2} \right) \quad (2.3)$$

If  $\frac{n_1}{n_2} > 1$  then we readily see that if  $\sin \theta_1$  is larger than  $\frac{n_2}{n_1}$  then  $\sin \theta_2 > 1$  suggesting that no refractive wave exists and hence TIR takes place. We define  $\sin \theta_c = \frac{n_2}{n_1}$  or equivalently,

$$\theta_c = \sin^{-1} \frac{n_2}{n_1} \quad (2.4)$$

We can therefore verify that if the angle of incidence  $\theta_1$  is larger than  $\theta_c$ ,  $\theta_1 > \theta_c$ , then TIR takes place and no radiation is expected to leak outside the core layer. This geometrical optics description is valid if the core width  $w$  is much larger than the wavelength of light  $\lambda$ ,  $w \gg \lambda$ . The propagating modes correspond to the various possible ray routes from the input to the output. As the core width  $w$  becomes comparable with  $\lambda$ , one needs to resort to Maxwell's equation in order to fully describe the propagation of light, but geometric optics can still provide valuable insight. It turns out that the different light paths are discrete and a structure with very small  $w$  can support only the direct wave connecting the input and output terminals which corresponds to the *fundamental* waveguide mode. A structure supporting only a single mode of propagation is referred to as a *single mode* waveguide. When more paths exist, we obtain a *multimode* waveguide (see figure 2.3). Although the dielectric slab can be used to illustrate the underlying physics of wave propagation in dielectric optical waveguides, it confines the waves only in one direction and therefore has no major practical application [62].

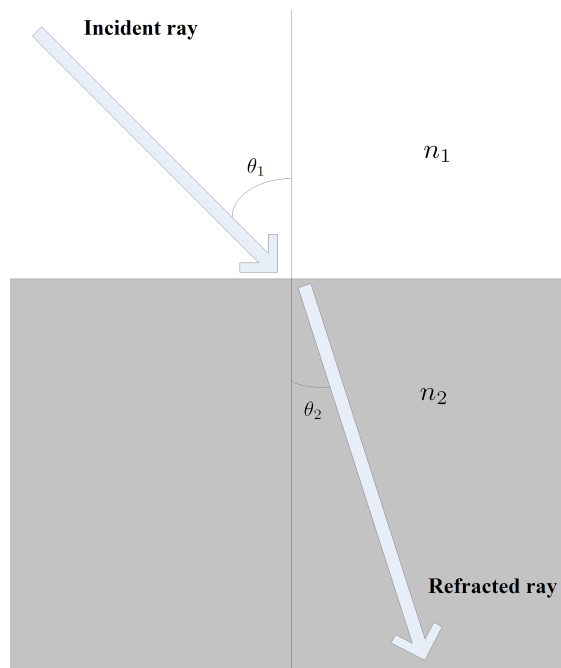


Figure 2.2: Snell's law

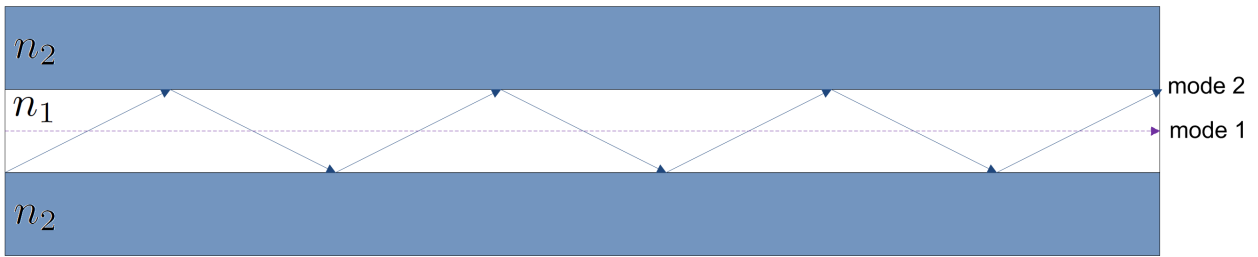


Figure 2.3: Total internal reflection at a slab waveguide

In practical applications, we wish to confine light in both directions perpendicular to the propagation path. A *strip* waveguide is formed when a core layer is confined between cladding layers in two out of three dimensions. The most straightforward example is a rectangular waveguide, which is formed by a rectangular guiding core layer surrounded by a lower index material in both transverse directions, as shown in figure 2.4b. Rectangular waveguides are commonly used in integrated optical circuits such as laser diodes [62]. Additionally, they are utilized as a basic component of Mach–Zehnder interferometers and wavelength division multiplexers.

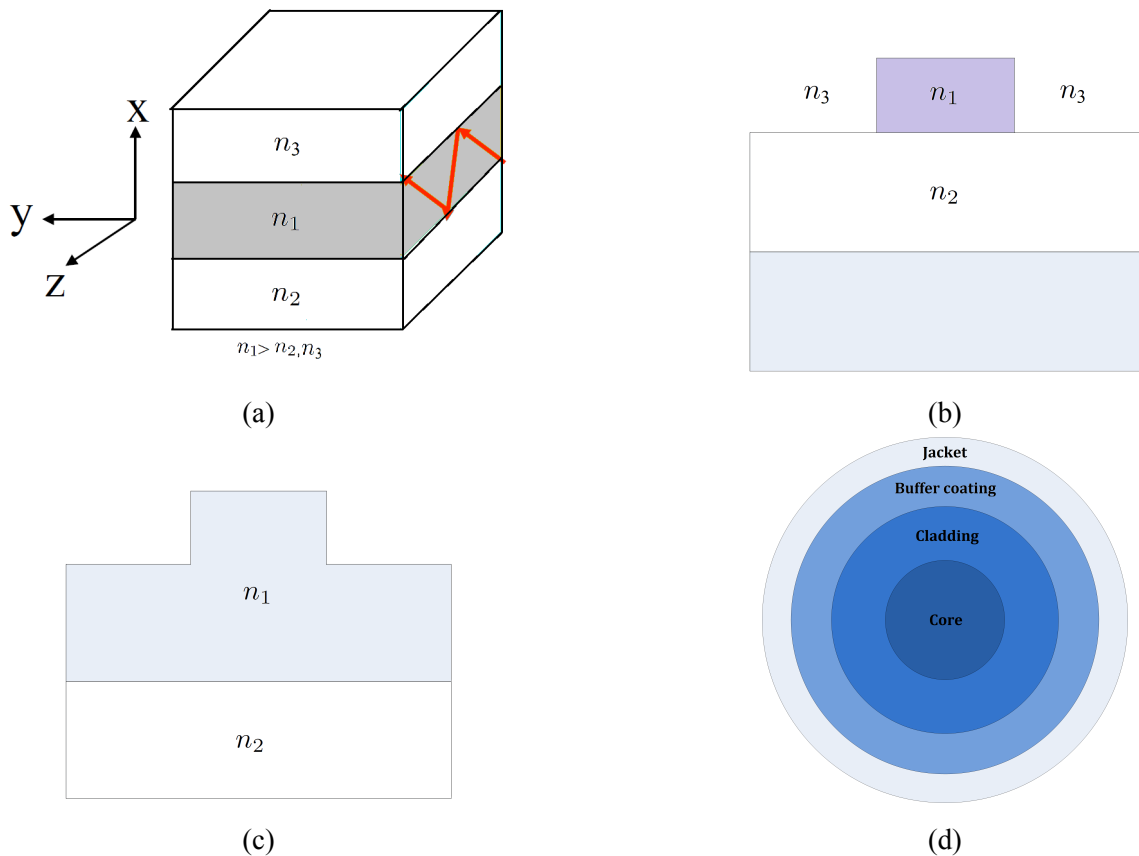


Figure 2.4: Waveguide types: a) slab waveguide, b) strip waveguide c) rib waveguide and d) optical fiber

A third kind of waveguide is a rib waveguide where the guiding layer consists of the slab with one or several strips superimposed onto it, and this kind also provides a two dimensional wave confinement, like the one depicted in figure 2.4c [62]. Although strip and rib waveguides typically

maintain a consistent cross-section along the propagation direction, other waveguide structures with periodic changes in their cross-section have been developed. These waveguides are known as segmented waveguides or as photonic crystal waveguides and they still allow lossless transmission of light, via the so-called periodic Bloch modes [62]. The previous designs are suitable for PICs but perhaps the most popular optical waveguide is the optical fiber which consist of a dielectric material surrounded by another dielectric material with a lower refractive index, as depicted in figure 2.4d, commonly made from silica glass (for long distance applications) or plastic (for short-distance applications). [62]. The most common waveguide material systems and their index contrasts are presented in table 2.2, where one can see that the typical index contrast  $\Delta n$ , ranges from about 1% (for weakly confined waveguides based on doped silica materials), to over 40% (for strongly confined semiconductor waveguides) [63].

<b>Core Material</b>	<b>Refractive Index at <math>\lambda = 1.55\mu\text{m}</math></b>	<b>Index Contrast <math>\Delta n(\%)</math></b>
Doped silica	1.45-1.5	0.7-4
Polymers	1.45-1.7	0.7-14
$\text{SiO}_x\text{N}_y$	1.45-2.0	0.7-24
$\text{SiN}_x$	2.0-2.3	24-30
III-V (InP, GaAs)	3.16, 3.4	40, 41
Si	3.47	41

Table 2.2: Refractive indices and index contrasts of the most common integrated optic waveguide materials, assuming  $\text{SiO}_2$  cladding with refractive index  $n_2 = 1.44$

## 2.5.2 Electromagnetic analysis

The finer details of mode propagation in optical structures can be studied using Maxwell's equations which describe the temporal evolution of the electric and magnetic components. In the time domain, the differential form of Maxwell equations becomes [64]:

$$\frac{\partial \mathbf{B}}{\partial t} = -\nabla \times \mathbf{E} - \mathbf{M} \text{ (Faraday's Law)} \quad (2.5a)$$

$$\frac{\partial \mathbf{D}}{\partial t} = \nabla \times \mathbf{H} - \mathbf{J} \text{ (Ampere's Law)} \quad (2.5b)$$

$$\nabla \cdot \mathbf{D} = 0 \text{ (Gauss's Law for the electric field)} \quad (2.5c)$$

$$\nabla \cdot \mathbf{B} = 0 \text{ (Gauss's Law for the magnetic field)} \quad (2.5d)$$

where  $\mathbf{E}$  is the electric field in V/m,  $\mathbf{D}$  is the density of the electric flow in Cb/m<sup>2</sup>,  $\mathbf{H}$  is the magnetic field in A/m,  $\mathbf{B}$  is the density of the magnetic flow in Weber/m<sup>2</sup>,  $\mathbf{J}$  is the density of the electric current in A/m<sup>2</sup> and  $\mathbf{M}$  is the density of the equivalent magnetic current in V/m<sup>2</sup>.

The field flows  $\mathbf{D}$  and  $\mathbf{B}$  are related to the fields  $\mathbf{E}$  and  $\mathbf{H}$  through the medium's constitutive relationships. Depending on the material and structure properties, these relation can be fairly complex. A first approximation is to assume that these relationships are scalar. For most dielectric

materials one can use the following equations:

$$\mathbf{D} = \epsilon \mathbf{E} \quad (2.6a)$$

$$\mathbf{B} = \mu \mathbf{H} \quad (2.6b)$$

with  $\epsilon$  being the permittivity and  $\mu$  the permeability of the medium. For most materials under consideration one can simply assume that  $\mu$  is equal to the vacuum permeability  $\mu_0 = 4\pi \times 10^{-7}$  H/m while the permittivity is related to the refractive index  $n$  through  $\epsilon = n^2 \epsilon_0$  where  $\epsilon_0 = 8.854 \times 10^{-12}$  F/m is the vacuum permittivity. In the absence of electric and magnetic currents, it is useful to cast Maxwell's equations in the frequency domain [64],

$$\nabla \times \tilde{\mathbf{E}} = j\omega\mu\tilde{\mathbf{H}} \quad (2.7a)$$

$$\nabla \times \tilde{\mathbf{H}} = -j\omega\epsilon\tilde{\mathbf{E}} \quad (2.7b)$$

$$\nabla \cdot \{\epsilon\tilde{\mathbf{E}}\} = 0 \quad (2.7c)$$

$$\nabla \cdot \tilde{\mathbf{H}} = 0 \quad (2.7d)$$

where the tilde ( $\sim$ ) denotes the fields in the frequency domain calculated through the Fourier transform. Assuming a structure that is uniform along the  $z$ -axis,  $\epsilon = \epsilon(x, y)$ . In this case, the waveguide modes are solutions to Maxwell's equation in the frequency domain of the form [64]:

$$\tilde{\mathbf{E}} = \mathbf{e}(x, y)e^{j\beta z} \quad (2.8a)$$

$$\tilde{\mathbf{H}} = \mathbf{h}(x, y)e^{j\beta z} \quad (2.8b)$$

where  $\mathbf{e}$  and  $\mathbf{h}$  are the modal fields along the transverse coordinates  $(x, y)$  and  $\beta$  is the propagation constant determining the phase evolution of the wave along the propagation direction  $z$ . The effective index is determined as  $n_{\text{eff}} = \beta/k_0$  where  $k_0$  is the wavenumber in free space  $k_0 = 2\pi/\lambda$  and is an important parameter of the waveguide mode. For propagating modes in dielectric waveguides, the effective index is between the refractive index of the background material and the core. For example, in figure 2.4b one has  $n_2, n_3 < n_{\text{eff}} < n_1$ .

The above equations can be re-written in scalar form:

$$\frac{\partial e_z}{\partial y} - j\beta e_y = j\omega\mu_0 h_x \quad (2.9a)$$

$$\frac{\partial e_z}{\partial x} - j\beta e_x = -j\omega\mu_0 h_y \quad (2.9b)$$

$$\frac{\partial e_y}{\partial x} - \frac{\partial e_x}{\partial y} = j\omega\mu_0 h_z \quad (2.9c)$$

$$\frac{\partial e_z}{\partial y} - j\beta h_y = -j\omega\epsilon e_x \quad (2.9d)$$

$$\frac{\partial h_z}{\partial x} - j\beta h_x = j\omega\epsilon e_y \quad (2.9e)$$

$$\frac{\partial h_y}{\partial x} - \frac{\partial h_x}{\partial y} = -j\omega\epsilon e_z \quad (2.9f)$$

$$\frac{\partial e_x}{\partial x} + \frac{\partial e_y}{\partial y} + j\beta e_z = 0 \quad (2.9g)$$

$$\frac{\partial h_x}{\partial x} + \frac{\partial h_y}{\partial y} + j\beta h_z = 0 \quad (2.9h)$$

Maxwell's equations can be solved in a variety of numerical and analytical methods depending on the structure at hand. The finite difference time domain method that will be presented in section 3.8 is quite popular for solving the time domain equations in (2.5). In order to solve Maxwell's equation in the frequency domain the finite difference frequency domain method can be applied which is also applicable for the modal equations in (2.9). We will further outline the FDFD method in section 3.7. Both the FDTD and FDFD rely on the discretization of the structure using a specified point grid and the approximation of the partial derivatives with finite differences and are numerical methods. The various analytical and semi-analytical methods on the other hand take advantage of the underlying material and structural characteristics in order to simplify Maxwell's equations. An example of such a method is the coupled mode theory framework further discussed in section 3.3.

Another widely used semi-analytical method that can be used to solve the modal equations is the effective index method (EIM) [65]. The main idea behind the EIM in the case of rectangular-like waveguide such as the one depicted in figure 2.4b, is that the components of the mode  $\mathbf{e}$  inside the waveguide, can be considered as the product of two functions of one variable, i.e.  $e_x = f_x(x)g_x(y)$ . This effectively breaks down the problem into two slab-like problems one in the  $y$  direction (vertical direction) and one in the  $x$  direction (horizontal direction) as shown in figure 2.5. The solutions for the slab waveguide are relatively straightforward and are found by solving well known transcendental equations [66]. One can therefore proceed to solve the vertical problem and calculate the corresponding effective index  $n_{\text{eff}}^y$  and then consider the horizontal slab problem by replacing  $n_1$  with  $n_{\text{eff}}^y$  as shown in 2.5. Although this approximation can lead to significant errors especially in the case of high index contrast  $\Delta n$ , it provides a powerful tool for waveguide analysis due to its simplicity [67].

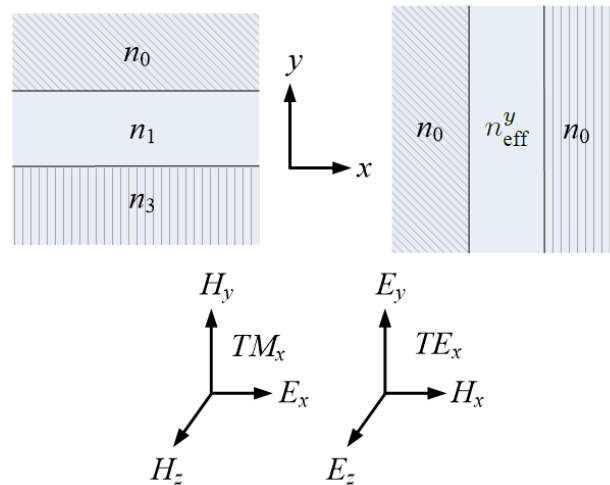


Figure 2.5: Graphical presentation of the EIM

## 2.6 Optical resonators

In general, a resonant optical cavity (or optical resonator) describes a set of optical components, arranged in such a manner that allows a beam of light to circulate in a closed path, i.e. it confines

light in all spatial directions. Such arrangements are implemented in various ways (disk resonators, ring resonators, RRs etc). There are two basic types of cavities. The first type is the standing-wave cavity where light travels back and forth between end-mirrors and the field at any point is the result of the standing-wave interference pattern between waves traveling in opposite directions (figure 2.6a). As a result, the field in a standing-wave resonator has a spatially-dependent amplitude distribution. The second type is the traveling wave resonator where the light propagates in round-trips in different directions without using any end mirrors (figure 2.6b) [68], [69]. The field amplitude in a traveling-wave resonator is nearly uniform. In both cases, resonators may contain additional optical elements which are passed in each round trip as in the case of a laser resonator which contains a gain medium that can compensate the path losses in each round trip. An important advantage of traveling wave over standing wave resonators is that no mirrors are required which can be difficult to fabricate in integrated optics. Moreover, the unidirectional propagating light in the travelling wave resonators, favours the distinction between the output light signals from the input light (physically isolated ports) [63].

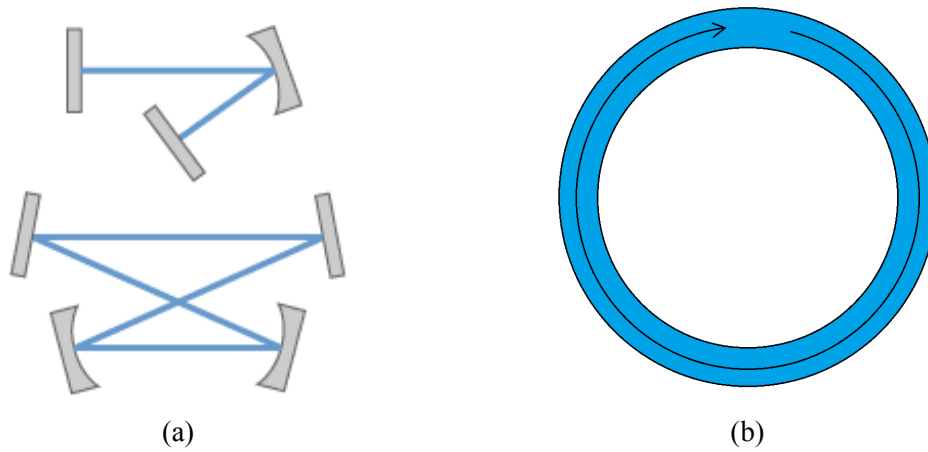


Figure 2.6: Examples of a) standing wave resonators [2] and b) traveling wave resonator

Some of the fundamental features characterizing resonators include:

- **The resonant frequency ( $f_0$ ).** The resonant frequency corresponds to the frequency at which the various waves involved in both the standing-wave and the travelling-wave resonators are added constructively with a phase difference equal to a multiple of  $2\pi$ . Assuming a path length  $L$ , the phase difference is expressed as:

$$\Delta\phi = \frac{2\pi n_{\text{eff}}}{\lambda} L = \frac{2\pi n_{\text{eff}} f}{c} L \quad (2.10)$$

Setting  $\Delta\phi$  equal to  $2\nu\pi$  we readily conclude that the resonant frequencies are given by:

$$f_0^\nu = \frac{c\nu}{n_{\text{eff}} L} \quad (2.11)$$

- **The resonator bandwidth ( $\Delta f$ ).** The field inside a resonator oscillates as  $e^{j2\pi f_0 t}$  but in practical situations it also decays due to resonator losses which can be intrinsic or due to

coupling with other structures. The resultant oscillations are described by  $e^{-\alpha/2t+j2\pi f_0 t}$  where  $\alpha > 0$  is a suitable attenuation coefficient. If we assume that these oscillations start at  $t = 0$  then it is straightforward to show that this corresponds to a spectrum:

$$A(f) = \frac{1}{\alpha/2 + j2\pi f} \quad (2.12)$$

This spectrum has a 3dB full width half maximum bandwidth (FWHM) at  $\Delta f = \alpha/2/\pi$ .

- **The quality factor ( $Q$ ).**  $Q$  is a dimensionless parameter that characterizes a resonator's bandwidth relative to its centre frequency and is equal to the ratio of the resonant frequency to the bandwidth of the cavity resonance. It is given by:

$$Q = \frac{f_0}{\Delta f} = \frac{2\pi f_0 E}{P} \quad (2.13)$$

where  $f_0$  is the resonant frequency,  $E$  is the stored energy in the cavity and  $P = -dE/dt$  is the power dissipated. The average lifetime of a resonant photon in the cavity is proportional to the cavity's  $Q$  [70].

- **The free spectral range (FSR).** Equation (2.11) suggest that the resonant frequencies of the structure are uniformly spaced. This periodicity is expressed through the FSR which denotes the spacing between the resonant frequencies,

$$\text{FSR} = f_0^{\nu+1} - f_0^\nu = \frac{c}{n_{\text{eff}}L} \quad (2.14)$$

As can be deduced from equation (2.14), due to the fact that the FSR is inversely proportional to the cavity length, the dimensions have to be small in order to achieve a high FSR and avoid crosstalk.

- **The finesse ( $F$ ).** The finesse  $F$  is the ratio of the FSR to the FWHM  $\Delta f$

$$F = \frac{\text{FSR}}{\Delta f} \quad (2.15)$$

and expresses the sharpness of the resonance compared to the spacing between the resonant frequencies.

In this dissertation we focus on traveling wave MRs. The MR is an integrated element fabricated by bending an optical waveguide to form a closed loop. The shape of this loop is typically a circle or a racetrack as shown in figure 2.6b. Light propagating in the MR waveguide interferes with itself after every trip around the ring. Constructive interference of light is obtained when the circumference of the loop  $2\pi R$  is exactly equal to an integer multiple of the guided wavelength  $\nu\lambda$ , implying a phase difference multiple of  $2\pi$ . This gives rise to sharp, Lorentzian-like resonances and large field intensity buildup inside the MR. The most important features of a MR are namely, the large field enhancement, the high wavelength selectivity, the high quality factor and the strong dispersion [63]. All the above render MR resonators extremely versatile and useful for a wide range of applications. These include signal processing, nonlinear optics, optical communication, quantum optics and sensing [69], [68].

## 2.7 Microring resonators

Figure 2.7a illustrates a ring resonator. The resonant condition of this device is given by  $\Delta\phi = 2\pi n_{\text{eff}}L/\lambda = 2\nu\pi$  with  $L = 2\pi R$  and  $R$  the radius of the ring [71]:

$$n_{\text{eff}}L = \nu\lambda \quad (2.16)$$

Figure 2.7b shows the transfer function of a MR device which is described by a sharp Lorentzian-like resonance [12], [72]. Much like the case of the simple Fabry-Perot cavity, the shape of the transfer function of such a single ring structure is not very attractive, when considered from a telecommunications application point-of-view. The reasons include the limited width of the pass-band which, in combination with the slowly decaying tails, limit the channel spacing in case the device is to be used as a WDM filter [1]. This is further illustrated in figure 2.7c which plots the transfer function over a wider frequency spacing where the periodicity of the transfer function is evident. The solution to the transfer function shape problem is to couple together several MRs in series. This improves the flatness in the passband and increases the decay rate at the tails rendering such devices more suitable for WDM applications.

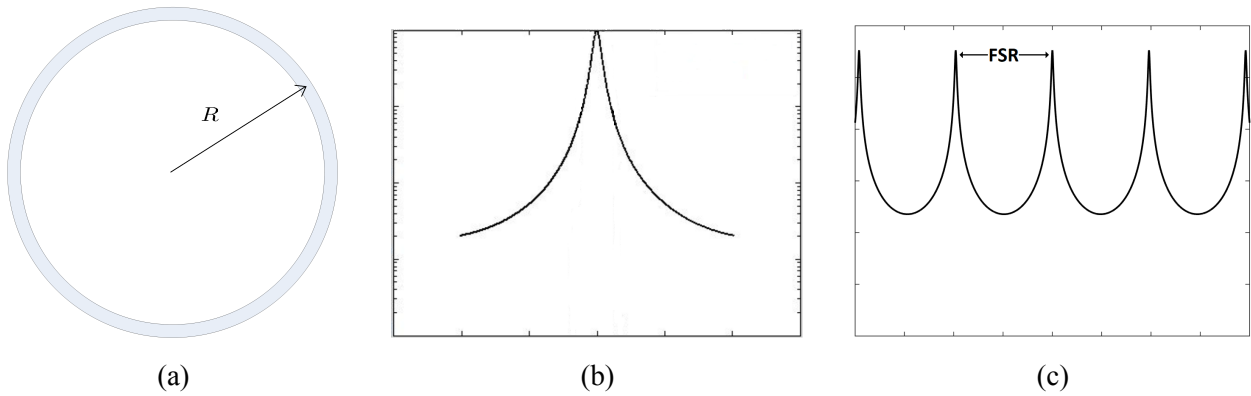


Figure 2.7: Depiction of a) a simple ring resonator, b) its transfer function in a single and c) multiple FSR range.

One of the main reasons for the increasing research interest in MRs, is the ability to fabricate them using the majority of the available photonic material platforms mentioned in section 2.4 including silicon [73], III–Vs [74], lithium niobate [75] and polymers [76].

In figure 2.8, we illustrate a simple waveguide/cavity system which is a four-port optical structure, consisting of a MR coupled to an input and an output waveguide. In the figure, we label the four ports as input (port 1), through (port 2), add (port 3), and drop (port 4). An optical signal is inserted in the system through port 1 and propagates in the lower waveguide until it exits the device through port 2. At the lower coupling region, some wavelengths  $\lambda_i$ , which satisfy the resonance condition may propagate in the ring in a counter-clockwise direction. Through the upper coupling region, these wavelengths may couple to the upper waveguide and exit from port 4. In the same manner, another wavelength which also satisfies the resonant condition,  $\lambda_n$ , can be inserted into the device through port 3. This wavelength will be added to the initial signal of waveguide 1, through the two coupling regions and will be finally received in port 2.

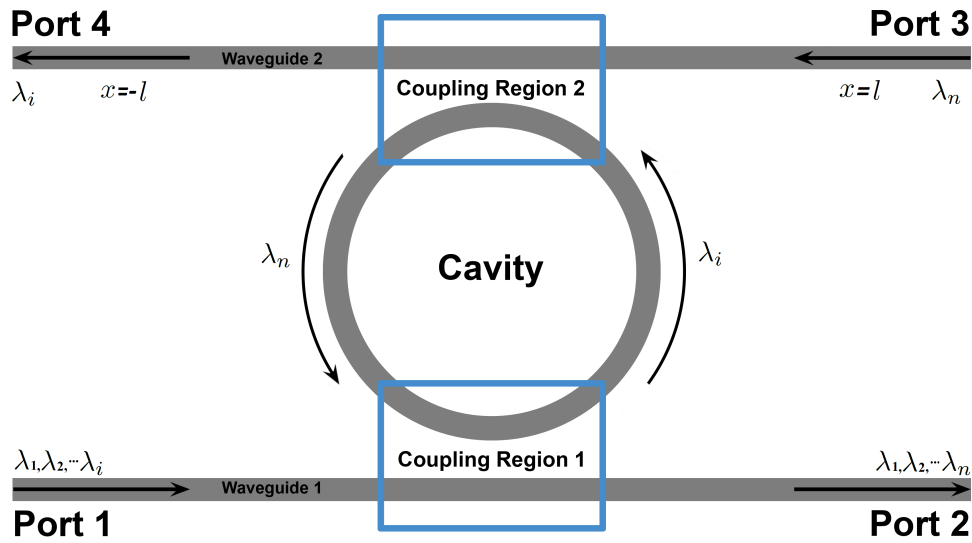


Figure 2.8: Representation of the simplest form of waveguide/cavity system

This device can be used as an add-drop filter in a WDM communication network allowing a wavelength channel from an input WDM signal that is in resonance with the MR, to be extracted to the drop port while, at the same time, allowing all other channels to proceed to the through port. In the same manner, a channel that is in resonance with the MR can be added onto the incoming WDM stream through the add port.

## 2.8 Multiple resonator structures

There are many possible ways in which multiple MRs can be combined to form a filter with more suitable properties. A coupled resonator optical waveguide (CROW) [77] is formed by placing the MRs along a path as shown in figure 2.9b. In this case light can hop from one ring to another. One can envision this series of MRs as a larger resonator in which many resonant frequencies are obtained around the resonant frequency  $f_0$  of the single ring. If the spacing between the rings is chosen carefully the superposition of the corresponding spectral peaks produces a flat top frequency response. An input and an output waveguide can be used to couple light to and from the structure. CROWs offer improved control over their dispersion characteristics and thus find applications in delay lines for storing and buffering of optical pulses through slow-light propagation [78] which can also enhance the non-linear response of the medium. In the majority of the cases, adjacent rings with the same radii are used, placed symmetrically along each other [79].

Alternatively, one can use a waveguide as in figure 2.9a to further enhance the coupling between the resonators. This device is called side-coupled integrated spaced sequence of resonators (SCISSOR) [80].

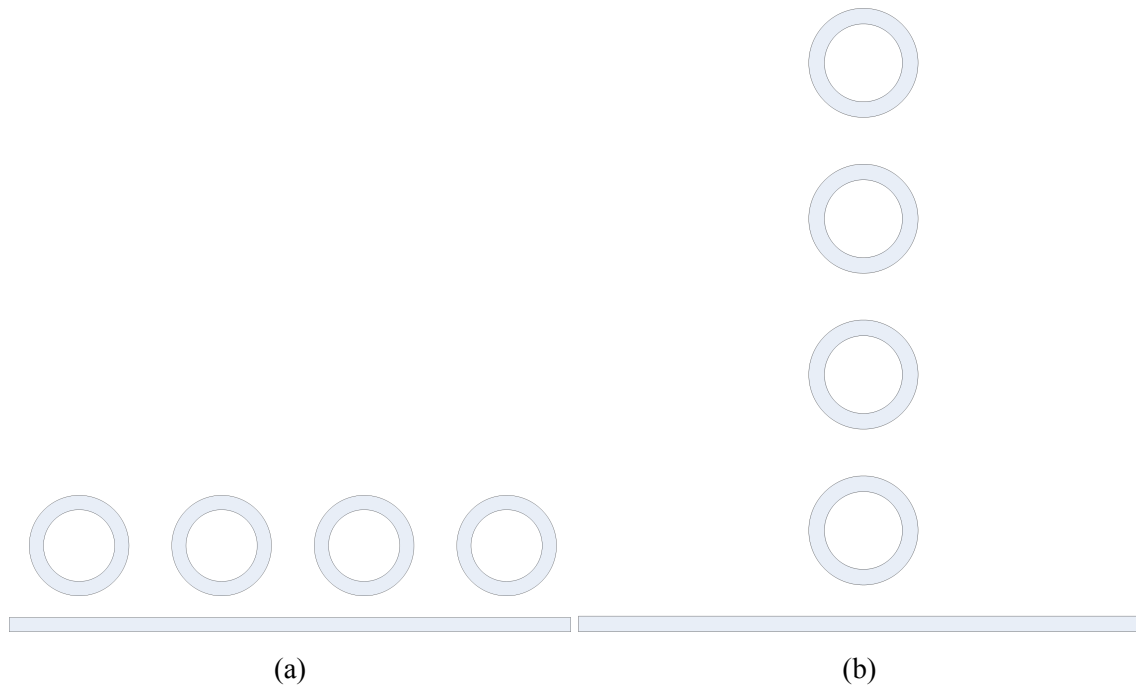


Figure 2.9: Multiple resonator structures: a) the SCISSOR geometry and b) the CROW geometry

In the SCISSOR case, if there is no resonator-to-resonator coupling, then light in all frequencies is transmitted in a feed-forward sequential manner from one resonator to the next “pausing” for localized feedback at each site. As a result, the optical properties of the structure do not depend on the spacing between neighboring resonators, but only the total number of resonators.

## 2.9 Applications of MRs

We have already discussed a basic add/drop functionality of the MR in section 2.7. MRs therefore constitute essential components in implementing OADMs and other network components [81], [82], [83], [84], [85]. MRs have also been proposed in a number of other applications including:

- **lasers:** Novel designs of three-terminal hybrid III–V-on-silicon lasers that integrate a metal-oxide-semiconductor (MOS) capacitor into the laser cavity using MRs, have been demonstrated. This approach enables a highly energy efficient method to tune both the output power and wavelength of MR lasers (figure 2.10a [3]). Additionally, a novel approach for achieving single mode lasing in MR lasers by increasing the radiation loss of all but one of the resonant modes of MR resonators by integrating second order gratings on the MRs’ waveguide, has been proposed (figure 2.10b [4]).

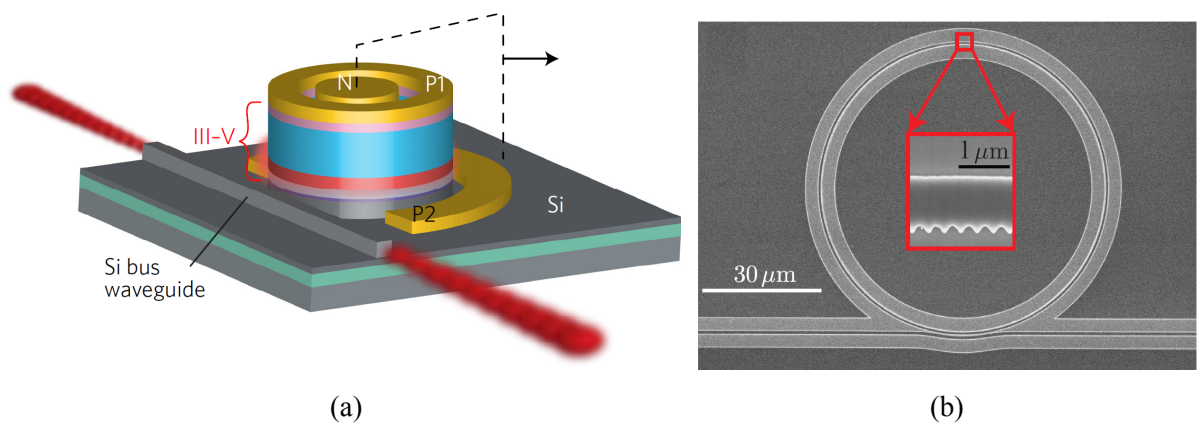


Figure 2.10: Depiction of a) three-terminal hybrid III–V-on-silicon [3] and b) laser-based on integrating second order gratings on the MRs' waveguide [4]

- switching elements:** Due to their high Q-factors and compact sizes, semiconductor MR resonators are the most appropriate candidates for fast optical switching applications. Such devices using micro-resonators can present up to ten times more enhanced field intensity in the ring and a finesse of the order of 100. This can lower the switching threshold by nearly four orders of magnitude. The carrier lifetime of the micro-cavity is found to be as short as a few picoseconds, allowing switching rates in the hundreds of gigahertz range in integrated form [86]. In addition,  $2 \times 2$  versions of silicon multi-wavelength switches have been demonstrated, which present switching transitions below 2 nanoseconds with up to 11.5dB extinction ratio at 10-Gb/s per channel data rates [87].
- optical gates:** MR resonators are one of the best competitors for the development of digital logic photonic integrated circuits, because of their planar and compact structure. Also, the absence of back reflections which are a major disadvantage of the Fabry-Perot type cavities, such as photonic crystals, is a major advantage. All-optical logic gates, based on symmetric GaAs–AlGaAs MR resonators with closely matched resonances, have been demonstrated. Furthermore, MR resonator based all optical gates have been reported [88]. In such structures, the use of more than one ring produces better cascading in photonic circuits due to the higher number of available ports. The switching energy of the gate is of the order of 20 pJ pulse, and the switching window is 40 ps, limited by the carrier lifetime (see figure 2.11) [5].

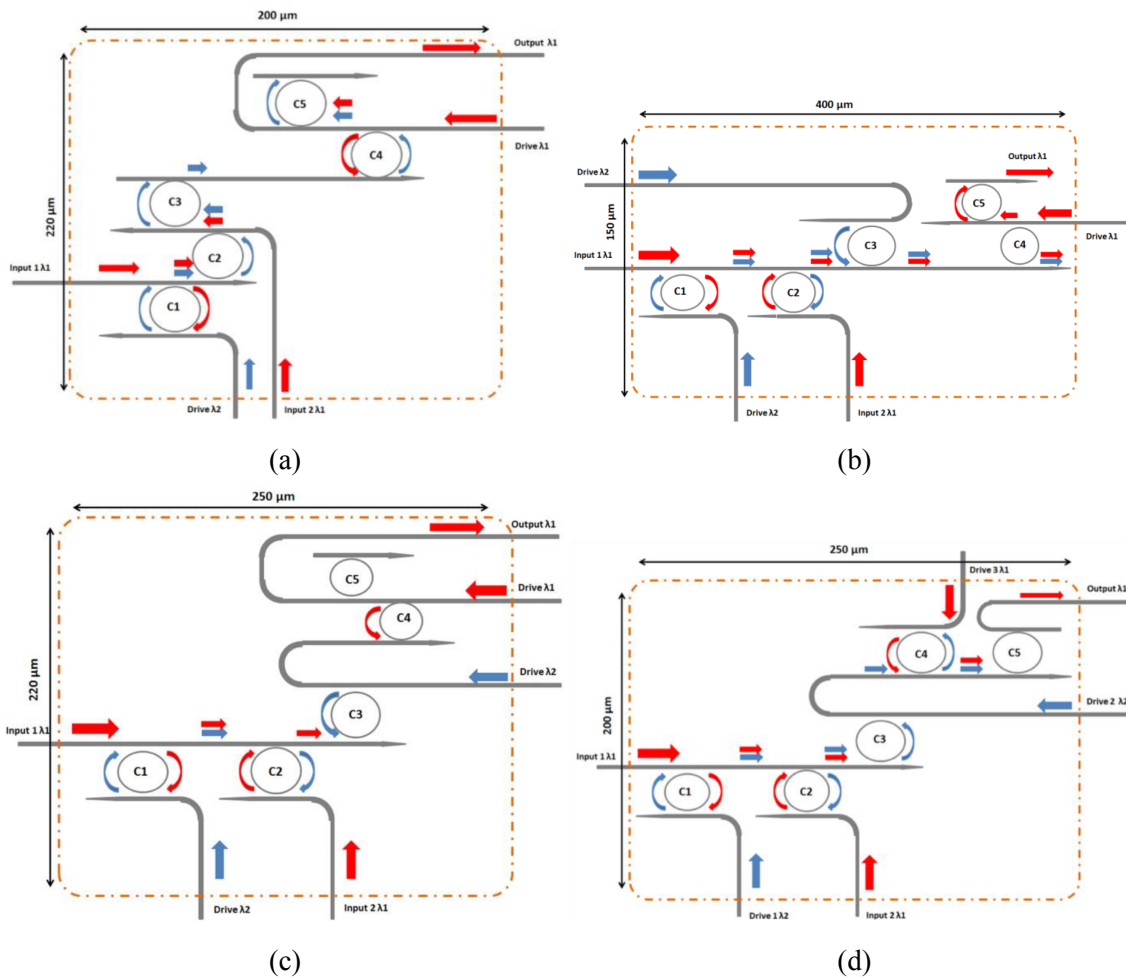


Figure 2.11: Depiction of an a) AND gate [5] b) OR gate [5] c) NOR gate [5] and d) XOR gate [5]

- optical modulators:** Electro-optical modulators utilizing MR resonators are critical components which enable optical interconnection systems on a microelectronic chip, in an attempt to meet the increasing bandwidth density demand that data centers and supercomputing systems require. Silicon modulators based on the free-carrier dispersion effect have been demonstrated [6]. Such modulators are either based on MOS capacitors or p-i-n diodes. Additionally, various schemes have been presented for the enhancement of the operation speed of the carrier-injection based p-i-n modulator (figure 2.12a). The major advantages of such devices include high-speed operation above 10 Gb/s, low power consumption, small device size and high modulation depth. Moreover, 40 Gb/s transmitters designed in 65nm CMOS which achieve 4 level pulse amplitude modulation on a single MR device have also been demonstrated (figure 2.12b) [7].

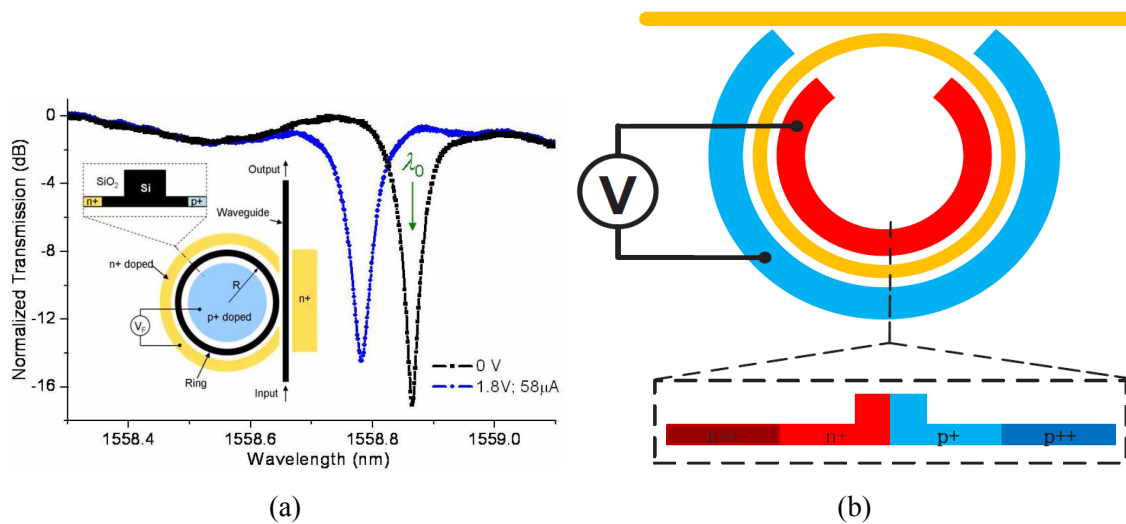


Figure 2.12: Depiction of the a) p-i-n modulator and its normalized transmission spectra [6] and b) top and cross-section views of a carrier-depletion MR modulator [7]

- optical signal processors:** Compact MR-assisted directional couplers in the silicon-on-insulator material system have been fabricated, designed to have a wide range of spectral characteristics, which include sharp asymmetric Fano line shapes, that can be utilized for WDM applications among others (figure 2.13a) [8]. Also, reconfigurable silicon thermo-optical devices have been demonstrated, which are able to tailor their intrinsic spectral optical response with the aid of the thermo-optical control of individual and uncoupled resonant modes of MRs (figure 2.13b). Such devices can be utilized to build up distinct and reconfigurable logic levels for optical signal processing usage [9].

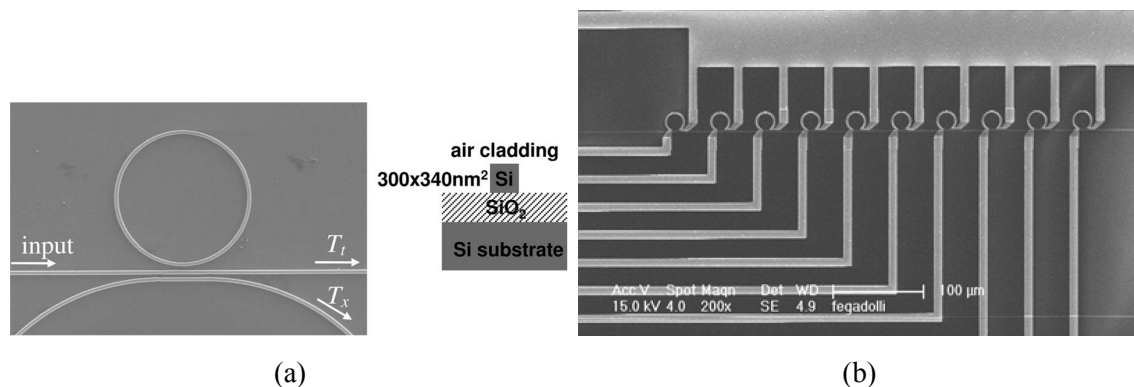


Figure 2.13: Depiction of a) compact MR-assisted directional couplers in the silicon-on-insulator material system [8] and b) reconfigurable silicon thermo-optical device [9]

- dispersion management:** A combination of various waveguide cross sections, in an aluminum nitride MR resonator can be used to control dispersion. Narrow waveguides with normal dispersion combined with wider ones with anomalous dispersion can be linked together with other tapering waveguides enclosed within a ring resonator, in order to produce a nearly zero device dispersion (figure 2.14) [10].

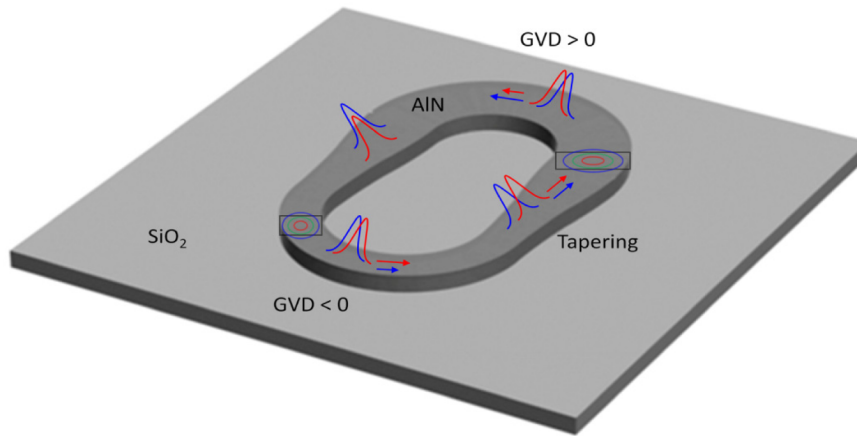


Figure 2.14: A multi-segment resonator that employs waveguides of different cross-sections for dispersion compensation. The red and blue curves are the light of longer and shorter wavelengths, respectively. The length of the arrows represent the speed of light for each wavelength in different waveguide sections. Mode profiles in narrow and wide waveguides are also sketched. The group velocity dispersion is either negative or positive depending on the material used [10]

## 2.10 Racetrack resonators

In order for a MR device to meet the required criteria, two basic parameters can be selected: the loss (gain) coefficient  $g_{avg}$  and the waveguide/MR coupling coefficient  $\kappa$ . The loss can be tailored by controlling the bending losses through proper design [89], the usage of different gain materials [90] and the clever matching of materials [91]. The coupling coefficient  $\kappa$  can be tuned by controlling the lateral coupling between the bus and ring waveguides. One way of realizing this is by vertically coupling the ring and the bus waveguide, which is a task that requires complex control and increased accuracy, hindering its applicability [92], [93], [94]. A simpler way to control the coupling coefficient is by using racetrack shaped resonator structures [95], [96], [97], as the one shown in figure 2.15.

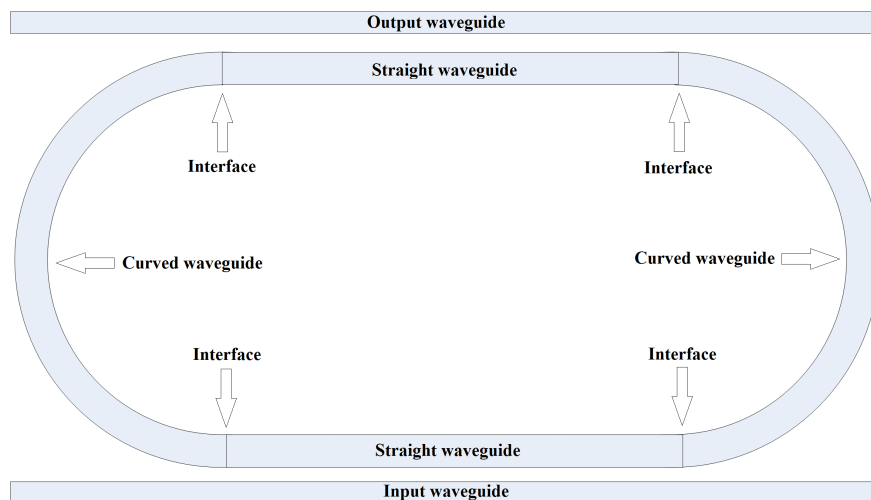


Figure 2.15: Representation of a RR structure

One of the advantages of this method is that conventional directional couplers are used, which makes the implementation simpler and more cost effective. The strength of the lateral coupling is determined by the length of the straight section of the RR. This characteristic however can also be a disadvantage as far as miniaturization is concerned. The increased losses due to the mode mismatch between the straight and the curved section of the RR along with the reflections at the interfaces are also considered a noticeable drawback of this approach. Important methods of reducing the impact of the mode mismatch have been presented in the past [91]. Alternatively however, intra-cavity reflections can provide additional degrees of freedom when designing a race-track/waveguide system. In [96], the authors have numerically shown that intra-cavity reflections in the active RRs result in various optical paths available to the oscillating field. The interference of these paths produces Fano resonances [98] that can be manipulated via gain tuning, by incorporating gain material [90] and then driving each of the waveguide's sections with different electrodes (separate current injections). Such Fano-type resonances can be utilized to implement various novel applications in the field of bio-sensing [99].

## 3 Design and simulation tools

### 3.1 Introduction

This chapter presents the basic tools for the analysis and design of coupled resonator/waveguide systems. As stated in 2.5.2 there are several tools for the analysis of such structures including direct solution of Maxwell's equations in the time or frequency domain as well as semi-analytical methods that take advantage of the specific nature of the coupling system. We begin with the latter since they can also provide greater insight in the device operation.

The term simulation describes the procedure where a set of parameters is utilized in combination with a mathematical model, in order to calculate the  $T(f)$  at the output of a structure. As can be easily understood, this means that the result of the calculations is unknown until they are completed and depends on the input parameter values used in the beginning. This fact is useful if the accuracy of a mathematical model is to be certified. This is done by comparing the results of this model with the results of other well established models, using the same set of input parameters. The idea behind our work however, has to do with the opposite procedure, i.e. the design of a structure: we need to find the best combination of the input parameters of a structure, in order to obtain a predetermined  $T(f)$  at its output.

The ideal filter response for telecommunication applications would be a box-like function  $T_0(f)$ :

$$T_0(f) = \begin{cases} 1 & , |f - f_0| \leq \frac{B}{2} \\ 0 & , \text{otherwise} \end{cases} \quad (3.1)$$

where  $B$  is the bandwidth. To measure how close a given transfer function  $T(f)$  is to our ideal box-like response  $T_0(f)$  we need to identify a metric  $d$ . One example could be:

$$d = \int_{f_a}^{f_b} |T(f) - T_0(f)|^2 df \quad (3.2)$$

We have empirically found however that attempting to match  $T(f)$  directly to a box-like transfer function  $T_0(f)$  in such a manner was often not practical since if the integration interval  $[f_a, f_b]$  was not chosen carefully, minimizing  $d$  could result in some peculiar looking  $T(f)$  which was of little interest from a practical point-of-view. Chapter 4 discusses a more fine choice for  $d$  in the case of the microring resonator. For the design of the RR structures for sensing applications in chapter 5 the problem was even more complex as it was not very clear what a reasonably attainable  $T_0(f)$  would look like. In this case we ended up choosing a metric  $d$  that involved some aspects of  $T(f)$  related to its behavior rather than its match to a particular ideal  $T_0(f)$ . In both cases the metric  $d = d(\mathbf{p})$  depends on the material and structural parameters  $\mathbf{p} = (p_1, \dots, p_N)$  of the device, i.e. the waveguide geometry, the number of resonators, etc. To optimize the design one should therefore minimize  $d(\mathbf{p})$ .

In practice, we expect that the fabrication process itself will impose limits on some or all the values of the parameters  $\mathbf{p}$ . We therefore need to perform the minimization on a finite interval.

This is a special case of constrained minimization where each parameter  $p_i$  must be kept within a pre-defined interval  $[p_i^{\min}, p_i^{\max}]$ .

There are a number of optimization methods typically used in the literature for the minimization of functions of multiple variables. If the number  $N$  of parameters is small, one could consider simply running an exhaustive search on a multidimensional grid of points  $\mathbf{p}_l$ . This is the method used in chapter 5. The interior-point algorithm is used in this thesis in chapter 4 since the number of design parameters is large and thus an exhaustive search is impractical. This algorithm transforms the original minimization problem,  $\min_{\mathbf{p}} d(\mathbf{p})$  to a series of approximate minimization problems involving only equalities as constraints. These problems are easier to solve using methods such as the conjugate gradient, etc. A detailed analysis of such optimization methods is out of the scope of this thesis and the interested reader is referred to [100] and [101] as well as the various textbooks in the area e.g. [102], [103].

### 3.2 Reciprocity relations

Reciprocity relations are instrumental in the derivation of the coupled mode equations as they can be used to relate the electromagnetic field components of two different structures. Let  $(\mathbf{E}_1, \mathbf{H}_1)$  and  $(\mathbf{E}_2, \mathbf{H}_2)$  be solutions of Maxwell's equations in the frequency domain corresponding to structures with dielectric constant  $\epsilon_1$  and  $\epsilon_2$  and frequencies  $\omega = \omega_1$  and  $\omega = \omega_2$  respectively, i.e.,

$$\nabla \times \mathbf{E}_1 = j\omega_1\mu\mathbf{H}_1 \quad (3.3a)$$

$$\nabla \times \mathbf{H}_1 = -j\omega_1\epsilon_1\mathbf{E}_1 \quad (3.3b)$$

$$\nabla \times \mathbf{E}_2 = j\omega_2\mu\mathbf{H}_2 \quad (3.4a)$$

$$\nabla \times \mathbf{H}_2 = -j\omega_2\epsilon_2\mathbf{E}_2 \quad (3.4b)$$

Let us define the vector function  $\mathbf{F}$  as follows:

$$\mathbf{F} = \mathbf{E}_1 \times \mathbf{H}_2^* + \mathbf{E}_2^* \times \mathbf{H}_1 \quad (3.5)$$

Assuming a planar surface  $S$  surrounded by a perimeter contour  $l$  on which  $\hat{\mathbf{n}}$  is the unit outward normal and  $\mathbf{z}$  is the unit vector orthogonal to  $S$ , we can write:

$$\int_S \nabla \cdot \mathbf{F} dS = \frac{\partial}{\partial z} \int_S \mathbf{F} \cdot \mathbf{z} dS + \oint_l \mathbf{F} \cdot \mathbf{n} dl \quad (3.6)$$

Using (3.5) we can calculate  $\nabla \cdot \mathbf{F}$  as:

$$\begin{aligned}
\nabla \cdot \mathbf{F} &= \nabla \cdot (\mathbf{E}_1 \times \mathbf{H}_2^* + \mathbf{E}_2^* \times \mathbf{H}_1) = \\
&= \mathbf{H}_2^* \cdot \nabla \times \mathbf{E}_1 - \mathbf{E}_1 \cdot \nabla \times \mathbf{H}_2^* + \mathbf{H}_1 \cdot \nabla \times \mathbf{E}_2^* - \mathbf{E}_2^* \cdot \nabla \times \mathbf{H}_1 = \\
&= j\omega_1 \mu \mathbf{H}_1 \cdot \mathbf{H}_2^* - j\omega_2 \epsilon_2 \mathbf{E}_1 \cdot \mathbf{E}_2^* - j\omega_2 \mu \mathbf{H}_1 \cdot \mathbf{H}_2^* + j\omega_1 \epsilon_1 \mathbf{E}_1 \cdot \mathbf{E}_2^* = \\
&= j\mu(\omega_1 - \omega_2) \mathbf{H}_1 \cdot \mathbf{H}_2^* + j(\omega_1 \epsilon_1 - \omega_2 \epsilon_2) \mathbf{E}_1 \cdot \mathbf{E}_2^*
\end{aligned} \tag{3.7}$$

We will now assume that  $S$  is a plane perpendicular to the propagation direction  $z$  and the fields vanish on  $l$ , i.e.

$$\oint_l \mathbf{F} \cdot \mathbf{n} dl = 0 \tag{3.8}$$

We can therefore combine (3.7) and (3.6) in order to obtain:

$$\frac{\partial}{\partial z} \int_S (\mathbf{E}_1 \times \mathbf{H}_2^* + \mathbf{E}_2^* \times \mathbf{H}_1) \cdot \mathbf{z} dS = j\mu(\omega_1 - \omega_2) \int_S \mathbf{H}_1 \cdot \mathbf{H}_2^* dS + \int_S j(\omega_1 \epsilon_1 - \omega_2 \epsilon_2) \mathbf{E}_1 \cdot \mathbf{E}_2^* dS \tag{3.9}$$

The reciprocity relation in (3.9) will be used to derive the coupled mode equations in the following sections.

### 3.3 Coupled mode theory

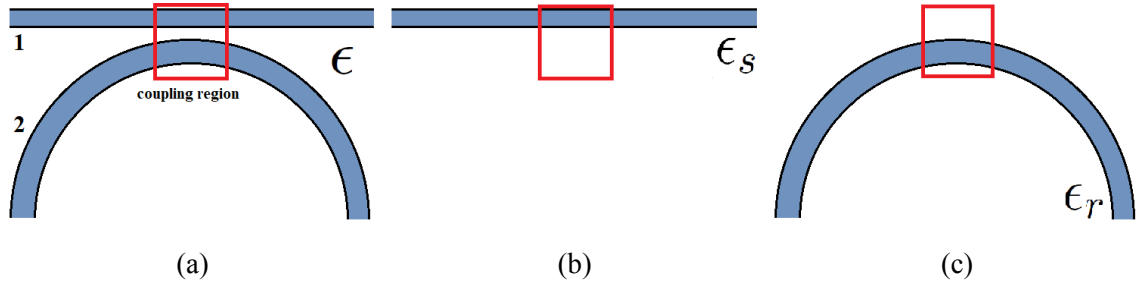


Figure 3.1: Depiction of a) coupling region, b) uncoupled straight and c) uncoupled ring waveguides.

Coupled mode theory is a general theoretical framework that describes the coupling of modes between waveguides and/or resonators. Given two or more coupled structures, the underlying idea is to expand the field as a superposition of the modes of the isolated individual structures. In the case of a straight waveguide coupled with a MR, we are interested in the analysis of the coupling region shown in figure 3.1a where the distance between the MR and the straight waveguide is small. The field in the straight waveguide can be written as:

$$\mathbf{E}_s = \mathbf{e}_s(x, y) e^{j\beta_s z} \tag{3.10a}$$

$$\mathbf{H}_s = \mathbf{h}_s(x, y) e^{j\beta_s z} \tag{3.10b}$$

As a first approximation, we can assume that the curvature of the ring waveguide is very small and hence the modal fields can be approximated by that of a straight waveguide as well,

$$\mathbf{E}_r = \mathbf{e}_r(x, y)e^{j\beta_r z} \quad (3.11a)$$

$$\mathbf{H}_r = \mathbf{h}_r(x, y)e^{j\beta_r z} \quad (3.11b)$$

The fields  $(\mathbf{E}_s, \mathbf{H}_s)$  and  $(\mathbf{E}_r, \mathbf{H}_r)$  obey Maxwell's equations for the straight and the ring waveguide respectively,

$$\nabla \times \mathbf{E}_s = j\omega\mu\mathbf{H}_s \quad (3.12a)$$

$$\nabla \times \mathbf{H}_s = -j\omega\epsilon_s\mathbf{E}_s \quad (3.12b)$$

$$\nabla \times \mathbf{E}_r = j\omega\mu\mathbf{H}_r \quad (3.13a)$$

$$\nabla \times \mathbf{H}_r = -j\omega\epsilon_r\mathbf{E}_r \quad (3.13b)$$

The dielectric constants  $\epsilon_s$  and  $\epsilon_r$  corresponding to the uncoupled straight and ring waveguides are illustrated in figures 3.1b and 3.1c. The total field  $(\mathbf{E}, \mathbf{H})$  inside the coupling region is written as a superposition of the isolated fields,

$$\mathbf{E} = a_r(z)\mathbf{E}_r + a_s(z)\mathbf{E}_s \quad (3.14a)$$

$$\mathbf{H} = a_r(z)\mathbf{H}_r + a_s(z)\mathbf{H}_s \quad (3.14b)$$

where  $a_s$  and  $a_r$  are the modal amplitudes along the propagation direction  $z$ . The total field obeys the following Maxwell's equations:

$$\nabla \times \mathbf{E} = j\omega\mu\mathbf{H} \quad (3.15a)$$

$$\nabla \times \mathbf{H} = -j\omega\epsilon\mathbf{E} \quad (3.15b)$$

We can now apply the reciprocity relation (3.9) to derive the coupled mode equations for the amplitudes  $a_r$  and  $a_s$ . We start by considering the functional  $\mathbf{F}_r = \mathbf{E} \times \mathbf{H}_r^* + \mathbf{E}_r^* \times \mathbf{H}$  and consider the left hand side of the reciprocity relation,

$$\begin{aligned} \frac{\partial}{\partial z} \int_S (\mathbf{E} \times \mathbf{H}_r^* + \mathbf{E}_r^* \times \mathbf{H}) \cdot \mathbf{z} dS = \\ \frac{\partial a_r}{\partial z} \int_S (\mathbf{E}_r \times \mathbf{H}_r^* + \mathbf{E}_r^* \times \mathbf{H}_r) \cdot \mathbf{z} dS + \frac{\partial a_s}{\partial z} \int_S (\mathbf{E}_s \times \mathbf{H}_r^* + \mathbf{E}_r^* \times \mathbf{H}_s) \cdot \mathbf{z} dS + \\ a_r \frac{\partial}{\partial z} \int_S (\mathbf{E}_r \times \mathbf{H}_r^* + \mathbf{E}_r^* \times \mathbf{H}_r) \cdot \mathbf{z} dS + a_s \frac{\partial}{\partial z} \int_S (\mathbf{E}_s \times \mathbf{H}_r^* + \mathbf{E}_r^* \times \mathbf{H}_s) \cdot \mathbf{z} dS \end{aligned} \quad (3.16)$$

We can assume that the mode fields are normalized so that,

$$\int_S (\mathbf{E}_r \times \mathbf{H}_r^* + \mathbf{E}_r^* \times \mathbf{H}_r) \cdot \mathbf{z} dS = \int_S (\mathbf{E}_s \times \mathbf{H}_s^* + \mathbf{E}_s^* \times \mathbf{H}_s) \cdot \mathbf{z} dS = 1 \quad (3.17)$$

Applying the reciprocity relations for  $\mathbf{F}_{sr} = \mathbf{E}_s \times \mathbf{H}_r^* + \mathbf{E}_r^* \times \mathbf{H}_s$  we obtain,

$$\kappa_{sr} = \frac{\partial}{\partial z} \int_S (\mathbf{E}_s \times \mathbf{H}_r^* + \mathbf{E}_r^* \times \mathbf{H}_s) \cdot \mathbf{z} dS = j\omega \int_S (\epsilon_s - \epsilon_r) \mathbf{E}_s \cdot \mathbf{E}_r^* dS \quad (3.18)$$

We therefore obtain,

$$\frac{\partial}{\partial z} \int_S (\mathbf{E} \times \mathbf{H}_r^* + \mathbf{E}_r^* \times \mathbf{H}) \cdot \mathbf{z} dS = \frac{\partial a_r}{\partial z} + \frac{\partial a_s}{\partial z} \Lambda_{sr} + a_s \kappa_{sr} \quad (3.19)$$

with

$$\Lambda_{sr} = \int_S (\mathbf{E}_s \times \mathbf{H}_r^* + \mathbf{E}_r^* \times \mathbf{H}_s) \cdot \mathbf{z} dS \quad (3.20)$$

Considering the right hand side of the reciprocity relation (3.9), we obtain,

$$\begin{aligned} \frac{\partial}{\partial z} \int_S (\mathbf{E} \times \mathbf{H}_r^* + \mathbf{E}_r^* \times \mathbf{H}) \cdot \mathbf{z} dS &= j\omega \int_S (\epsilon - \epsilon_r) \mathbf{E} \cdot \mathbf{E}_r^* dS = \\ &= j\omega a_r \int_S (\epsilon - \epsilon_r) \mathbf{E}_r \cdot \mathbf{E}_r^* dS + j\omega a_s \int_S (\epsilon - \epsilon_r) \mathbf{E}_s \cdot \mathbf{E}_r^* dS \end{aligned} \quad (3.21)$$

If we ignore the self coupling term,

$$j\omega a_r \int_S (\epsilon - \epsilon_r) \mathbf{E}_r \cdot \mathbf{E}_r^* dS \cong 0 \quad (3.22)$$

we can write:

$$\frac{\partial}{\partial z} \int_S (\mathbf{E} \times \mathbf{H}_r^* + \mathbf{E}_r^* \times \mathbf{H}) \cdot \mathbf{z} dS = j\omega a_s \int_S (\epsilon - \epsilon_r) \mathbf{E}_s \cdot \mathbf{E}_r^* dS \quad (3.23)$$

Combining (3.19) and (3.23), we obtain the following propagation equation,

$$\frac{\partial a_r}{\partial z} + \frac{\partial a_s}{\partial z} \Lambda_{sr} = j\kappa_s a_s \quad (3.24)$$

where we have defined,

$$\kappa_s = \omega \int_S (\epsilon - \epsilon_s) \mathbf{E}_s \cdot \mathbf{E}_r^* dS \quad (3.25)$$

In a similar manner we obtain,

$$\frac{\partial a_s}{\partial z} + \frac{\partial a_r}{\partial z} \Lambda_{rs} = j\kappa_r a_r \quad (3.26)$$

with

$$\Lambda_{rs} = \int_S (\mathbf{E}_r \times \mathbf{H}_s^* + \mathbf{E}_s^* \times \mathbf{H}_r) \cdot \mathbf{z} dS = \Lambda_{sr}^* \quad (3.27)$$

If we define the matrices  $\mathbf{C}$  and  $\mathbf{K}$  as follows:

$$\mathbf{C} = \begin{bmatrix} 1 & \Lambda_{rs} \\ \Lambda_{sr} & 1 \end{bmatrix} \quad (3.28)$$

$$\mathbf{K} = \begin{bmatrix} 0 & \kappa_r \\ \kappa_s & 0 \end{bmatrix} \quad (3.29)$$

and the vector  $\mathbf{a}$  as:

$$\mathbf{a} = \begin{bmatrix} a_s \\ a_r \end{bmatrix} \quad (3.30)$$

then we can write the propagation equations (3.24) and (3.26) as:

$$\frac{\partial \mathbf{a}}{\partial z} = j\mathbf{C}^{-1} \mathbf{K} \mathbf{a} \quad (3.31)$$

A formal solution to this system of equations is:

$$\mathbf{a}(l_c) = \exp\left(j \int_0^{l_c} \mathbf{C}^{-1} \mathbf{K} dz\right) \mathbf{a}(0) \quad (3.32)$$

where  $l_c$  is the length of the coupling region and  $\mathbf{a}(0)$  is the initial amplitude. Let  $\mathbf{M}$  be the matrix,

$$\mathbf{M} = \exp\left(j \int_0^{l_c} \mathbf{C}^{-1} \mathbf{K} dz\right) = \begin{bmatrix} m_{11} & m_{12} \\ m_{21} & m_{22} \end{bmatrix} \quad (3.33)$$

The amplitudes of the fields at the input and output of the coupling region in figure 3.1a are therefore determined by,

$$\begin{bmatrix} a_s(l_c) \\ a_r(l_c) \end{bmatrix} = \begin{bmatrix} m_{11} & m_{12} \\ m_{21} & m_{22} \end{bmatrix} \begin{bmatrix} a_s(0) \\ a_r(0) \end{bmatrix} \quad (3.34)$$

The parameters  $m_{pq}$  are the scattering parameters of the coupling region and  $\mathbf{M}$  is the scattering matrix.

### 3.4 Power flow

The matrix equation (3.34) reveals that the input and output amplitudes of the fields in the coupling region are related through a linear equation. Let us first consider the matrix  $\mathbf{C}$  which is given by (3.28) and (3.27). As indicated by (3.27) the non-diagonal elements of the matrix are the overlap of the fields in the ring and the straight waveguides. If we apply the reciprocity relation (3.9) we can show that:

$$\frac{\partial \Lambda_{rs}}{\partial z} = j\omega \int_S (\epsilon_r - \epsilon_s) \mathbf{E}_r \cdot \mathbf{E}_s^* dS \quad (3.35)$$

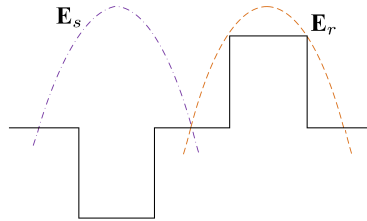


Figure 3.2: The distribution  $\epsilon_r - \epsilon_s$  along with the modal fields  $\mathbf{E}_s$  and  $\mathbf{E}_r$ .

We therefore see that the variation of  $\Lambda_{rs}$  along the propagation equation is determined by the integral of  $(\epsilon_r - \epsilon_s) \mathbf{E}_r \cdot \mathbf{E}_s$  over the plane  $S$ . Let us assume that the ring and straight waveguide have similar cross-sections and that their modes are also similar. In this case  $\mathbf{E}_r$  can be considered a displaced version of  $\mathbf{E}_s$ . Figure 3.2 illustrates the one-dimensional analog of the quantities involved in (3.35). Based on the figure, we see that the integral in (3.35) comprises of nearly anti-symmetric contributions which cancel one another: one inside the ring waveguide and one in the straight waveguide. We therefore expect:

$$\frac{\partial \Lambda_{rs}}{\partial z} \cong 0 \quad (3.36)$$

At the input of the coupling region, we expect that the overlap between the fields  $\mathbf{E}_s, \mathbf{H}_s$  and  $\mathbf{E}_r, \mathbf{H}_r$  is negligible since the waveguides are placed far apart. Hence we can assume that,

$$\Lambda = \Lambda_{rs} = \int_S (\mathbf{E}_r \times \mathbf{H}_s^* + \mathbf{E}_s^* \times \mathbf{H}_r) \cdot \mathbf{z} dS \cong 0 \quad (3.37)$$

This implies that the matrix  $\mathbf{C}$  can be approximated by the identity matrix,

$$\mathbf{C} = \begin{bmatrix} 1 & \Lambda_{rs} \\ \Lambda_{sr} & 1 \end{bmatrix} \cong \begin{bmatrix} 1 & 0 \\ 0 & 1 \end{bmatrix} \quad (3.38)$$

The fields obeying:

$$\int_S (\mathbf{E}_1 \times \mathbf{H}_2^* + \mathbf{E}_2^* \times \mathbf{H}_1) \cdot \mathbf{z} dS = 0 \quad (3.39)$$

are said to be orthogonal. We therefore conclude that the fields  $\mathbf{E}_s, \mathbf{H}_s$  and  $\mathbf{E}_r, \mathbf{H}_r$  can be considered orthogonal and this orthogonality is approximately maintained throughout the coupling region. This simplifies the calculation of the power flow through the coupling region. The power along the propagation equation is given by Poynting's theorem,

$$P_z = \int_S (\mathbf{E} \times \mathbf{H}^* + \mathbf{E}^* \times \mathbf{H}) \cdot \mathbf{z} dS \quad (3.40)$$

Substituting the field expansion (3.14) in (3.40) and using the normalization condition (3.17) along with the orthogonality condition (3.37) we can obtain:

$$P_z = |a_s|^2 + |a_r|^2 \quad (3.41)$$

### 3.5 Lossless coupling region

(3.41) illustrates that the power flow along the propagation direction is given by the sum of the squares of the amplitudes of the propagating modes. Assuming that the coupling region is lossless, the input and output amplitudes are related through,

$$|a_s(0)|^2 + |a_r(0)|^2 = |a_s(l_c)|^2 + |a_r(l_c)|^2 \quad (3.42)$$

This imposes certain conditions on the structure of the matrix  $\mathbf{M}$ . Denoting  $\{.\}^T$  the conjugate transpose, then:

$$\mathbf{a}^T(z)\mathbf{a}(z) = |a_s(z)|^2 + |a_r(z)|^2 \quad (3.43)$$

Hence,

$$|a_s(l_c)|^2 + |a_r(l_c)|^2 = \mathbf{a}^T(l_c)\mathbf{a}(l_c) = \mathbf{a}^T(0)(\mathbf{M}^T\mathbf{M})\mathbf{a}(0) \quad (3.44)$$

and the lossless condition translates to:

$$\mathbf{M}^T\mathbf{M} = \mathbf{I} \quad (3.45)$$

where  $\mathbf{I}$  is the identity matrix. The above equations translate to:

$$|m_{11}|^2 + |m_{21}|^2 = 1 \quad (3.46a)$$

$$|m_{12}|^2 + |m_{22}|^2 = 1 \quad (3.46b)$$

$$m_{11}^* m_{12} + m_{21}^* m_{22} = 0 \quad (3.46c)$$

Using some mathematical manipulation we can show that the elements of the matrix are related as follows:

$$|m_{11}| = |m_{22}| \quad (3.47a)$$

$$|m_{12}| = |m_{21}| \quad (3.47b)$$

We note that if the straight and ring waveguides are symmetrical we expect that  $\kappa_r = \kappa_s^*$  and the matrix  $\mathbf{K}$  can be written as,

$$\mathbf{K} = \begin{bmatrix} 0 & \kappa_s \\ \kappa_s^* & 0 \end{bmatrix} \quad (3.48)$$

Since the matrix  $\mathbf{C}$  is Hermitian we expect that the matrix  $\mathbf{C}^{-1}\mathbf{K}$  is also Hermitian. Especially in view of (3.38), we can approximate  $\mathbf{C}^{-1}\mathbf{K} \cong \mathbf{K}$  and hence:

$$\mathbf{m} = j \int_0^{l_c} \mathbf{C}^{-1}\mathbf{K}dz \cong j \int_0^{l_c} \mathbf{K}dz = \begin{bmatrix} 0 & jK \\ jK^* & 0 \end{bmatrix} \quad (3.49)$$

where  $K$  is the cumulative coupling coefficient over the coupling region,

$$K = \int_0^{l_c} \kappa_s dz \quad (3.50)$$

Lets consider the matrix  $\mathbf{I}$  given by,

$$\mathbf{I} = \begin{bmatrix} 0 & K \\ K^* & 0 \end{bmatrix} \quad (3.51)$$

which is Hermitian and has eigenvalues equal to  $\pm|K|$ , while the eigenvectors  $(v_1, v_2)$  are determined by:

$$\begin{bmatrix} 0 & K \\ K^* & 0 \end{bmatrix} \begin{bmatrix} v_1 \\ v_2 \end{bmatrix} = \pm|K| \begin{bmatrix} v_1 \\ v_2 \end{bmatrix} \quad (3.52)$$

which implies that  $v_2 = \pm v_1 e^{j\phi_K}$ , where  $\phi_K$  is the phase of  $K$ . We can easily show that:

$$\mathbf{v} = \frac{1}{\sqrt{2}} \begin{bmatrix} e^{j\phi_K/2} \\ \pm e^{j\phi_K/2} \end{bmatrix} \quad (3.53)$$

are normalized eigenvectors corresponding to the eigenvalues  $\pm|K|$ . Constructing the unitary matrix with the eigenvectors as columns,

$$\mathbf{U} = \frac{1}{\sqrt{2}} \begin{bmatrix} e^{j\phi_K/2} & e^{j\phi_K/2} \\ e^{-j\phi_K/2} & -e^{-j\phi_K/2} \end{bmatrix} \quad (3.54)$$

and the diagonal matrix,

$$\mathbf{D} = \begin{bmatrix} |K| & 0 \\ 0 & -|K| \end{bmatrix} \quad (3.55)$$

we can readily see that  $\mathbf{I}$  can be diagonalized as:

$$\mathbf{I} = \mathbf{U}\mathbf{D}\mathbf{U}^T = \frac{1}{2} \begin{bmatrix} e^{j\phi_K/2} & e^{j\phi_K/2} \\ e^{-j\phi_K/2} & -e^{-j\phi_K/2} \end{bmatrix} \begin{bmatrix} 0 & |K| \\ -|K| & 0 \end{bmatrix} \begin{bmatrix} e^{-j\phi_K/2} & e^{j\phi_K/2} \\ e^{-j\phi_K/2} & -e^{j\phi_K/2} \end{bmatrix} \quad (3.56)$$

The exponential  $\exp(j\mathbf{l})$  can be computed as:

$$\mathbf{M} = \exp(j\mathbf{l}) = \frac{1}{2} \begin{bmatrix} e^{j\phi_K/2} & e^{j\phi_K/2} \\ e^{-j\phi_K/2} & -e^{-j\phi_K/2} \end{bmatrix} \begin{bmatrix} 0 & \exp(j|K|) \\ \exp(-j|K|) & 0 \end{bmatrix} \begin{bmatrix} e^{-j\phi_K/2} & e^{j\phi_K/2} \\ e^{-j\phi_K/2} & -e^{j\phi_K/2} \end{bmatrix} \quad (3.57)$$

which is also written as:

$$\mathbf{M} = \begin{bmatrix} \cos(|K|) & j \sin(|K|) e^{j\phi_K} \\ j \sin(|K|) e^{-j\phi_K} & \cos(|K|) \end{bmatrix} \quad (3.58)$$

We can define the power coupling coefficient  $\kappa$  and the power transmission coefficient  $\tau$  as:

$$\tau = \cos^2(|K|) \quad (3.59a)$$

$$\kappa = \sin^2(|K|) \quad (3.59b)$$

$$(3.59c)$$

in which case the scattering matrix is written as:

$$\mathbf{M} = \begin{bmatrix} \sqrt{\tau} & j\sqrt{\kappa} e^{j\phi_K} \\ j\sqrt{\kappa} e^{-j\phi_K} & \sqrt{\tau} \end{bmatrix} \quad (3.60)$$

We readily obtain,

$$\tau + \kappa = \cos^2(K) + \sin^2(K) = 1 \quad (3.61)$$

The scattering matrix (3.60) describes the evolution of the fields inside the coupling region as a result of which the fields may obtain a phase difference  $\phi_K$ . If we assume that the propagation constant is the same in the straight and the ring waveguide, we expect that:

$$\mathbf{E}_s \cdot \mathbf{E}_r^* = \mathbf{e}_s \cdot \mathbf{e}_r^* \quad (3.62)$$

and hence we expect that:

$$\kappa_s = \omega \int_S (\epsilon - \epsilon_s) \mathbf{E}_s \cdot \mathbf{E}_r^* dS = \omega \int_S (\epsilon - \epsilon_s) \mathbf{e}_s \cdot \mathbf{e}_r^* dS \quad (3.63)$$

We can choose the modal fields  $\mathbf{e}_s$  and  $\mathbf{e}_r$  so that  $\kappa_s$  is real and hence  $\phi_K = 0$ . This implies that:

$$\mathbf{M} = \begin{bmatrix} \sqrt{\tau} & j\sqrt{\kappa} \\ j\sqrt{\kappa} & \sqrt{\tau} \end{bmatrix} \quad (3.64)$$

### 3.6 Transfer function calculation

The transfer matrix method is essential in the analysis of more complex coupled structures and essentially amounts to breaking down a larger structure into basic building blocks, each described by a matrix  $M_i$ . In our case we will consider uncoupled waveguides and coupling regions. Later on we will consider reflections arising inside RRs that can also be described by a matrix.

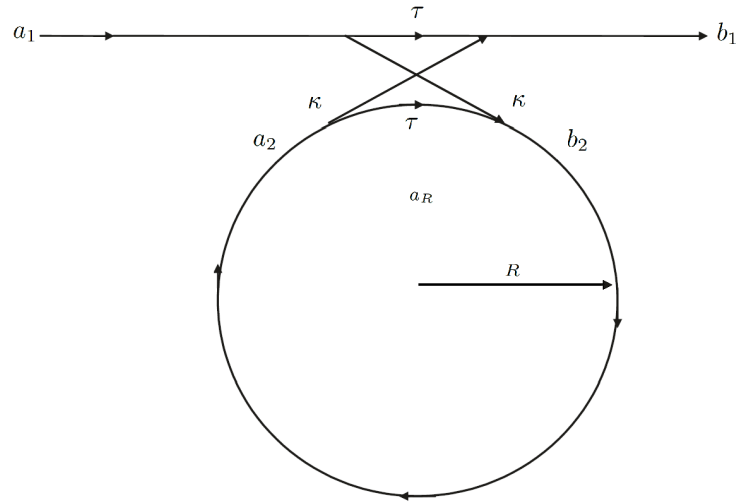


Figure 3.3: Representation of a simple waveguide/ring system

Referring to figure 3.3, we can relate the input  $(a_1, a_2)$  and output amplitudes  $(b_1, b_2)$  at the coupling region,

$$\begin{bmatrix} b_1 \\ b_2 \end{bmatrix} = \begin{bmatrix} \sqrt{\tau} & j\sqrt{\kappa} \\ j\sqrt{\kappa} & \sqrt{\tau} \end{bmatrix} \begin{bmatrix} a_1 \\ a_2 \end{bmatrix} \quad (3.65)$$

The amplitude  $a_2$  is related to the amplitude  $b_2$  through the following relation:

$$a_2 = e^{-(j\phi + 2a_R\pi R)} b_2 \quad (3.66)$$

where  $a_R$  is the loss coefficient in the ring and depends on the material,  $R$  is the ring radius  $\phi$  is the roundtrip phase shift,

$$\phi = \frac{2\pi n_{\text{eff}} 2\pi R}{\lambda} \quad (3.67)$$

where  $n_{\text{eff}}$  is the effective refractive index of the ring waveguide. Using (3.65) and (3.66) we obtain the following relation:

$$H = \frac{b_1}{a_1} = \left( \frac{\sqrt{\tau} - e^{-(j\phi + 2a_R\pi R)}}{1 - e^{-(j\phi + 2a_R\pi R)} \sqrt{\tau}} \right) \quad (3.68)$$

where  $H$  is the amplitude transfer function of the device, relating the input and output amplitudes in the straight waveguide. The power transfer function  $T = |H|^2$ , is obtained as:

$$T = \left| \frac{b_1}{a_1} \right|^2 = \left| \frac{\sqrt{\tau} - e^{-(j\phi + 2a_R\pi R)}}{1 - e^{-(j\phi + 2a_R\pi R)} \sqrt{\tau}} \right|^2 \quad (3.69)$$

An example of  $T$  for the single ring case is presented in figure 3.4. A ring of radius  $R=14.7\mu\text{m}$  was used with  $\kappa = 0.3$ . The  $n_{\text{eff}}$  was considered to be 3.3 which is typical for silicon waveguides. The transfer function is plotted in terms of  $\delta f = f - f_0$  where  $f_0 = 196$  THz corresponding to a free space wavelength of  $\lambda_0 = 1.531\mu\text{m}$ .

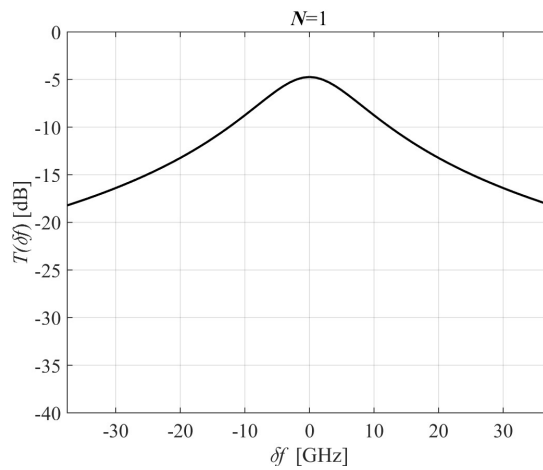


Figure 3.4: Representation of a single ring MR system transmission coefficient

The above analysis can be extended in the case of multiple rings and waveguides. Consider the double ring structure shown in figure 3.5 which depicts a serially coupled double ring resonator structure.

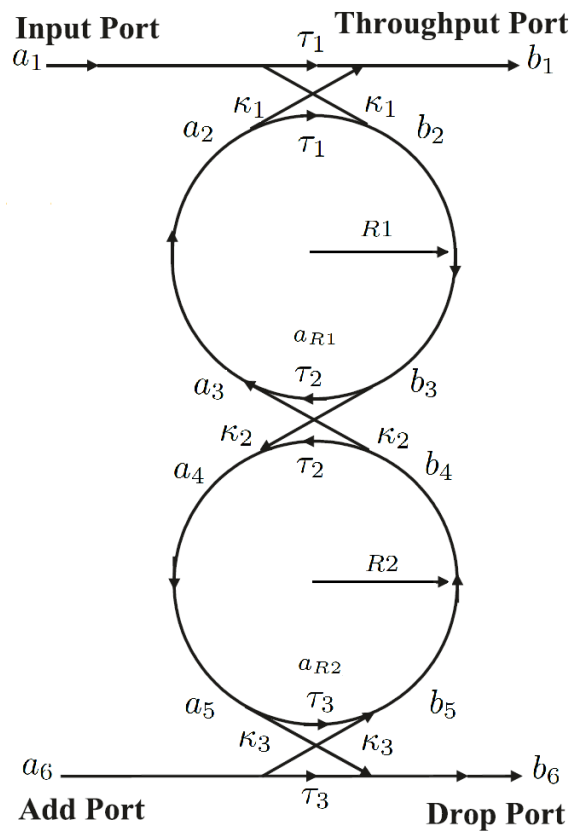


Figure 3.5: Representation of a double ring MR system where the rings are placed in series

It consists of two straight waveguides and two ring waveguides. We first start by writing

down the equations relating the input and output fields in the three coupling regions:

$$\begin{bmatrix} b_1 \\ b_2 \end{bmatrix} = \begin{bmatrix} \sqrt{\tau_1} & j\sqrt{\kappa_1} \\ j\sqrt{\kappa_1} & \sqrt{\tau_1} \end{bmatrix} \begin{bmatrix} a_1 \\ a_2 \end{bmatrix} \quad (3.70a)$$

$$\begin{bmatrix} a_3 \\ a_4 \end{bmatrix} = \begin{bmatrix} \sqrt{\tau_2} & j\sqrt{\kappa_2} \\ j\sqrt{\kappa_2} & \sqrt{\tau_2} \end{bmatrix} \begin{bmatrix} b_3 \\ b_4 \end{bmatrix} \quad (3.70b)$$

$$\begin{bmatrix} b_5 \\ b_6 \end{bmatrix} = \begin{bmatrix} \sqrt{\tau_3} & j\sqrt{\kappa_3} \\ j\sqrt{\kappa_3} & \sqrt{\tau_3} \end{bmatrix} \begin{bmatrix} a_5 \\ a_6 \end{bmatrix} \quad (3.70c)$$

where  $\kappa_i$  and  $\tau_i$  are the power coupling and transmission coefficients of the  $i^{\text{th}}$  coupling region. The propagation equations for the ring waveguides are written as:

$$a_2 = e^{-(j\frac{\phi_1}{2} + a_{R1}\pi R1)} a_3 \quad (3.71a)$$

$$b_3 = e^{-(j\frac{\phi_1}{2} + a_{R1}\pi R1)} b_2 \quad (3.71b)$$

$$a_5 = e^{-(j\frac{\phi_2}{2} + a_{R2}\pi R2)} a_4 \quad (3.71c)$$

$$b_4 = e^{-(j\frac{\phi_2}{2} + a_{R2}\pi R2)} b_5 \quad (3.71d)$$

where  $\phi_1, \phi_2$  and  $R_1, R_2$  represent the phase shifts and radii of the first and second ring respectively. If we assume that no signal enters in the add port in figure 3.5 then  $a_6=0$ . Equations (3.70) and the (3.71) constitute a system of ten equations which can be used to calculate the unknown amplitudes. In the case where the rings are weakly coupled, we can assume that the clockwise propagating wave on the first ring ( $a_3$ ) exiting the coupling region between the first and second ring, inside the first ring, is negligible with amplitude  $a_3 = j\sqrt{\kappa_2}b_4 + \sqrt{\tau_2}b_3$  and thus can be approximated as  $a_3 \cong \sqrt{\tau_2}b_3$ . After some mathematical manipulation we end up to the solution of the equations system with respect to  $T$ :

$$T = \frac{(1 - \tau_1)(1 - \tau_2)(1 - \tau_3)e^{-2a_{R1}\pi R1}e^{-2a_{R2}\pi R2}}{|1 - \sqrt{\tau_1\tau_2}e^{-(j\phi_1 + a_{R1})2\pi R1}|^2|1 - \sqrt{\tau_2\tau_3}e^{-(j\phi_2 + a_{R2})2\pi R2}|^2} \quad (3.72)$$

In the general case of  $N$  rings, making the same assumptions, the transmission coefficient  $T$  can be obtained by:

$$T = (1 - \tau_{N+1}) \prod_{n=1}^N \frac{(1 - \tau_n)e^{-2a_{Rn}\pi Rn}e^{-2a_{Rn}\pi Rn}}{|1 - \sqrt{\tau_n\tau_{n+1}}e^{-(j\phi_n + a_{Rn})2\pi Rn}|^2} \quad (3.73)$$

An example of  $T$  for the double ring case is presented in figure 3.6. In this case we have assumed that  $f_0 = 196$  THz and  $n_{\text{eff}} = 3.3$  just as in figure 3.4. Also  $\kappa_1 = \kappa_3 = 0.3$ ,  $\kappa_2 = 0.08$ ,  $R_1 = 24.6\mu\text{m}$  and  $R_2 = 17\mu\text{m}$ .

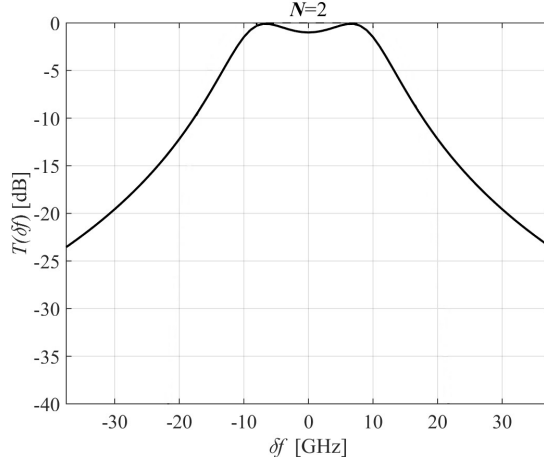


Figure 3.6: Representation of a double ring MR system transmission coefficient

## 3.7 Finite difference frequency domain method

### 3.7.1 Yee's grid

In the previous sections we have provided a coupling of modes analysis of coupled resonator structures. The modal fields are important in the estimation of the coupling coefficients, e.g. in (3.25). In chapter 2, we have given an example of how approximate methods such as the effective index method (section 2.5.2) can be used to obtain an approximation of the modal fields  $\mathbf{E}_s$  and  $\mathbf{E}_r$ . Although computationally efficient, one may encounter cases where such methods are not accurate (e.g. high-index contrast structures) or not applicable altogether (e.g. non rectangular shaped waveguides). In this section we present an alternative method of estimating the modal fields based on finite differences, namely the finite difference frequency domain method which utilizes the finite differences approximation to replace derivatives in Maxwell's equations [79], for example:

$$\frac{\partial E_z(x, y)}{\partial y} \approx \frac{E_z(x, y + \frac{1}{2}\Delta y) - E_z(x, y - \frac{1}{2}\Delta y)}{\Delta y} \quad (3.74)$$

By properly choosing the points where the derivatives are approximated, one can cast the differential problem of equations (2.9) into an eigenvalue problem whose solution is much more straightforward. Yee's grid is a very popular choice of points [104], [105] and is depicted in figure 3.7. To simplify the notation in the subsequent equations, we omit the grid spacing  $\Delta x$  and  $\Delta y$  in the field arguments. Hence  $E_z(i, j)$  stands for  $E_z(i\Delta x, j\Delta y)$  and  $E_y(i, j + \frac{1}{2})$  stands for  $E_y(i\Delta x, (j + \frac{1}{2})\Delta y)$ .

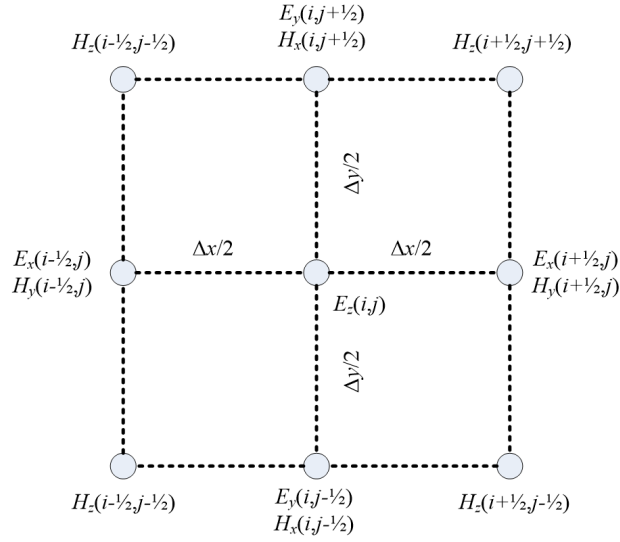


Figure 3.7: The two dimensional Yee's grid

Adopting Yee's grid, (2.9) become:

$$\frac{E_z(i, j+1) - E_z(i, j)}{\Delta y} - j\beta E_y(i, j + \frac{1}{2}) = j\omega\mu_0 H_x(i, j + \frac{1}{2}) \quad (3.75a)$$

$$\frac{E_z(i+1, j) - E_z(i, j)}{\Delta x} - j\beta E_x(i + \frac{1}{2}, j) = -j\omega\mu_0 H_y(i + \frac{1}{2}, j) \quad (3.75b)$$

$$\frac{E_y(i+1, j + \frac{1}{2}) - E_y(i, j + \frac{1}{2})}{\Delta x} - \frac{E_x(i + \frac{1}{2}, j+1) - E_x(i + \frac{1}{2}, j)}{\Delta y} = j\omega\mu_0 H_z(i + \frac{1}{2}, j + \frac{1}{2}) \quad (3.75c)$$

$$\frac{H_z(i + \frac{1}{2}, j + \frac{1}{2}) - H_z(i + \frac{1}{2}, j - \frac{1}{2})}{\Delta y} - j\beta H_y(i + \frac{1}{2}, j) = -j\omega\varepsilon E_x(i + \frac{1}{2}, j) \quad (3.75d)$$

$$\frac{H_z(i + \frac{1}{2}, j + \frac{1}{2}) - H_z(i - \frac{1}{2}, j + \frac{1}{2})}{\Delta x} - j\beta H_x(i, j + \frac{1}{2}) = j\omega\varepsilon E_y(i, j + \frac{1}{2}) \quad (3.75e)$$

$$\frac{H_y(i + \frac{1}{2}, j) - H_y(i - \frac{1}{2}, j)}{\Delta x} - \frac{H_x(i, j + \frac{1}{2}) - H_x(i, j - \frac{1}{2})}{\Delta y} = -j\omega\varepsilon E_z(i, j) \quad (3.75f)$$

$$j\beta E_z(i, j) + \frac{E_x(i + \frac{1}{2}, j) - E_x(i - \frac{1}{2}, j)}{\Delta x} + \frac{E_y(i, j + \frac{1}{2}) - E_y(i, j - \frac{1}{2})}{\Delta y} = 0 \quad (3.75g)$$

$$j\beta H_z(i + \frac{1}{2}, j + \frac{1}{2}) + \frac{H_x(i + 1, j + \frac{1}{2}) - H_x(i, j + \frac{1}{2})}{\Delta x} + \frac{H_y(i + \frac{1}{2}, j + 1) - H_y(i + \frac{1}{2}, j)}{\Delta y} = 0 \quad (3.75h)$$

The field components in equations (3.75) are only calculated at the points determined from the Yee grid.

### 3.7.2 Eigenvalue problems

These equations can be re-written in a matrix form, using the column vectors  $\mathbf{e}_x$ ,  $\mathbf{e}_y$ ,  $\mathbf{e}_z$ ,  $\mathbf{h}_x$ ,  $\mathbf{h}_y$  and  $\mathbf{h}_z$  which are correlated with the fields at the Yee's grid points via the following equations:

$$e_x(p) = e_x(i + \frac{1}{2}, j) \quad (3.76a)$$

$$e_y(p) = e_y(i, j + \frac{1}{2}) \quad (3.76b)$$

$$e_z(p) = e_z(i, j) \quad (3.76c)$$

$$h_x(p) = h_x(i, j + \frac{1}{2}) \quad (3.76d)$$

$$h_y(p) = h_y(i + \frac{1}{2}, j) \quad (3.76e)$$

$$h_z(p) = h_z(i + \frac{1}{2}, j + \frac{1}{2}) \quad (3.76f)$$

where  $p = (j - 1)N_x + i$  and  $N_x$  is the number of points at the x-axis. Consequently, equations (3.75) can be re-written as:

$$\frac{e_z(p + N_x) - e_z(p)}{\Delta y} - j\beta e_y(p) = j\omega\mu_0 h_x(p) \quad (3.77a)$$

$$- \frac{e_z(p + 1) - e_z(p)}{\Delta x} + j\beta e_x(p) = j\omega\mu_0 h_y(p) \quad (3.77b)$$

$$\frac{e_y(p + 1) - e_y(p)}{\Delta x} - \frac{e_x(p + N_x) - e_x(p)}{\Delta y} = j\omega\mu_0 h_z(p) \quad (3.77c)$$

$$\frac{h_z(p) - h_z(p - N_x)}{\Delta y} - j\beta h_y(p) = -j\omega\varepsilon_x(p)e_x(p) \quad (3.77d)$$

$$- \frac{h_z(p) - h_z(p - 1)}{\Delta x} - j\beta h_x(p) = -j\omega\varepsilon_y(p)e_y(p) \quad (3.77e)$$

$$\frac{h_y(p) - h_y(p - 1)}{\Delta x} - \frac{h_x(p) - h_x(p - N_x)}{\Delta y} = -j\omega\varepsilon_z(p)e_z(p) \quad (3.77f)$$

$$j\beta e_z(p) + \frac{e_x(p) - e_x(p - 1)}{\Delta x} + \frac{e_y(p) - e_y(p - N_x)}{\Delta y} = 0 \quad (3.77g)$$

$$j\beta h_z(p) + \frac{h_x(p + 1) - h_x(p)}{\Delta x} + \frac{h_y(p + N_x) - h_y(p)}{\Delta y} = 0 \quad (3.77h)$$

We define the matrices:

$$U_y^{(pq)} = [\mathbf{U}_y]_{pq} = \frac{1}{\Delta y} \begin{cases} 1 & , p + N_x = q \\ -1 & , p = q \end{cases} \quad (3.78a)$$

$$U_x^{(pq)} = [\mathbf{U}_x]_{pq} = \frac{1}{\Delta x} \begin{cases} 1 & , p + 1 = q \\ -1 & , p = q \end{cases} \quad (3.78b)$$

$$V_y^{(pq)} = [\mathbf{V}_y]_{pq} = \frac{1}{\Delta y} \begin{cases} -1 & , p - N_x = q \\ 1 & , p = q \end{cases} \quad (3.78c)$$

$$V_x^{(pq)} = [\mathbf{V}_x]_{pq} = \frac{1}{\Delta x} \begin{cases} -1 & , p - 1 = q \\ 1 & , p = q \end{cases} \quad (3.78d)$$

the vector form of (3.77) becomes:

$$\mathbf{U}_y \mathbf{e}_z - j\beta \mathbf{e}_y = j\omega\mu_0 \mathbf{h}_x \quad (3.79a)$$

$$-\mathbf{U}_x \mathbf{e}_z + j\beta \mathbf{e}_x = j\omega\mu_0 \mathbf{h}_y \quad (3.79b)$$

$$\mathbf{U}_x \mathbf{e}_y - U_y \mathbf{e}_x = j\omega\mu_0 \mathbf{h}_z \quad (3.79c)$$

$$\mathbf{V}_y \mathbf{h}_z - j\beta \mathbf{h}_y = -j\omega\epsilon_0 \epsilon_x \mathbf{e}_x \quad (3.79d)$$

$$-\mathbf{V}_x \mathbf{h}_z + j\beta \mathbf{h}_x = -j\omega\epsilon_0 \epsilon_y \mathbf{e}_y \quad (3.79e)$$

$$\mathbf{V}_x \mathbf{h}_y - V_y \mathbf{h}_x = -j\omega\epsilon_0 \epsilon_z \mathbf{e}_z \quad (3.79f)$$

$$-j\beta \epsilon_z \mathbf{e}_z = \mathbf{V}_x \epsilon_x \mathbf{e}_x + \mathbf{V}_y \epsilon_y \mathbf{e}_y \quad (3.79g)$$

$$-j\beta \mathbf{h}_z = \mathbf{U}_x \mathbf{h}_x + \mathbf{U}_y \mathbf{h}_y \quad (3.79h)$$

The diagonal matrices  $\epsilon_x$ ,  $\epsilon_y$  and  $\epsilon_z$  are given by:

$$[\epsilon_x]_{pp} = \epsilon_r(i + \frac{1}{2}, j) \quad (3.80a)$$

$$[\epsilon_y]_{pp} = \epsilon_r(i, j + \frac{1}{2}) \quad (3.80b)$$

$$[\epsilon_z]_{pp} = \epsilon_r(i, j) \quad (3.80c)$$

We next define the following submatrices:

$$\mathbf{P}_{xx} = \mathbf{V}_y \mathbf{U}_y + \mathbf{U}_x \epsilon_z^{-1} \mathbf{V}_x \epsilon_x + k^2 \epsilon_x \quad (3.81a)$$

$$\mathbf{P}_{xy} = -\mathbf{V}_y \mathbf{U}_x + \mathbf{U}_x \epsilon_z^{-1} \mathbf{V}_y \epsilon_y \quad (3.81b)$$

$$\mathbf{P}_{yx} = -\mathbf{V}_x \mathbf{U}_y + \mathbf{U}_y \epsilon_z^{-1} \mathbf{V}_x \epsilon_x \quad (3.81c)$$

$$\mathbf{P}_{yy} = \mathbf{V}_x \mathbf{U}_x + \mathbf{U}_y \epsilon_z^{-1} \mathbf{V}_y \epsilon_y + k^2 \epsilon_y \quad (3.81d)$$

$$\mathbf{Q}_{xx} = \mathbf{V}_x \mathbf{U}_x + \mathbf{U}_y \epsilon_z^{-1} \mathbf{V}_y \epsilon_y + k^2 \epsilon_y \quad (3.81e)$$

$$\mathbf{Q}_{xy} = \mathbf{V}_x \mathbf{U}_y - \mathbf{U}_y \epsilon_z^{-1} \mathbf{V}_x \epsilon_x \quad (3.81f)$$

$$\mathbf{Q}_{yx} = \mathbf{V}_y \mathbf{U}_x - \mathbf{U}_x \epsilon_z^{-1} \mathbf{V}_y \epsilon_y \quad (3.81g)$$

$$\mathbf{Q}_{yy} = \mathbf{V}_y \mathbf{U}_y + \mathbf{U}_x \epsilon_z^{-1} \mathbf{V}_x \epsilon_x + k^2 \epsilon_x \quad (3.81h)$$

where  $k = 2\pi/\lambda$  is the wavenumber. Finally we end up with two equivalent eigenproblems, one for electric field:

$$\begin{bmatrix} \mathbf{P}_{xx} & \mathbf{P}_{xy} \\ \mathbf{P}_{yx} & \mathbf{P}_{yy} \end{bmatrix} \begin{bmatrix} \mathbf{e}_x \\ \mathbf{e}_y \end{bmatrix} = \beta^2 \begin{bmatrix} \mathbf{e}_x \\ \mathbf{e}_y \end{bmatrix} \quad (3.82)$$

and one for the magnetic field and:

$$\begin{bmatrix} \mathbf{Q}_{xx} & \mathbf{Q}_{xy} \\ \mathbf{Q}_{yx} & \mathbf{Q}_{yy} \end{bmatrix} \begin{bmatrix} \mathbf{h}_x \\ \mathbf{h}_y \end{bmatrix} = \beta^2 \begin{bmatrix} \mathbf{h}_x \\ \mathbf{h}_y \end{bmatrix} \quad (3.83)$$

We can use standard eigenvalue calculations methods to solve either of the eigenproblems and obtain the propagation constant and the modal fields of the propagating modes.

### 3.7.3 Boundary conditions and averaging

At this point it is important to stress out that in order to extract the equations presented above, the electric and magnetic fields at the edges of the grid are considered to be equal to zero, implying that the components of the fields outside the grid are not taken into account. For this reason it is very important that the selection of the grid has to be done in such a manner, so that the field has sufficiently dissipated at the edges of the grid which can increase the grid size considerably. There are more sophisticated solutions in order to enhance field dissipation such as the perfectly matched layers method (PML) presented in [106]. The main idea behind PML is the placement of a fully absorbing layer, which causes almost no reflections, at the edges of the grid.

An analysis of PML is presented in [107]. The introduction of a PML absorber is accomplished by using the following dielectric constant and permeability tensor:

$$\vec{\epsilon} = \begin{bmatrix} \frac{s_y}{s_x} \epsilon & 0 & 0 \\ 0 & \frac{s_x}{s_y} \epsilon & 0 \\ 0 & 0 & s_x s_y \epsilon \end{bmatrix} \quad (3.84a)$$

$$\vec{\mu} = \begin{bmatrix} \frac{s_y}{s_x} \mu & 0 & 0 \\ 0 & \frac{s_x}{s_y} \mu & 0 \\ 0 & 0 & s_x s_y \mu \end{bmatrix} \quad (3.84b)$$

where  $s_x$  and  $s_y$  determine the absorption of the layers according to:

$$s_x = 1 + \frac{\sigma_x}{j\omega\epsilon_0} \quad (3.85a)$$

$$s_y = 1 + \frac{\sigma_y}{j\omega\epsilon_0} \quad (3.85b)$$

and  $\sigma_x$  and  $\sigma_y$  represent the losses coefficients of the PML.

The PML is reflection-less in the limit of very small grid spacing ( $\Delta x, \Delta y \rightarrow 0$ ). In practice, reflections arise and for this reason the coefficients  $\sigma_x$  and  $\sigma_y$  have to be chosen in such a way that they increase gradually rather than abruptly in the edges of the computational grid. It is common to adopt a polynomial variation,

$$\sigma_x = \sigma_{\max} \left( \frac{d_x}{d_{pml}} \right)^n \quad (3.86a)$$

$$\sigma_y = \sigma_{\max} \left( \frac{d_y}{d_{pml}} \right)^n \quad (3.86b)$$

where  $d_x$  and  $d_y$  are the distances from the inner PML boundary at the  $x$  and  $y$  direction respectively and  $d_{pml}$  is the PML thickness. By retracing the steps of the derivation of the eigenproblem in

(3.7.2) and including the tensor quantities we obtain [108]:

$$\mathbf{P}_{xx} = \mathbf{V}_y \mathbf{U}_y \mathbf{M}_y \mathbf{M}_z^{-1} + \mathbf{U}_x \mathbf{E}_z^{-1} \mathbf{V}_x \mathbf{E}_x + k^2 \mathbf{E}_x \mathbf{M}_y \quad (3.87a)$$

$$\mathbf{P}_{xy} = -\mathbf{V}_y \mathbf{U}_x \mathbf{M}_y \mathbf{M}_z^{-1} + \mathbf{U}_x \mathbf{E}_z^{-1} \mathbf{V}_y \mathbf{E}_y \quad (3.87b)$$

$$\mathbf{P}_{yx} = -\mathbf{V}_x \mathbf{U}_y \mathbf{M}_x \mathbf{M}_z^{-1} + \mathbf{U}_y \mathbf{E}_z^{-1} \mathbf{V}_x \mathbf{E}_y \quad (3.87c)$$

$$\mathbf{P}_{yy} = \mathbf{V}_x \mathbf{U}_x \mathbf{M}_x \mathbf{M}_z^{-1} + \mathbf{U}_y \mathbf{E}_z^{-1} \mathbf{V}_y \mathbf{E}_y + k^2 \mathbf{E}_y \mathbf{M}_x \quad (3.87d)$$

$$\mathbf{Q}_{xx} = \mathbf{V}_x \mathbf{U}_x \mathbf{M}_x \mathbf{M}_z^{-1} + \mathbf{U}_y \mathbf{E}_z^{-1} \mathbf{V}_y \mathbf{E}_y + k^2 \mathbf{E}_y \mathbf{M}_x \quad (3.87e)$$

$$\mathbf{Q}_{xy} = \mathbf{V}_x \mathbf{U}_y \mathbf{M}_y \mathbf{M}_z^{-1} - \mathbf{U}_y \mathbf{E}_z^{-1} \mathbf{V}_x \mathbf{E}_y \quad (3.87f)$$

$$\mathbf{Q}_{yx} = \mathbf{V}_y \mathbf{U}_x \mathbf{M}_x \mathbf{M}_z^{-1} - \mathbf{U}_x \mathbf{E}_z^{-1} \mathbf{V}_y \mathbf{E}_x \quad (3.87g)$$

$$\mathbf{Q}_{yy} = \mathbf{V}_y \mathbf{U}_y \mathbf{M}_y \mathbf{M}_z^{-1} + \mathbf{U}_x \mathbf{E}_z^{-1} \mathbf{V}_x \mathbf{E}_x + k^2 \mathbf{E}_x \mathbf{M}_y \quad (3.87h)$$

The auxiliary diagonal matrices  $\mathbf{M}$  and  $\mathbf{E}$  describe the PML absorption effect and their diagonal elements are given by:

$$[\mathbf{E}_x]_{pp} = \varepsilon_r(i + \frac{1}{2}, j) \frac{s_y(j + \frac{1}{2})}{s_x(i)} \quad (3.88a)$$

$$[\mathbf{E}_y]_{pp} = \varepsilon_r(i, j + \frac{1}{2}) \frac{s_x(i)}{s_y(j + \frac{1}{2})} \quad (3.88b)$$

$$[\mathbf{E}_z]_{pp} = \varepsilon_r(i, j) s_x(i) s_y(j) \quad (3.88c)$$

$$[\mathbf{M}_x]_{pp} = \varepsilon_r(i, j + \frac{1}{2}) \frac{s_y(j)}{s_x(i + \frac{1}{2})} \quad (3.88d)$$

$$[\mathbf{M}_y]_{pp} = \varepsilon_r(i + \frac{1}{2}, j) \frac{s_x(i + \frac{1}{2})}{s_y(j)} \quad (3.88e)$$

$$[\mathbf{M}_z]_{pp} = \varepsilon_r(i + \frac{1}{2}, j + \frac{1}{2}) s_x(i + \frac{1}{2}) s_y(j + \frac{1}{2}) \quad (3.88f)$$

If  $\varepsilon_r$  has large discontinuities as in the case of a high-index contrast optical waveguide, the grid must be dense enough to capture the fine details of the structure. An alternative is to smooth the discontinuities by averaging around a grid point. For this reason,  $\varepsilon_r$  is replaced by:

$$\bar{\varepsilon}(x, y) = \frac{1}{\Delta x} \frac{1}{\Delta y} \int_{x-\frac{1}{2}\Delta x}^{x+\frac{1}{2}\Delta x} dx' \int_{y-\frac{1}{2}\Delta y}^{y+\frac{1}{2}\Delta y} dy' \varepsilon(x', y') \quad (3.89)$$

The above formula assumes a rectangular region with dimensions  $\Delta x \times \Delta y$  and  $(x, y)$  as its center. The double integral is used to calculate the average of the dielectric constant within this region.

### 3.7.4 Application of the FDFD method

In order to present a complete picture of the FDFD method, a few examples of the the parameters obtained are shown in figures 3.8, 3.9 and 3.10, which include the number of modes calculated for different waveguide dimensions at different wavelengths, along with the depiction of the components of the transverse electric field for the highest and second highest  $n_{\text{eff}}$  mode. The parameters used for the simulation of the strip waveguide depicted in the figures are summarized in table 3.1.

Parameter	Value	Parameter	Value
$n_1$	1.567	grid step	$\Delta = \Delta_x = \Delta_y = 0.48\mu\text{m}$
$n_2$	1.45	PML profile	polynomial
$n_3$	1	order of PML loss coefficients	$n = 3$
$h_{core}$	$1.5\mu\text{m}$	grid dimensions	$10 \times 10$
$w_{core}$	$1.5\mu\text{m}$	$\sigma_{max}$	$-(n+1)\frac{\log R_0}{2hd_{pml}}$
$h_{cladding}$	$10\mu\text{m}$	$R_0$	$e^{32}$
$w_{cladding}$	$10\mu\text{m}$	$h$	$(\mu_0/\epsilon_0)^{1/2}$
$d_{pml}$	$10 \times \Delta$		

Table 3.1: FDFD parameters

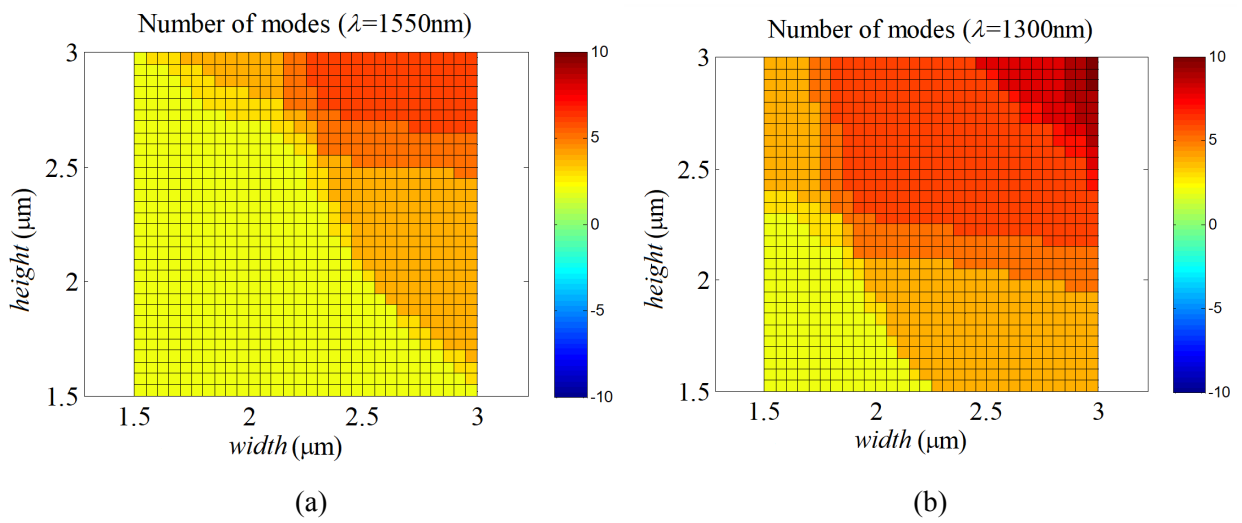


Figure 3.8: FDFD calculation of the number of modes for different values of the width and height of the waveguide for  $\lambda =$  a) 1550 nm and b) 1330 nm

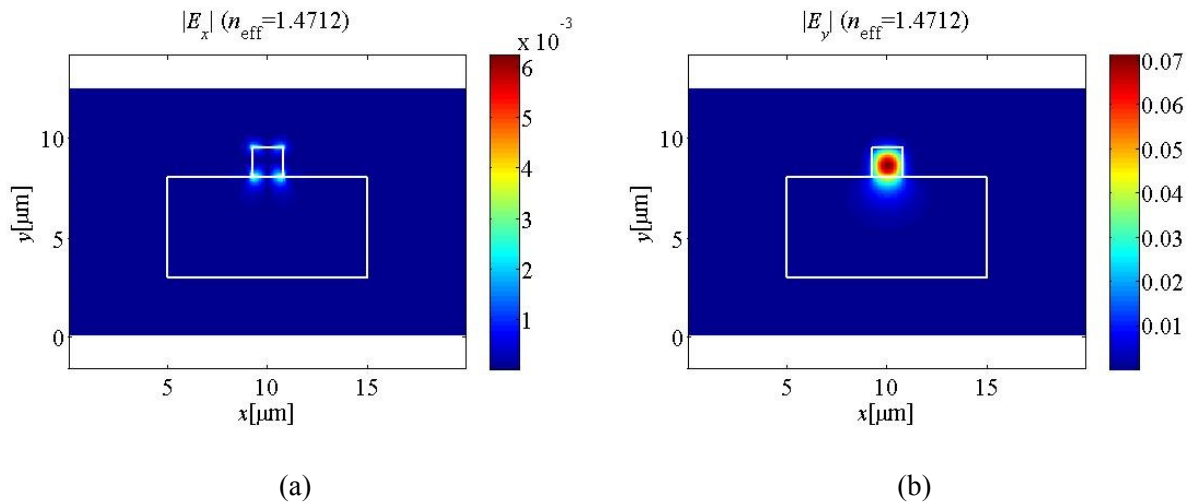


Figure 3.9: FDFD calculation of the a) horizontal and b) vertical component of the transverse electric field of the waveguide for the highest  $n_{eff}$  mode, for  $\lambda = 1500$  nm

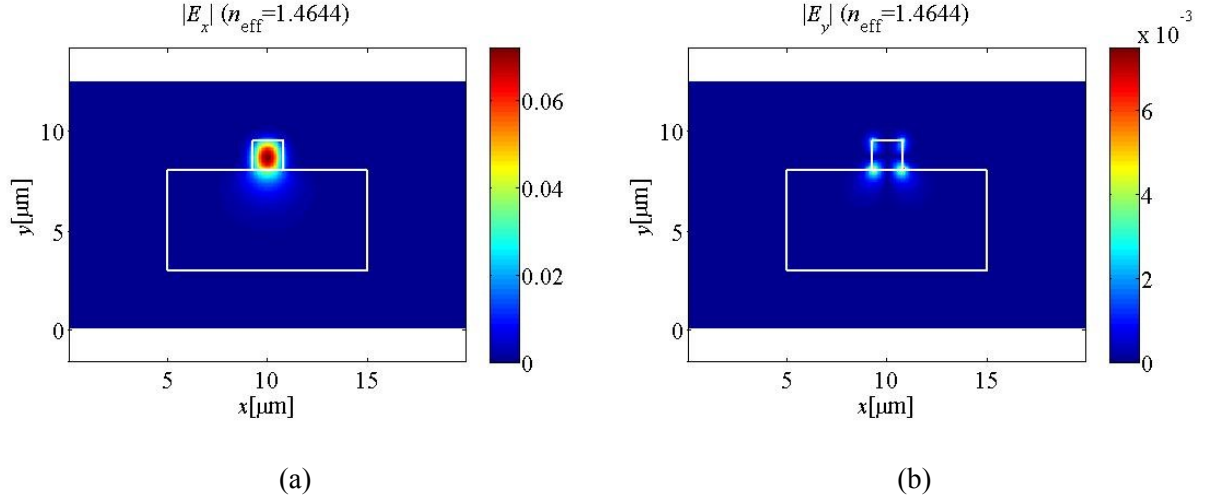


Figure 3.10: FDFD calculation of the a) horizontal and b) vertical component of the transverse electric field of the waveguide for the second highest  $n_{\text{eff}}$  mode, for  $\lambda=1500$  nm

### 3.8 Finite difference time domain method analysis

#### 3.8.1 Yee's grid in 3D

In section 3.7 we used finite difference to approximate Maxwell's equations in the frequency domain and calculate the modal fields. One can also apply a similar approach based on Yee's grid to discretize and solve Maxwell's equations in the time domain. This is known as the finite difference time domain (FDTD) method.

We start from Maxwell's equations in the time domain which can be written in scalar form as follows:

$$\frac{\partial H_x}{\partial t} = \frac{1}{\mu} \left( \frac{\partial E_y}{\partial z} - \frac{\partial E_z}{\partial y} \right) \quad (3.90a)$$

$$\frac{\partial H_y}{\partial t} = \frac{1}{\mu} \left( \frac{\partial E_z}{\partial x} - \frac{\partial E_x}{\partial z} \right) \quad (3.90b)$$

$$\frac{\partial H_z}{\partial t} = \frac{1}{\mu} \left( \frac{\partial E_x}{\partial y} - \frac{\partial E_y}{\partial x} \right) \quad (3.90c)$$

$$\frac{\partial E_x}{\partial t} = \frac{1}{\varepsilon} \left( \frac{\partial H_z}{\partial y} - \frac{\partial H_y}{\partial z} \right) \quad (3.90d)$$

$$\frac{\partial E_y}{\partial t} = \frac{1}{\varepsilon} \left( \frac{\partial H_x}{\partial z} - \frac{\partial H_z}{\partial x} \right) \quad (3.90e)$$

$$\frac{\partial E_z}{\partial t} = \frac{1}{\varepsilon} \left( \frac{\partial H_y}{\partial x} - \frac{\partial H_x}{\partial y} \right) \quad (3.90f)$$

The discretization of equations (3.90) is based on the Yee grid shown in figure 3.11, which is similar to the one used in FDFD, but in this case the grid is three dimensional and not two dimensional as the one presented in section 3.7.

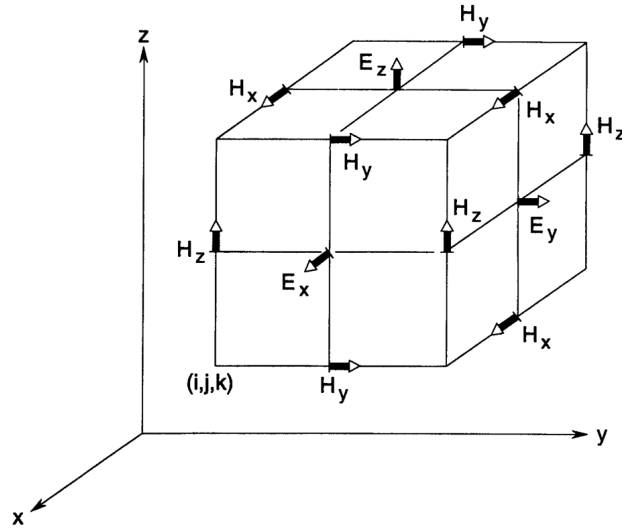


Figure 3.11: The three dimensional Yee's grid

Usually the points of the grid  $(x_i, y_j, z_\kappa)$  on the three dimensional space, where  $1 \leq i \leq N_x$ ,  $1 \leq j \leq N_y$  and  $1 \leq \kappa \leq N_z$  are equidistant.  $N_x$ ,  $N_y$  and  $N_z$  are the number of points on the  $x$ ,  $y$  and  $z$  axes respectively. One therefore obtains,  $x_{i+1} - x_i = \Delta x$ ,  $y_{j+1} - y_j = \Delta y$ ,  $z_{\kappa+1} - z_\kappa = \Delta z$ . The components of the electric and magnetic field are calculated at the following points:

- $E_x$  is calculated at  $\{i\Delta x, (j + 1/2)\Delta y, (\kappa + 1/2)\Delta z\}$
- $E_y$  is calculated at  $\{(i + 1/2)\Delta x, j\Delta y, (\kappa + 1/2)\Delta z\}$
- $E_z$  is calculated at  $\{(i + 1/2)\Delta x, (j + 1/2)\Delta y, \kappa\Delta z\}$
- $H_x$  is calculated at  $\{(i + 1/2)\Delta x, j\Delta y, \kappa\Delta z\}$
- $H_y$  is calculated at  $\{i\Delta x, (j + 1/2)\Delta y, \kappa\Delta z\}$
- $H_z$  is calculated at  $\{i\Delta x, j\Delta y, (\kappa + 1/2)\Delta z\}$

In FDTD, the time variable  $t$  is also discretized so that the magnetic field is calculated at times  $t = n\Delta t$  and the electric field at times  $t = (n + \frac{1}{2})\Delta t$ . Equations (3.90) can be re-written in their finite difference form as:

$$E_x \Big|_{i, j+\frac{1}{2}, \kappa+\frac{1}{2}}^{n+\frac{1}{2}} = E_x \Big|_{i, j+\frac{1}{2}, \kappa+\frac{1}{2}}^{n-\frac{1}{2}} + \frac{\Delta t}{\epsilon_{i, j+\frac{1}{2}, \kappa+\frac{1}{2}}} \left( \frac{H_z \Big|_{i, j+1, \kappa+\frac{1}{2}}^n - H_z \Big|_{i, j, \kappa+\frac{1}{2}}^n}{\Delta} - \frac{H_y \Big|_{i, j+\frac{1}{2}, \kappa+1}^n - H_y \Big|_{i, j+\frac{1}{2}, \kappa}^n}{\Delta} \right) \quad (3.91a)$$

$$E_y \Big|_{i+\frac{1}{2},j,\kappa+\frac{1}{2}}^{n+\frac{1}{2}} = E_y \Big|_{i+\frac{1}{2},j,\kappa+\frac{1}{2}}^{n-\frac{1}{2}} + \frac{\Delta t}{\varepsilon_{i+\frac{1}{2},j,\kappa+\frac{1}{2}}} \left( \frac{H_x \Big|_{i+\frac{1}{2},j,\kappa+1}^n - H_x \Big|_{i+\frac{1}{2},j,\kappa}^n}{\Delta} - \frac{H_z \Big|_{i+1,j,\kappa+\frac{1}{2}}^n - H_z \Big|_{i,j,\kappa+\frac{1}{2}}^n}{\Delta} \right) \quad (3.91b)$$

$$E_z \Big|_{i+\frac{1}{2},j+\frac{1}{2},\kappa}^{n+\frac{1}{2}} = E_y \Big|_{i+\frac{1}{2},j+\frac{1}{2},\kappa}^{n-\frac{1}{2}} + \frac{\Delta t}{\varepsilon_{i+\frac{1}{2},j+\frac{1}{2},\kappa}} \left( \frac{H_y \Big|_{i+1,j+\frac{1}{2},\kappa}^n - H_y \Big|_{i,j+\frac{1}{2},\kappa}^n}{\Delta} - \frac{H_x \Big|_{i+\frac{1}{2},j+1,\kappa}^n - H_x \Big|_{i+\frac{1}{2},j,\kappa}^n}{\Delta} \right) \quad (3.91c)$$

$$H_x \Big|_{i+\frac{1}{2},j,\kappa}^{n+1} = H_x \Big|_{i+\frac{1}{2},j,\kappa}^n + \frac{\Delta t}{\mu} \left( \frac{E_y \Big|_{i+\frac{1}{2},j,\kappa+\frac{1}{2}}^{n+\frac{1}{2}} - E_y \Big|_{i+\frac{1}{2},j,\kappa-\frac{1}{2}}^{n+\frac{1}{2}}}{\Delta} - \frac{E_z \Big|_{i+\frac{1}{2},j+\frac{1}{2},\kappa}^{n+\frac{1}{2}} - E_y \Big|_{i+\frac{1}{2},j-\frac{1}{2},\kappa}^{n+\frac{1}{2}}}{\Delta} \right) \quad (3.92a)$$

$$H_y \Big|_{i,j+\frac{1}{2},\kappa}^{n+1} = H_y \Big|_{i,j+\frac{1}{2},\kappa}^n + \frac{\Delta t}{\mu} \left( \frac{E_z \Big|_{i+\frac{1}{2},j+\frac{1}{2},\kappa}^{n+\frac{1}{2}} - E_z \Big|_{i-\frac{1}{2},j+\frac{1}{2},\kappa}^{n+\frac{1}{2}}}{\Delta} - \frac{E_x \Big|_{i,j+\frac{1}{2},\kappa}^{n+\frac{1}{2}} - E_x \Big|_{i+\frac{1}{2},j-\frac{1}{2},\kappa}^{n+\frac{1}{2}}}{\Delta} \right) \quad (3.92b)$$

$$H_z \Big|_{i,j,\kappa+\frac{1}{2}}^{n+1} = H_z \Big|_{i,j,\kappa+\frac{1}{2}}^n + \frac{\Delta t}{\mu} \left( \frac{E_x \Big|_{i,j+\frac{1}{2},\kappa+\frac{1}{2}}^{n+\frac{1}{2}} - E_x \Big|_{i,j-\frac{1}{2},\kappa+\frac{1}{2}}^{n+\frac{1}{2}}}{\Delta} - \frac{E_y \Big|_{i+\frac{1}{2},j,\kappa+\frac{1}{2}}^{n+\frac{1}{2}} - E_y \Big|_{i-\frac{1}{2},j,\kappa+\frac{1}{2}}^{n+\frac{1}{2}}}{\Delta} \right) \quad (3.92c)$$

Note that according to (3.91) and (3.92) the field calculation can be separated into two steps. The electric field components are updated at times  $t = (n + \frac{1}{2})\Delta t$  using (3.91), based on their values on  $t = (n - \frac{1}{2})\Delta t$  and the values of the magnetic field components at  $t = n\Delta t$ . In a similar manner, the magnetic field components are updated at time  $t = (n + 1)\Delta t$  based on their values at  $t = n\Delta t$  and the values of the electric field at time  $t = (n + \frac{1}{2})\Delta t$  obtained from the previous step. This update procedure is the underlying notion of the FDTD method which unlike FDFD is based on update equations rather than an eigenvalue problem. Starting from suitable initial conditions, we can therefore calculate the time evolution of the electromagnetic field inside the structure.

### 3.8.2 Perfectly matched layers

In section 3.7, we introduced the PML technique in order to avoid the reflections at the edges of the grid. In the 3D case, the tensors used are:

$$\vec{\epsilon} = \begin{bmatrix} \frac{s_y s_z}{s_x} \epsilon & 0 & 0 \\ 0 & \frac{s_x s_z}{s_y} \epsilon & 0 \\ 0 & 0 & \frac{s_x s_y}{s_z} \epsilon \end{bmatrix} \quad (3.93a)$$

$$\vec{\mu} = \begin{bmatrix} \frac{s_y s_z}{s_x} \mu & 0 & 0 \\ 0 & \frac{s_x s_z}{s_y} \mu & 0 \\ 0 & 0 & \frac{s_x s_y}{s_z} \mu \end{bmatrix} \quad (3.93b)$$

where:

$$s_x = 1 + \frac{\sigma_x}{j\omega\epsilon_0} \quad (3.94a)$$

$$s_y = 1 + \frac{\sigma_y}{j\omega\epsilon_0} \quad (3.94b)$$

$$s_z = 1 + \frac{\sigma_z}{j\omega\epsilon_0} \quad (3.94c)$$

where  $\sigma_x$ ,  $\sigma_y$  and  $\sigma_z$  represent the losses coefficients of the PML and are calculated in the same manner as in section 3.7. In order to extract the proper relationships that represent the fields in the time domain, we have to start with Maxwell's equations in the frequency domain and combine them with (3.93) and (3.94), i.e.:

$$\nabla \times \tilde{\mathbf{E}} = -j\omega \vec{\mu} \tilde{\mathbf{H}} \quad (3.95a)$$

$$\nabla \times \tilde{\mathbf{H}} = j\omega \vec{\epsilon} \tilde{\mathbf{E}} \quad (3.95b)$$

Splitting the above equations to their components one obtains:

$$\frac{\partial \tilde{H}_z}{\partial y} - \frac{\partial \tilde{H}_y}{\partial z} = j\omega \varepsilon \frac{s_y s_z}{s_x} \tilde{E}_x \quad (3.96a)$$

$$\frac{\partial \tilde{H}_x}{\partial z} - \frac{\partial \tilde{H}_z}{\partial x} = j\omega \varepsilon \frac{s_z s_x}{s_y} \tilde{E}_y \quad (3.96b)$$

$$\frac{\partial \tilde{H}_y}{\partial x} - \frac{\partial \tilde{H}_x}{\partial y} = j\omega \varepsilon \frac{s_x s_y}{s_z} \tilde{E}_z \quad (3.96c)$$

$$\frac{\partial \tilde{E}_z}{\partial y} - \frac{\partial \tilde{E}_y}{\partial z} = -j\omega \mu \frac{s_y s_z}{s_x} \tilde{H}_x \quad (3.96d)$$

$$\frac{\partial \tilde{E}_x}{\partial z} - \frac{\partial \tilde{E}_z}{\partial x} = -j\omega \mu \frac{s_z s_x}{s_y} \tilde{H}_y \quad (3.96e)$$

$$\frac{\partial \tilde{E}_y}{\partial x} - \frac{\partial \tilde{E}_x}{\partial y} = -j\omega \mu \frac{s_x s_y}{s_z} \tilde{H}_z \quad (3.96f)$$

In order to transform the above equations in first level differential equations in the time domain, the variables  $\tilde{\mathbf{D}}$  and  $\tilde{\mathbf{B}}$  have to be introduced, so that:

$$\tilde{D}_x = \varepsilon \frac{s_z}{s_x} \tilde{E}_x \quad (3.97a)$$

$$\tilde{D}_y = \varepsilon \frac{s_z}{s_y} \tilde{E}_y \quad (3.97b)$$

$$\tilde{D}_z = \varepsilon \frac{s_y}{s_z} \tilde{E}_z \quad (3.97c)$$

$$\tilde{B}_x = \mu \frac{s_z}{s_x} \tilde{H}_x \quad (3.97d)$$

$$\tilde{B}_y = \mu \frac{s_x}{s_y} \tilde{H}_y \quad (3.97e)$$

$$\tilde{B}_z = \mu \frac{s_y}{s_z} \tilde{H}_z \quad (3.97f)$$

Substituting (3.97) into (3.96) we obtain:

$$\frac{\partial \tilde{H}_z}{\partial y} - \frac{\partial \tilde{H}_y}{\partial z} = j\omega s_y \tilde{D}_x = j\omega \tilde{D}_x + \frac{\sigma_y}{\varepsilon_0} \tilde{D}_x \quad (3.98a)$$

$$\frac{\partial \tilde{H}_x}{\partial z} - \frac{\partial \tilde{H}_z}{\partial x} = j\omega s_z \tilde{D}_y = j\omega \tilde{D}_y + \frac{\sigma_z}{\varepsilon_0} \tilde{D}_y \quad (3.98b)$$

$$\frac{\partial \tilde{H}_y}{\partial x} - \frac{\partial \tilde{H}_x}{\partial y} = j\omega s_x \tilde{D}_z = j\omega \tilde{D}_z + \frac{\sigma_x}{\varepsilon_0} \tilde{D}_z \quad (3.98c)$$

$$\frac{\partial \tilde{E}_z}{\partial y} - \frac{\partial \tilde{E}_y}{\partial z} = -j\omega s_y \tilde{B}_x = -j\omega \tilde{B}_x - \frac{\sigma_y}{\varepsilon_0} \tilde{B}_x \quad (3.98d)$$

$$\frac{\partial \tilde{E}_x}{\partial z} - \frac{\partial \tilde{E}_z}{\partial x} = -j\omega s_z \tilde{B}_y = -j\omega \tilde{B}_y - \frac{\sigma_z}{\varepsilon_0} \tilde{B}_y \quad (3.98e)$$

$$\frac{\partial \tilde{E}_y}{\partial x} - \frac{\partial \tilde{E}_x}{\partial y} = -j\omega s_x \tilde{B}_z = -j\omega \tilde{B}_z - \frac{\sigma_x}{\varepsilon_0} \tilde{B}_z \quad (3.98f)$$

which can be re-written in the time domain as:

$$\frac{\partial H_z}{\partial y} - \frac{\partial H_y}{\partial z} = \frac{\partial D_x}{\partial t} + \frac{\sigma_y}{\varepsilon_0} D_x \quad (3.99a)$$

$$\frac{\partial H_x}{\partial z} - \frac{\partial H_z}{\partial x} = \frac{\partial D_y}{\partial t} + \frac{\sigma_z}{\varepsilon_0} D_y \quad (3.99b)$$

$$\frac{\partial H_y}{\partial x} - \frac{\partial H_x}{\partial y} = \frac{\partial D_z}{\partial t} + \frac{\sigma_x}{\varepsilon_0} D_z \quad (3.99c)$$

$$\frac{\partial E_z}{\partial y} - \frac{\partial E_y}{\partial z} = -j\omega \frac{\partial B_x}{\partial t} - \frac{\sigma_y}{\varepsilon_0} B_x \quad (3.99d)$$

$$\frac{\partial E_x}{\partial z} - \frac{\partial E_z}{\partial x} = -j\omega \frac{\partial B_y}{\partial t} - \frac{\sigma_z}{\varepsilon_0} B_y \quad (3.99e)$$

$$\frac{\partial E_y}{\partial x} - \frac{\partial E_x}{\partial y} = -j\omega \frac{\partial B_z}{\partial t} - \frac{\sigma_x}{\varepsilon_0} B_z \quad (3.99f)$$

Replacing the derivatives with their finite differences approximation and assuming for simplicity  $\Delta x = \Delta y = \Delta z$  leads to:

$$D_x \Big|_{i,j+\frac{1}{2},\kappa+\frac{1}{2}}^{n+\frac{1}{2}} = \frac{2\varepsilon_0 - \sigma_y \Delta t}{2\varepsilon_0 + \sigma_y \Delta t} D_x \Big|_{i,j+\frac{1}{2},\kappa+\frac{1}{2}}^{n-\frac{1}{2}} + \frac{2\varepsilon_0 \Delta t}{2\varepsilon_0 + \sigma_y \Delta t} \left( \frac{H_z \Big|_{i,j+1,\kappa+\frac{1}{2}}^n - H_z \Big|_{i,j,\kappa+\frac{1}{2}}^n}{\Delta} - \frac{H_y \Big|_{i,j+\frac{1}{2},\kappa+1}^n - H_y \Big|_{i,j+\frac{1}{2},\kappa}^n}{\Delta} \right) \quad (3.100a)$$

$$D_y \Big|_{i+\frac{1}{2},j,\kappa+\frac{1}{2}}^{n+\frac{1}{2}} = \frac{2\varepsilon_0 - \sigma_z \Delta t}{2\varepsilon_0 + \sigma_z \Delta t} D_y \Big|_{i+\frac{1}{2},j,\kappa+\frac{1}{2}}^{n-\frac{1}{2}} + \frac{2\varepsilon_0 \Delta t}{2\varepsilon_0 + \sigma_z \Delta t} \left( \frac{H_x \Big|_{i+\frac{1}{2},j,\kappa+1}^n - H_x \Big|_{i+\frac{1}{2},j,\kappa}^n}{\Delta} - \frac{H_z \Big|_{i+1,j,\kappa+\frac{1}{2}}^n - H_z \Big|_{i,j,\kappa+\frac{1}{2}}^n}{\Delta} \right) \quad (3.100b)$$

$$D_z \Big|_{i+\frac{1}{2},j+\frac{1}{2},\kappa}^{n+\frac{1}{2}} = \frac{2\varepsilon_0 - \sigma_x \Delta t}{2\varepsilon_0 + \sigma_x \Delta t} D_z \Big|_{i+\frac{1}{2},j+\frac{1}{2},\kappa}^{n-\frac{1}{2}} + \frac{2\varepsilon_0 \Delta t}{2\varepsilon_0 + \sigma_x \Delta t} \left( \frac{H_y \Big|_{i+1,j+\frac{1}{2},\kappa}^n - H_y \Big|_{i,j+\frac{1}{2},\kappa}^n}{\Delta} - \frac{H_x \Big|_{i+\frac{1}{2},j+1,\kappa+\frac{1}{2}}^n - H_x \Big|_{i+\frac{1}{2},j,\kappa+\frac{1}{2}}^n}{\Delta} \right) \quad (3.100c)$$

$$B_x \Big|_{i+\frac{1}{2},j,\kappa}^{n+1} = \frac{2\varepsilon_0 + \sigma_y \Delta t}{2\varepsilon_0 - \sigma_y \Delta t} B_x \Big|_{i+\frac{1}{2},j,\kappa}^n - \frac{2\varepsilon_0 \Delta t}{2\varepsilon_0 - \sigma_y \Delta t} \left( \frac{E_z \Big|_{i+\frac{1}{2},j+\frac{1}{2},\kappa}^{n+\frac{1}{2}} - E_z \Big|_{i+\frac{1}{2},j-\frac{1}{2},\kappa}^{n+\frac{1}{2}}}{\Delta} - \frac{E_y \Big|_{i+\frac{1}{2},j,\kappa+\frac{1}{2}}^{n+\frac{1}{2}} - E_y \Big|_{i+\frac{1}{2},j,\kappa-\frac{1}{2}}^{n+\frac{1}{2}}}{\Delta} \right) \quad (3.101a)$$

$$B_y \Big|_{i,j+\frac{1}{2},\kappa}^{n+1} = \frac{2\varepsilon_0 + \sigma_z \Delta t}{2\varepsilon_0 - \sigma_z \Delta t} B_y \Big|_{i,j+\frac{1}{2},\kappa}^n - \frac{2\varepsilon_0 \Delta t}{2\varepsilon_0 - \sigma_z \Delta t} \left( \frac{E_x \Big|_{i,j+\frac{1}{2},\kappa}^{n+\frac{1}{2}} - E_x \Big|_{i+\frac{1}{2},j-\frac{1}{2},\kappa}^{n+\frac{1}{2}}}{\Delta} - \frac{E_z \Big|_{i+\frac{1}{2},j,\kappa+\frac{1}{2}}^{n+\frac{1}{2}} - E_z \Big|_{i+\frac{1}{2},j,\kappa-\frac{1}{2}}^{n+\frac{1}{2}}}{\Delta} \right) \quad (3.101b)$$

$$B_z \Big|_{i,j,\kappa+\frac{1}{2}}^{n+1} = \frac{2\varepsilon_0 + \sigma_x \Delta t}{2\varepsilon_0 - \sigma_x \Delta t} B_z \Big|_{i,j,\kappa+\frac{1}{2}}^n - \frac{2\varepsilon_0 \Delta t}{2\varepsilon_0 - \sigma_x \Delta t} \left( \frac{E_y \Big|_{i+\frac{1}{2},j,\kappa+\frac{1}{2}}^{n+\frac{1}{2}} - E_y \Big|_{i-\frac{1}{2},j,\kappa+\frac{1}{2}}^{n+\frac{1}{2}}}{\Delta} - \frac{E_x \Big|_{i+\frac{1}{2},j+\frac{1}{2},\kappa}^{n+\frac{1}{2}} - E_x \Big|_{i+\frac{1}{2},j-\frac{1}{2},\kappa}^{n+\frac{1}{2}}}{\Delta} \right) \quad (3.101c)$$

Note that the introduction of the PML alters the update equations since they now involve the components of  $\mathbf{D}$  through (3.100) which are updated based on the components of the magnetic field and also the components of  $\mathbf{B}$  which are updated from the components of the electric field. We therefore need to relate the components of  $\mathbf{D}$  with the components of  $\mathbf{E}$  and the components of  $\mathbf{B}$  with the components of  $\mathbf{H}$ . To do this, we need to write (3.97) in the time domain:

$$\frac{\partial D_x}{\partial t} + \frac{\sigma_x}{\varepsilon_0} D_x = \varepsilon \left( \frac{\partial E_x}{\partial t} + \frac{\sigma_z}{\varepsilon_0} E_x \right) \quad (3.102a)$$

$$\frac{\partial D_y}{\partial t} + \frac{\sigma_y}{\varepsilon_0} D_y = \varepsilon \left( \frac{\partial E_y}{\partial t} + \frac{\sigma_x}{\varepsilon_0} E_y \right) \quad (3.102b)$$

$$\frac{\partial D_z}{\partial t} + \frac{\sigma_z}{\varepsilon_0} D_z = \varepsilon \left( \frac{\partial E_z}{\partial t} + \frac{\sigma_y}{\varepsilon_0} E_z \right) \quad (3.102c)$$

$$\frac{\partial B_x}{\partial t} + \frac{\sigma_x}{\varepsilon_0} B_x = \mu \left( \frac{\partial H_x}{\partial t} + \frac{\sigma_z}{\varepsilon_0} H_x \right) \quad (3.102d)$$

$$\frac{\partial B_y}{\partial t} + \frac{\sigma_y}{\varepsilon_0} B_y = \mu \left( \frac{\partial H_y}{\partial t} + \frac{\sigma_x}{\varepsilon_0} H_y \right) \quad (3.102e)$$

$$\frac{\partial B_z}{\partial t} + \frac{\sigma_z}{\varepsilon_0} B_z = \mu \left( \frac{\partial H_z}{\partial t} + \frac{\sigma_y}{\varepsilon_0} H_z \right) \quad (3.102f)$$

We next need to discretize (3.102) in order to obtain the relations between  $\mathbf{D}$  and  $\mathbf{B}$  with  $\mathbf{E}$  and  $\mathbf{H}$  respectively,

$$E_x \Big|_{i,j+\frac{1}{2},\kappa+\frac{1}{2}}^{n+\frac{1}{2}} = \frac{2\varepsilon_0\Delta t - \sigma_z}{2\varepsilon_0\Delta t + \sigma_z} E_x \Big|_{i,j+\frac{1}{2},\kappa+\frac{1}{2}}^{n-\frac{1}{2}} + \frac{2\varepsilon_0\Delta t + \sigma_x}{\varepsilon(2\varepsilon_0\Delta t + \sigma_z)} D_x \Big|_{i,j+\frac{1}{2},\kappa+\frac{1}{2}}^{n+\frac{1}{2}} - \frac{2\varepsilon_0\Delta t - \sigma_x}{\varepsilon(2\varepsilon_0\Delta t + \sigma_z)} D_x \Big|_{i,j+\frac{1}{2},\kappa+\frac{1}{2}}^{n-\frac{1}{2}} \quad (3.103a)$$

$$E_y \Big|_{i+\frac{1}{2},j,\kappa+\frac{1}{2}}^{n+\frac{1}{2}} = \frac{2\varepsilon_0\Delta t - \sigma_x}{2\varepsilon_0\Delta t + \sigma_x} E_y \Big|_{i+\frac{1}{2},j,\kappa+\frac{1}{2}}^{n-\frac{1}{2}} + \frac{2\varepsilon_0\Delta t + \sigma_y}{\varepsilon(2\varepsilon_0\Delta t + \sigma_x)} D_y \Big|_{i+\frac{1}{2},j,\kappa+\frac{1}{2}}^{n+\frac{1}{2}} - \frac{2\varepsilon_0\Delta t - \sigma_y}{\varepsilon(2\varepsilon_0\Delta t + \sigma_x)} D_y \Big|_{i+\frac{1}{2},j,\kappa+\frac{1}{2}}^{n-\frac{1}{2}} \quad (3.103b)$$

$$E_z \Big|_{i+\frac{1}{2},j+\frac{1}{2},\kappa}^{n+\frac{1}{2}} = \frac{2\varepsilon_0\Delta t - \sigma_y}{2\varepsilon_0\Delta t + \sigma_y} E_z \Big|_{i+\frac{1}{2},j+\frac{1}{2},\kappa}^{n-\frac{1}{2}} + \frac{2\varepsilon_0\Delta t + \sigma_z}{\varepsilon(2\varepsilon_0\Delta t + \sigma_y)} D_z \Big|_{i+\frac{1}{2},j+\frac{1}{2},\kappa}^{n+\frac{1}{2}} - \frac{2\varepsilon_0\Delta t - \sigma_z}{\varepsilon(2\varepsilon_0\Delta t + \sigma_y)} D_z \Big|_{i+\frac{1}{2},j+\frac{1}{2},\kappa}^{n-\frac{1}{2}} \quad (3.103c)$$

$$H_x \Big|_{i+\frac{1}{2},j,\kappa}^{n+1} = \frac{2\varepsilon_0\Delta t - \sigma_z}{2\varepsilon_0\Delta t + \sigma_z} H_x \Big|_{i+\frac{1}{2},j,\kappa}^n + \frac{2\varepsilon_0\Delta t + \sigma_x}{\mu(2\varepsilon_0\Delta t + \sigma_z)} B_x \Big|_{i+\frac{1}{2},j,\kappa}^{n+1} - \frac{2\varepsilon_0\Delta t - \sigma_x}{\mu(2\varepsilon_0\Delta t + \sigma_z)} B_x \Big|_{i+\frac{1}{2},j,\kappa}^n \quad (3.104a)$$

$$H_y \Big|_{i,j+\frac{1}{2},\kappa}^{n+1} = \frac{2\varepsilon_0\Delta t - \sigma_x}{2\varepsilon_0\Delta t + \sigma_x} H_y \Big|_{i,j+\frac{1}{2},\kappa}^n + \frac{2\varepsilon_0\Delta t + \sigma_y}{\mu(2\varepsilon_0\Delta t + \sigma_x)} B_y \Big|_{i,j+\frac{1}{2},\kappa}^{n+1} - \frac{2\varepsilon_0\Delta t - \sigma_y}{\mu(2\varepsilon_0\Delta t + \sigma_x)} B_y \Big|_{i,j+\frac{1}{2},\kappa}^n \quad (3.104b)$$

$$H_z \Big|_{i,j,\kappa+\frac{1}{2}}^{n+1} = \frac{2\varepsilon_0\Delta t - \sigma_y}{2\varepsilon_0\Delta t + \sigma_y} H_z \Big|_{i,j,\kappa+\frac{1}{2}}^n + \frac{2\varepsilon_0\Delta t + \sigma_z}{\mu(2\varepsilon_0\Delta t + \sigma_y)} B_z \Big|_{i,j,\kappa+\frac{1}{2}}^{n+1} - \frac{2\varepsilon_0\Delta t - \sigma_z}{\mu(2\varepsilon_0\Delta t + \sigma_y)} B_z \Big|_{i,j,\kappa+\frac{1}{2}}^n \quad (3.104c)$$

The FDTD algorithm for PML media, is therefore summarized as follows: Starting from suitable initial conditions, we use (3.100) to calculate the components of  $\mathbf{D}$  at time  $t = (n + \frac{1}{2})\Delta t$  from the magnetic field components  $\mathbf{H}$  at time  $t = n\Delta t$ . We next calculate the components of  $\mathbf{E}$  from  $\mathbf{D}$  using (3.103). We next use (3.101) to calculate the components of  $\mathbf{B}$  and then (3.104) to calculate the magnetic field.

### 3.8.3 2D structures

If  $\varepsilon$  is independent of one of the three dimensions, e.g. the  $z$  dimension ( $\varepsilon = \varepsilon(x, y)$ ), the field can be decomposed into two components: one having zero magnetic field component along  $z$

( $H_z = 0$ ), the transverse-magnetic  $\text{TM}_z$  component and one having zero electric field component along  $z$  ( $E_z = 0$ ), the transverse-electric  $\text{TE}_z$  component. The evolution of each wave can be calculated independently using the following Maxwell's equations for the  $\text{TM}_z$  components:

$$\frac{\partial H_x}{\partial t} = \frac{1}{\mu} \left( \frac{\partial E_y}{\partial z} - \frac{\partial E_z}{\partial y} \right) \quad (3.105a)$$

$$\frac{\partial H_y}{\partial t} = \frac{1}{\mu} \left( \frac{\partial E_z}{\partial x} - \frac{\partial E_x}{\partial z} \right) \quad (3.105b)$$

$$\frac{\partial E_z}{\partial t} = \frac{1}{\varepsilon} \left( \frac{\partial H_y}{\partial x} - \frac{\partial H_x}{\partial y} \right) \quad (3.105c)$$

and for the  $\text{TE}_z$  components:

$$\frac{\partial H_z}{\partial t} = \frac{1}{\mu} \left( \frac{\partial E_x}{\partial z} - \frac{\partial E_y}{\partial y} \right) \quad (3.106a)$$

$$\frac{\partial E_x}{\partial t} = \frac{1}{\varepsilon} \left( \frac{\partial H_z}{\partial y} - \frac{\partial H_y}{\partial z} \right) \quad (3.106b)$$

$$\frac{\partial E_y}{\partial t} = \frac{1}{\varepsilon} \left( \frac{\partial H_x}{\partial z} - \frac{\partial H_z}{\partial y} \right) \quad (3.106c)$$

### 3.9 FDTD in MR structures

The popularity of FDTD has grown significantly over the years and several open source and commercial packages have been developed. The MEEP package [109] is an open-source platform incorporating many features including a suitable averaging scheme for  $\varepsilon$  which uses an effective dielectric tensor for non-PML media as well, which is given by:

$$\vec{\varepsilon}_{avg} = \mathbf{P}\langle\varepsilon^{-1}\rangle + (\mathbf{I} - \mathbf{P})\langle\varepsilon\rangle^{-1} \quad (3.107)$$

Matrix  $\mathbf{I}$  is a unitary  $3 \times 3$  matrix and matrix  $\mathbf{P}$  expresses the vertical projection of the surface. Its elements are:

$$P_{ab} = n_a n_b \quad (3.108)$$

where  $1 \leq a, b \leq 3$  and  $\mathbf{n} = [n_1, n_2, n_3]$  is the unitary vector which is vertical to the surface between the two materials. The values inside the  $\langle \rangle$  denote the mean value of the variable calculated inside a cube of dimensions  $\Delta \times \Delta \times \Delta$  whose center is the point where  $\varepsilon$  needs to be calculated.

In figure 3.12 we show the electric field  $E_z$  inside an MR structure, calculated with MEEP assuming a 2D structure. The parameters used for this simulation are presented in table 3.2. At this point it is important to highlight that we used a current-source of central wavelength  $\lambda = 1\mu\text{m}$  which stimulates the  $\text{TM}_z$  waves. One can see the value of the electric field during its first pass through an MR device, for various moments ranging from 100fs to 300fs.

Parameter	Value	Parameter	Value
$n_1$	1.5	$\Delta$	33nm
$n_2$	1 (air)	ring radius	$5.25\mu\text{m}$
waveguide width	$0.5\mu\text{m}$	waveguide-ring distance	$0.2\mu\text{m}$
$d_{pml}$	$1\mu\text{m}$	waveguide-PML distance	$4\mu\text{m}$
source distance from left edge of structure	$2\mu\text{m}$	waveguide length	$40\mu\text{m}$

Table 3.2: MEEP parameters

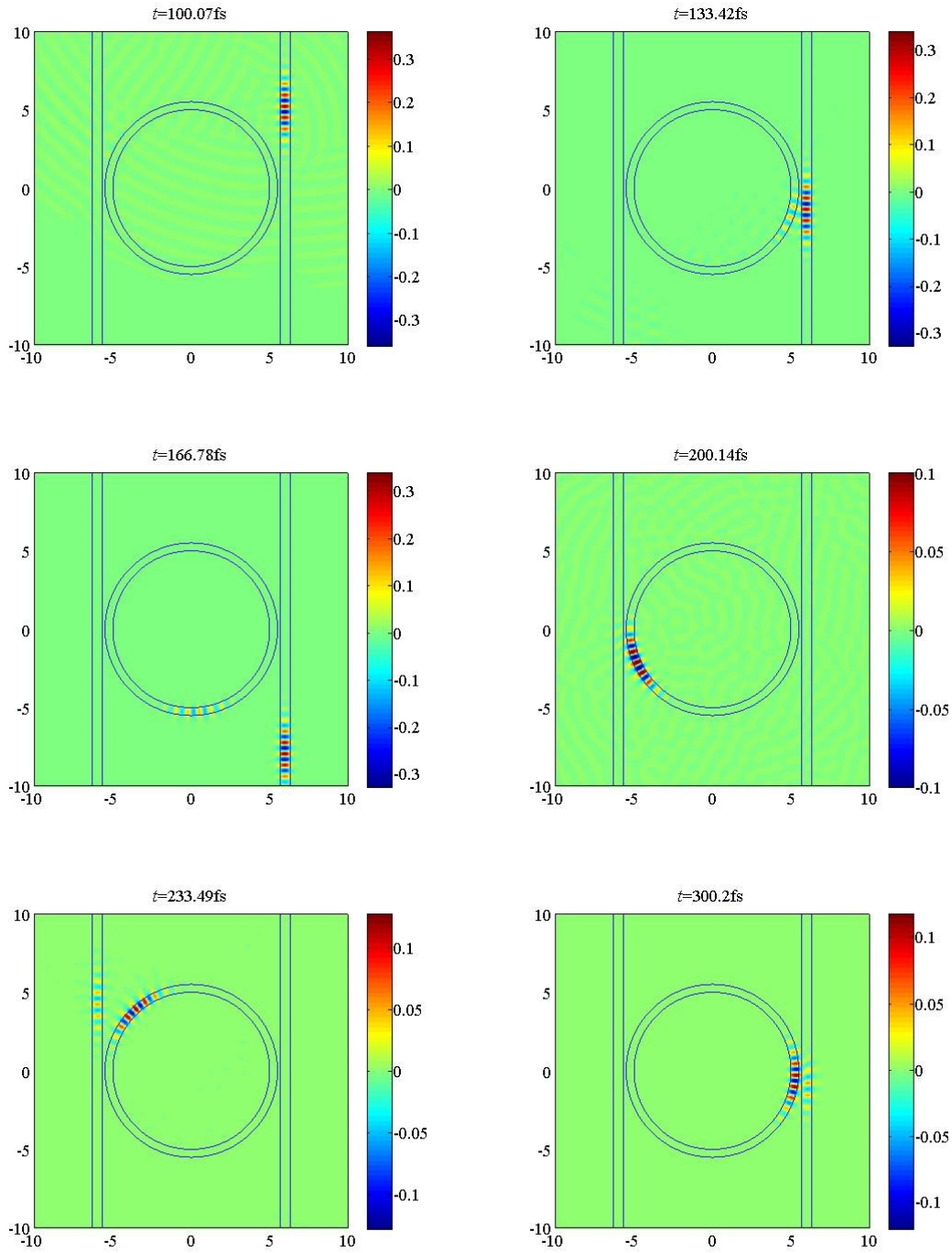


Figure 3.12: Depiction of the value of electric field  $E_z$  during its first pass, inside an MR device using MEEP for different moments varying from 100 fs to 300 fs

Although the results seem to indicate that FDTD can be applied in MR structures, we have found that the method can not be used accurately for large scale design optimization where the fields need to be calculated for different sets of design parameters. This is true even for the 2D case of (3.12) where we ignore field confinement in the vertical direction. Even in this simplified scenario, the time required on a standard desktop computer, for the simulation to complete is of the order of 1h which is prohibitive even for a single simulation especially, if denser grid is used. It was therefore realized early on our work that using FDTD combined with the optimization schemes outlined in the next section was highly impractical. This is why, the CMT framework is used throughout this thesis as a basis for the calculation of the transfer function. It is interesting to note that evidence in the literature [110] suggests that FDTD and coupled mode analysis agree very well for the coupling region of the ring even if a full-blown 3D model is assumed.

## 4 Designing MR structures

In this chapter, we outline the procedure proposed to design multiple MR structures and calculate the optimum values for structural parameters such as the coupling coefficients and the ring radii. Our approach can be applied independently of the number of the rings ( $N$ ) that might be used in a multi MR device.

The work presented in this chapter is not a simulation method. As emphasized in section 1.1 we address the design/optimization problem in figure 1.1b rather than the simulation/analysis problem in figure 1.1a. In section 3.1 we have already described that the design problem can be reduced to the minimization of a suitable metric  $d$  that measures the difference between the device  $T(f)$  and the (nearly) rectangular function  $T_0(f)$  in (3.1). The location of the minimum  $\mathbf{p} = \mathbf{p}_{\text{opt}}$  in the multi-dimensional space will yield optimum design parameter values. To our knowledge, this is the first time optimization methods have been applied in the design of multiple micro-ring structures. We search inside a multi-parameter space defined by the ring radii and coupling coefficients, the range of which are predefined so as to ensure that the optimum values can be realized in practice. Before resorting to optimization methods one could first try an exhaustive search method as explained in section 3.1, where the multi-dimensional parameter space is sampled and the  $T(f)$  is calculated for every point on the grid in order to determine the closest match to the ideal  $T(f)$ . However, as the number of rings increases, the size of the multi-dimensional search grid grows exponentially, which renders this approach inefficient.

The choice of the method by which the  $T(f)$  is calculated has also an important bearing on the feasibility of the endeavor. In the present analysis, we have used as a basis the coupled-mode theoretic approach of sections 3.2-3.6 which is both intuitively appealing and efficient in terms of computational time and memory requirements. This is unlike full-blown electromagnetic simulation tools such as the FDTD and the FDFD methods of sections 3.7 and 3.8 respectively. As explained in 3.9, in both cases the computational resources required can be huge even if a 2D approximation is carried out by means of the effective index method. FDTD may require a large amount of time for the simulations to conclude due to the fact that the ring resonances are usually spectrally narrow, implying a slow power exchange between the waveguides and the rings. Hence, once the device is excited by the incident pulse, the simulation may require many round-trips for the electromagnetic field to fully dissipate at the output waveguide. In FDFD, one usually runs into excessive memory requirements in order to store the system matrix corresponding to the structure at hand. Coupled mode theory is much faster and equally accurate when compared with full-blown simulation tools. Coupled mode theory also forms the basis for the TMM, which is frequently adopted in multi-ring structures. In the present analysis, we start from the coupled mode framework that can be used in order to reduce the problem of calculating the  $T(f)$  into the solution of a  $(4N + 2) \times (4N + 2)$  system of unknowns which correspond to the modal amplitudes of the electromagnetic field inside the structure. We discuss in detail how the matrix of the system can be systematically constructed for an arbitrary number of micro-rings and how its elements are related to the geometric and coupling parameters. Using this scheme and optimization methods we

are thus able to obtain transfer functions with reasonably flat pass-band which are aperiodic and hence are not severely restricted by the FSR of the individual resonators. The results of this work were published in [111].

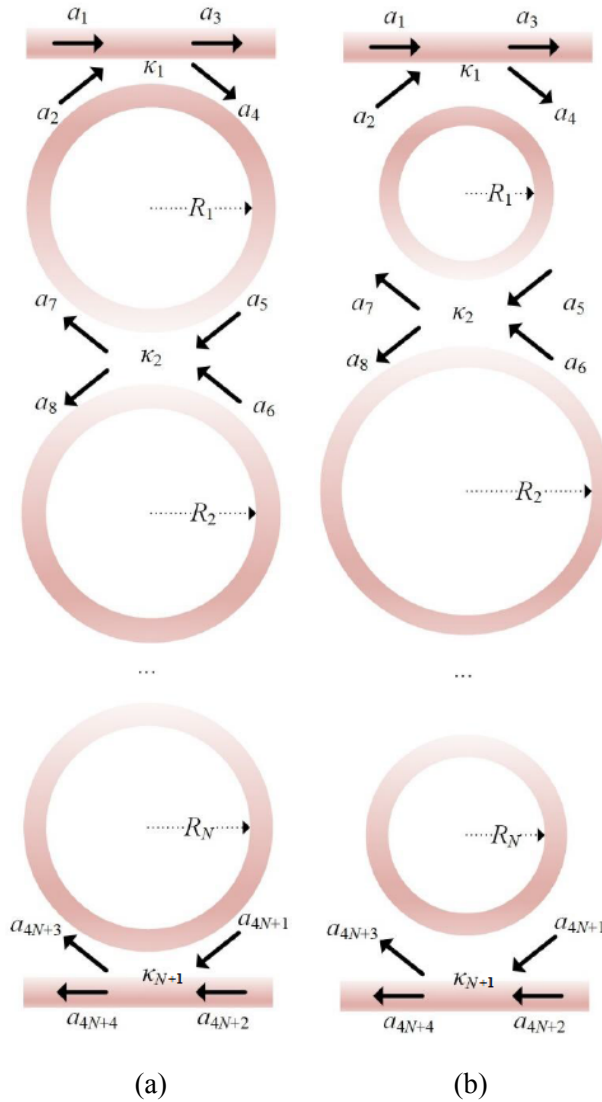


Figure 4.1: Schematic of a) a uniform multiring structure and b) a non uniform multiring structure

The spacing between the waveguides and the adjacent rings as well as between consecutive rings, as shown in figure 4.1, determines the coupling coefficients  $\kappa_i$  of the various coupling regions [12], [112]. There are a total of  $N + 1$  coupling regions in the structure and  $\kappa_1$  refers to the coupling coefficient between the input waveguide and the first ring,  $\kappa_i$  for  $2 \leq i \leq N$  stand for the coupling coefficient between the  $(i - 1)^{th}$  and the  $i^{th}$  rings while  $\kappa_{N+1}$  is the coupling coefficient between the last ring and the output waveguide. We also assume that the rings have radii  $R_i$  for  $1 \leq i \leq N$ . For structures such as the ones depicted in figure 4.1, coupled mode theory provides an intuitive way of describing the electromagnetic field interaction at the various components of the structure. Each ring supports two degenerate guided modes, one propagating clockwise and the other counterclockwise along the ring. At the first coupling region, light at the input waveguide is coupled to the clockwise mode of the first ring near the resonant frequency of the resonator. The

coupling of light in the counter-clockwise mode is negligible due to poor phase-matching conditions. At the second coupling region between the first and the second ring, light enters from the opposite direction and is therefore coupled to the counter-clockwise guided mode of the second ring. This interaction continues as light is coupled from resonator to resonator until it is coupled to the output waveguide. Depending on whether the number of rings  $N$  is even or odd, light may exit the output waveguide in either the same or opposite direction respectively with regards to the light incident at the input waveguide.

## 4.1 CMT framework

Using the reciprocity relations in section 3.2, it is possible to rigorously relate the amplitudes of the modes at the input and the output of each interaction region through the coupling coefficients [72]. The coupling coefficients  $\kappa_i$  are determined by the electric field profiles of the modes of the isolated waveguides and can be calculated approximately analytically assuming an effective index 2D approximation [12] or numerically using rigorous mode analysis and numerical integration of the modal field overlap near the coupling region [112]. Since the number of coupling regions is  $N + 1$ , there are  $4(N + 1)$  modal amplitudes describing the transfer of the electromagnetic field across the structure. We choose to label the amplitudes so that in the  $i^{th}$  coupling region  $a_{4i-3}$  and  $a_{4i-2}$  are the amplitudes of the modes at the input of the region while  $a_{4i-1}$  and  $a_{4i}$  are the amplitudes at the output. According to the analysis in section 3.6, these amplitudes are related through the following equations:

$$a_{4i-1} = \sqrt{1 - \kappa_i} a_{4i-3} - j\sqrt{\kappa_i} a_{4i-2} \quad (4.1a)$$

$$a_{4i} = -j\sqrt{\kappa_i} a_{4i-3} + \sqrt{1 - \kappa_i} a_{4i-2} \quad (4.1b)$$

The above equations hold for  $1 \leq i \leq N + 1$ . As a result of the field propagation inside the rings, the amplitudes undergo a phase shift. Taking into account the arrangement of figure 4.1 we see that:

$$a_{4i+1} = a_{4i} e^{-j\phi_i} \quad (4.2a)$$

$$a_{4i-2} = a_{4i+3} e^{-j\phi_i} \quad (4.2b)$$

where  $\phi_i$  is the phase shift resulting from the half round-trip propagation in the left or right half of the  $i^{th}$  ring resonator determined by:

$$\phi_i = \left( \frac{2\pi n_{\text{eff}}}{\lambda} - ja \right) \pi R_i \quad (4.3)$$

In (4.3)  $\lambda$  is the wavelength,  $n_{\text{eff}}$  is the effective refractive index of the waveguide mode in the ring and  $a$  is the propagation loss written in units of neper per unit length, which is initially considered as zero. Equation (4.2a) describes the propagation of the wave exiting the  $i^{th}$  coupling region in the  $i^{th}$  ring up to the point that it enters the  $(i + 1)^{th}$  region. Equation (4.2b) describes the propagation of the wave exiting the latter region up to the point that it re-enters the  $i^{th}$  region. Since there are  $N$  rings, (4.2) hold for  $1 \leq i \leq N$ . Given the ranges of index  $i$  in (4.1) and (4.2) we deduce that

the amplitudes  $a_m$  (which are  $4N + 4$  in number) are determined by a system of  $4N + 2$  equations. We should also bear in mind that according to figure 4.1,  $a_1$  is the amplitude of the incident field in the input waveguide that can be assumed equal to unity,  $a_1 = 1$  while  $a_{4N+2}$  is the field entering the output waveguide which should be zero since this waveguide is not excited at its input, hence  $a_{4N+2} = 0$ . The remaining unknown amplitudes can in principle be determined by the system of (4.1)-(4.2).

Given a waveguide structure, the effective index  $n_{\text{eff}}$  can be calculated using either approximate analytical expressions [113] or numerical mode solvers [108]. If the waveguide design is different for each ring, we can allow for different effective refractive indices  $n_{\text{eff}}^{(i)}$  in (4.3). However adopting different waveguide designs might unnecessarily complicate the fabrication process. It therefore makes more sense to assume that the waveguide parameters (dimensions and material indices) do not vary across the rings of the structures. Another point to consider is that the waveguides can be generally lossy, as a result of the either curvature-induced radiation losses or scattering loss due to fabrication imperfections. The losses can be incorporated in the imaginary part of the effective index  $n_i = \text{Im}\{n_{\text{eff}}\}$  [92]. In this work, we carry out our designs assuming negligible loss but should the need arises for inclusion of loss, this is easily accomplished by properly adjusting  $n_i$ .

Equations (4.1)-(4.2) form the basis for estimating the  $T(f)$  of the device defined as the ratio of  $a_{4N+4}$  to  $a_1$  corresponding to the amplitude of the waveguide mode exiting the output waveguide and at the input waveguide respectively:

$$T(f) = \left| \frac{a_{4N+4}}{a_1} \right|^2 \quad (4.4)$$

To calculate  $a_{4N+4}$  it is useful to write (4.1)-(4.2) in matrix notation. We define:

$$t_i = -\sqrt{1 - \kappa_i} \quad (4.5a)$$

$$x_i = j\sqrt{\kappa_i} \quad (4.5b)$$

and taking into account that  $a_1 = 1$ , the equations for the first coupling region ( $i = 1$ ) are written as:

$$a_2 - a_7 e^{-j\phi_1} = 0 \quad (4.6a)$$

$$a_3 + x_1 a_2 = -t_1 \quad (4.6b)$$

$$a_4 + t_1 a_2 = -x_1 \quad (4.6c)$$

$$a_5 - a_4 e^{-j\phi_1} = 0 \quad (4.6d)$$

For intermediate coupling regions ( $2 \leq i \leq N$ , assuming that  $N \geq 2$ ), we re-write the coupling equations as:

$$a_{4i-2} - a_{4i+3} e^{-j\phi_{i-1}} = 0 \quad (4.7a)$$

$$a_{4i-1} + x_i a_{4i-2} + t_i a_{4i-3} = 0 \quad (4.7b)$$

$$a_{4i} + t_i a_{4i-2} + x_i a_{4i-3} = 0 \quad (4.7c)$$

$$a_{4i+1} - a_{4i} e^{-j\phi_{i-1}} = 0 \quad (4.7d)$$

At the last coupling region ( $i = N + 1$ ) we have  $a_{4N+2} = 0$  and hence the following equations:

$$a_{4N+3} - t_{N+1}a_{4N+1} = 0 \quad (4.8a)$$

$$a_{4N+4} - x_{N+1}a_{4N+1} = 0 \quad (4.8b)$$

In matrix notation, we may define the coupling region sub-matrices  $\mathbf{M}_i$ :

$$\mathbf{M}_1 = \begin{bmatrix} 1 & 0 & 0 & 0 & 0 & -e^{-j\phi_1} \\ x_1 & 1 & 0 & 0 & 0 & 0 \\ t_1 & 0 & 1 & 0 & 0 & 0 \\ 0 & 0 & -e^{-j\phi_1} & 1 & 0 & 0 \end{bmatrix} \quad (4.9a)$$

$$\mathbf{M}_i = \begin{bmatrix} 0 & 1 & 0 & 0 & 0 & 0 & -e^{-j\phi_i} \\ t_i & x_i & 1 & 0 & 0 & 0 & 0 \\ x_i & t_i & 0 & 1 & 0 & 0 & 0 \\ 0 & 0 & 0 & -e^{-j\phi_i} & 1 & 0 & 0 \end{bmatrix}, (2 \leq i \leq N) \quad (4.9b)$$

$$\mathbf{M}_{N+1} = \begin{bmatrix} t_{N+1} & x_{N+1} & 1 & 0 \\ x_{N+1} & t_{N+1} & 0 & 1 \end{bmatrix} \quad (4.9c)$$

and the  $(4N+2) \times (4N+2)$  sparse system matrix  $\mathbf{M} = [M_{pq}]$  which is formed from the sub-matrices as follows:

$$\mathbf{M} = \begin{bmatrix} \mathbf{M}_1 & \mathbf{0}_{4 \times 4} & \cdots & \mathbf{0}_{4 \times 2} \\ \mathbf{M}_{4 \times 3} & \mathbf{M}_2 & \cdots & \mathbf{0}_{4 \times 2} \\ \vdots & \vdots & \ddots & \vdots \\ \mathbf{0}_{4 \times 3} & \mathbf{0}_{4 \times 4} & \cdots & \mathbf{M}_{N+1} \end{bmatrix} \quad (4.10)$$

where the matrix  $\mathbf{0}_{\mu \times \nu}$  stands for a  $\mu \times \nu$  matrix with zero elements. The sub-matrices  $\mathbf{M}_i$  for  $1 \leq i \leq N + 1$  are arranged so that the elements  $M_{pp}$  of the diagonal of  $\mathbf{M}$  are always equal to unity. We also define the vectors:

$$\mathbf{a} = (a_2, \cdots, a_{4N+1}, a_{4N+3}, a_{4N+4})^T \quad (4.11a)$$

$$\mathbf{c} = (0, -t_1, -x_1, 0, \cdots, 0)^T \quad (4.11b)$$

where  $()^T$  stands for transpose of the vector. Based on these definitions, it is easy to see that the system of (4.6)-(4.8) is written in matrix notation as:

$$\mathbf{M}\mathbf{a} = \mathbf{c} \quad (4.12)$$

The system in (4.12) can be easily solved for  $\mathbf{a}$  with standard numerical analysis algorithms [79]. Once  $\mathbf{a}$  is determined we readily calculate the transfer function through (4.4). This provides a general, and easily scalable framework for estimating the transfer function of the structure given its parameters, valid for an arbitrary number of rings  $N$ . Figure 4.2a shows the function obtained for a single ring structure  $N = 1$  assuming that  $n_{\text{eff}} \approx 3.3$  which is typical for silicon waveguides,  $R_1 = 14.7 \mu\text{m}$  and  $\kappa_1 = \kappa_2 = 0.3$ . The transfer function is plotted in terms of  $\delta f = f - f_0$  where  $f_0 = 196 \text{ THz}$  corresponding to a free space wavelength of  $\lambda_0 = 1.531 \mu\text{m}$ . We obtain the well-known Lorentzian-like response of the single micro-ring resonator filter. We also plot the

transfer function in a wider frequency range  $\pm 2$  THz around  $f_0$  in figure 4.2b, where we observe the periodic response because of the multiplicity of the resonant frequencies of the single micro-ring occurring when the phase difference from one full roundtrip in the ring is equal to multiples of  $2\pi$ , i.e.  $2\phi_1 = 2m\pi$  where  $m$  is an integer.

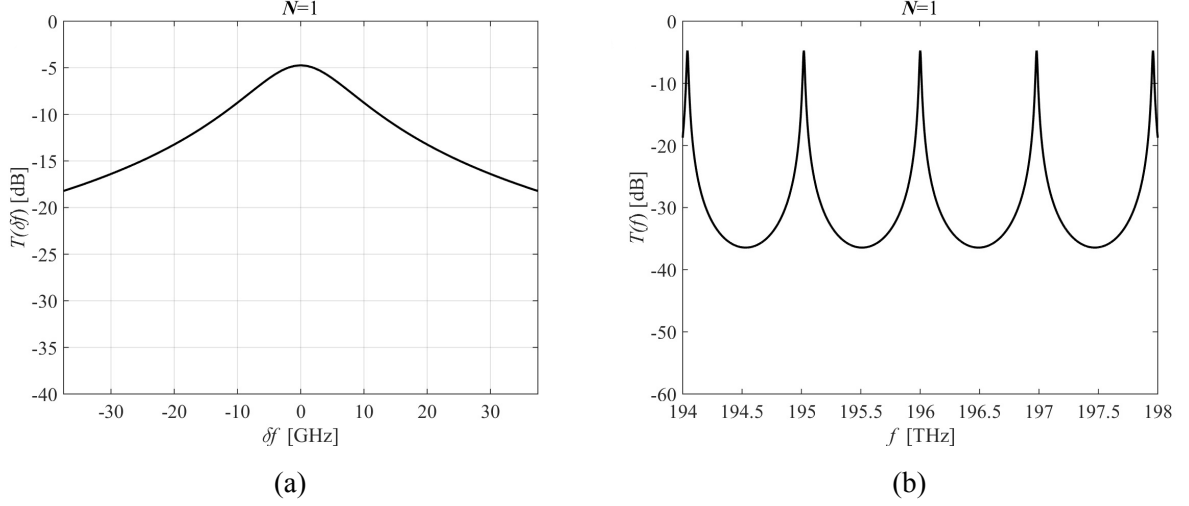


Figure 4.2: Transfer function of single micro-ring structure

As shown above, the transfer function obtained through the matrix  $\mathbf{M}$  and the vector  $\mathbf{c}$  depends on the coupling coefficients  $\kappa_i$  and the phases  $\phi_i$  which are dependent on the ring radii  $R_i$  through (4.3). We may therefore formally write:

$$T(f) = F(f, \kappa_1, \dots, \kappa_{N+1}, R_1, \dots, R_N) \quad (4.13)$$

## 4.2 Minimization metric

In order to choose the design parameters  $\kappa_i$  and  $R_i$  we can minimize a suitable metric  $d$  between  $T(f)$  and an almost rectangular transfer function weighted by some appropriate function  $w(f)$ , as explained in section 3.1. We choose the following minimization metric:

$$d = \int_{-\infty}^{+\infty} |T(f) - 1| w(f) \delta f + \int_{-\infty}^{+\infty} T(f) |1 - w(f)| \delta f \quad (4.14)$$

The weighting function  $w(f)$  can be any sufficiently box-like function which ensures that  $T(f)$  is matched to unity inside a specified frequency range  $f \in I_F$ . Outside this region we desire the smallest possible crosstalk and hence  $T(f)$  should be matched to zero for  $f \notin I_F$ . The first integral of the minimization metric in (4.14) calculates the distance between the transfer function and unity for frequencies mainly inside  $I_F$  while the second integral takes care of the frequency region away from the central frequency. In our calculations we have chosen  $w(f)$  to be a super-Gaussian function of order 6, i.e.:

$$w(f) = \exp\left(-\frac{(f - f_0)^6}{B^6}\right) \quad (4.15)$$

where  $f_0$  is the desired central frequency of our filter and  $2B$  is the desired pass-band range. We assume  $B = 15$  GHz for the remainder of the analysis. If  $d$  is minimized we therefore expect a flat pass-band near  $f = f_0$  and small cross-talk far from  $f_0$ . In practice we sampled the frequency axis on 200 points inside  $[f_{\min}, f_{\max}]$  where  $f_{\min} = f_0 - 1.5B$  and  $f_{\max} = f_0 + 1.5B$  and used the trapezium rule to evaluate the minimization metric  $d$  in (4.14). In most cases, we found that the obtained transfer function had low cross-talk over a much wider frequency region than  $[f_{\min}, f_{\max}]$  as we shall see below.

In our minimizations, it is useful to exclude values inside the multi-dimensional parameter space for which we do not expect favorable behavior for  $T(f)$ . Much insight can be gained from considering the system of coupled resonators as one large resonator in order to facilitate the search. The resonant frequencies of the large resonator are obtained from the resonant frequencies of the individual resonators which are detuned because of the resonator-to-resonator coupling [114]. In order to obtain a flatter frequency response we should ensure that the resonances occur at frequencies near  $f_0$ . Possibly the simplest way to do this is to have all micro-rings resonate at  $f_0$ , i.e.:

$$\frac{2\pi n_{\text{eff}}}{\lambda_0}(2\pi R_i) = 2\pi\mu_i \quad (4.16)$$

where  $\mu_i$  are integers determining the order of the resonance and  $\lambda_0 = c/f_0$ . The above condition implies that the central frequency  $f_0$  belongs to the resonant frequencies of the individual rings and hence a flatter response is expected near its vicinity. To impose this condition in the minimization process we simply evaluate the integer  $\nu_i$  which is closest to  $2\pi n_{\text{eff}}/\lambda_0 R_i$  and set:

$$\bar{R}_i = \frac{\nu_i \lambda_0}{2\pi n_{\text{eff}}} \quad (4.17)$$

and then use  $\bar{R}_i$  instead of  $R_i$  when evaluating the transfer function in (4.13).

In our designs we have assumed that  $f_0 = 196$  THz and  $n_{\text{eff}} = 3.3$  just as in figure 4.2. We assume that the ring radii  $R_i$  range from 14  $\mu\text{m}$  to 24  $\mu\text{m}$  while the coupling coefficients  $\kappa_i$  vary from 0 to 0.3 [115], [116]. It should be noted that the range of values of radii and coupling coefficients in general is bounded by the limits of state-of-the-art fabrication processes on the one hand and the application requirements on the other. The chosen range for  $R_i$  and  $\kappa_i$  lies within the capabilities of large scale fabrication techniques and as it will be shown below complies with the operational requirements. In this work, we used an interior-point approach that combines a direct method for solving the constrained minimization problem along with conjugate gradient steps using trust regions [101]. The initial guess (starting point) is of particular importance in order to ensure a favorable convergence. The metric  $d$  in (4.14) generally possesses many local minima in the multi-parameter space and we would benefit from starting our minimization close to one suitable minimum. On the other hand we need to avoid minima corresponding to rings with similar radii because the nearly periodic nature of the transfer function in this case would imply increased cross-talk away from  $f = f_0$  just as in figure 4.2b. We therefore choose the initial guess for the ring radii with a uniform random distribution. The coupling coefficients on the other hand can initially be chosen to favor a flat design. Again referring to the resonant frequencies of the larger resonator consisting of the  $N$  individual resonators, we see that the inner ring-to-ring coupling coefficients

$(\kappa_i, 2 \leq i \leq N)$  should be small, in order to allow for a small detuning of the resonant frequencies. The outer coupling coefficients ( $\kappa_1$  and  $\kappa_{N+1}$ ) should be large in order to ensure a broad resonance. We therefore choose to set  $\kappa_1 = \kappa_{N+1} = 0.3$  and  $\kappa_2 = \dots = \kappa_N = 0.1$  as a starting point in our minimizations.

### 4.3 Results and discussion

In this part of the dissertation we demonstrate the results obtained from the minimization of the metric in (4.14). We considered the cases where  $N=2,3,4,5$  and 6 since a higher number of rings may render the implementation of the design impractical. Figures 4.3 and 4.4 provide bar plots of the coupling coefficients and the ring radii of the optimized designs respectively. Figures 4.5 and 4.6 show the corresponding transfer functions near the pass-band and a larger frequency range respectively. All minimizations took less than 4min on a standard desktop personal computer with 8 GB of RAM and an eight-core AMD FX3120, 3.3 GHz processor. The iterations required in the minimization algorithm were always less than 300.

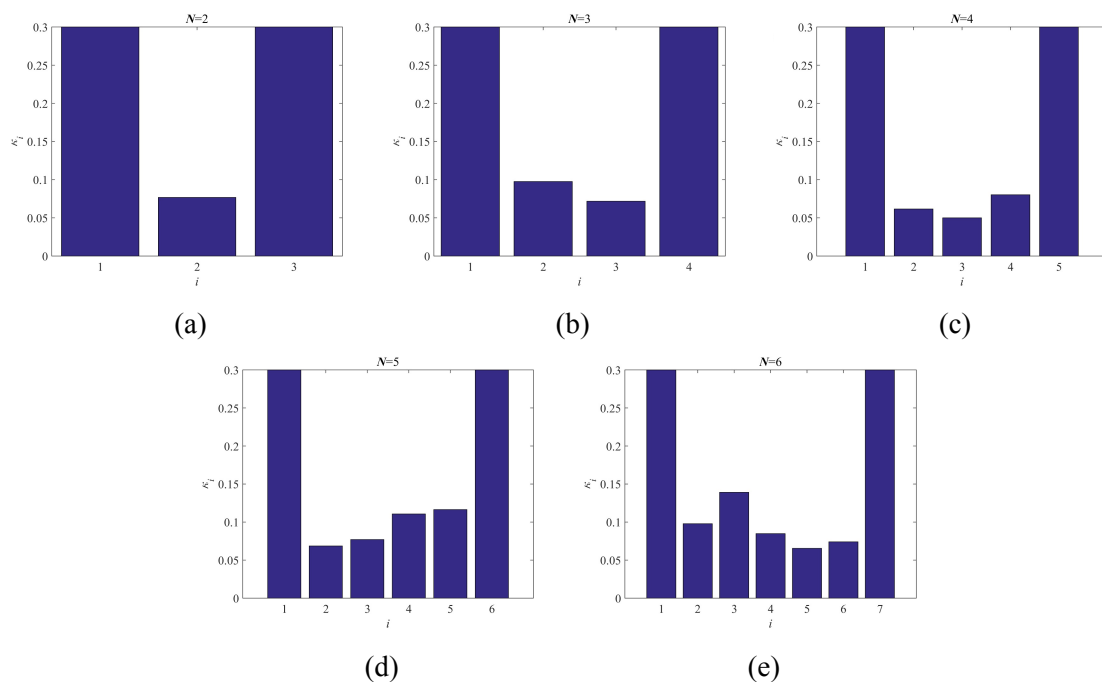


Figure 4.3: Coupling coefficients  $\kappa_i$  obtained for a)  $N = 2$ , b)  $N = 3$ , c)  $N = 4$ , d)  $N = 5$  and e)  $N = 6$  rings

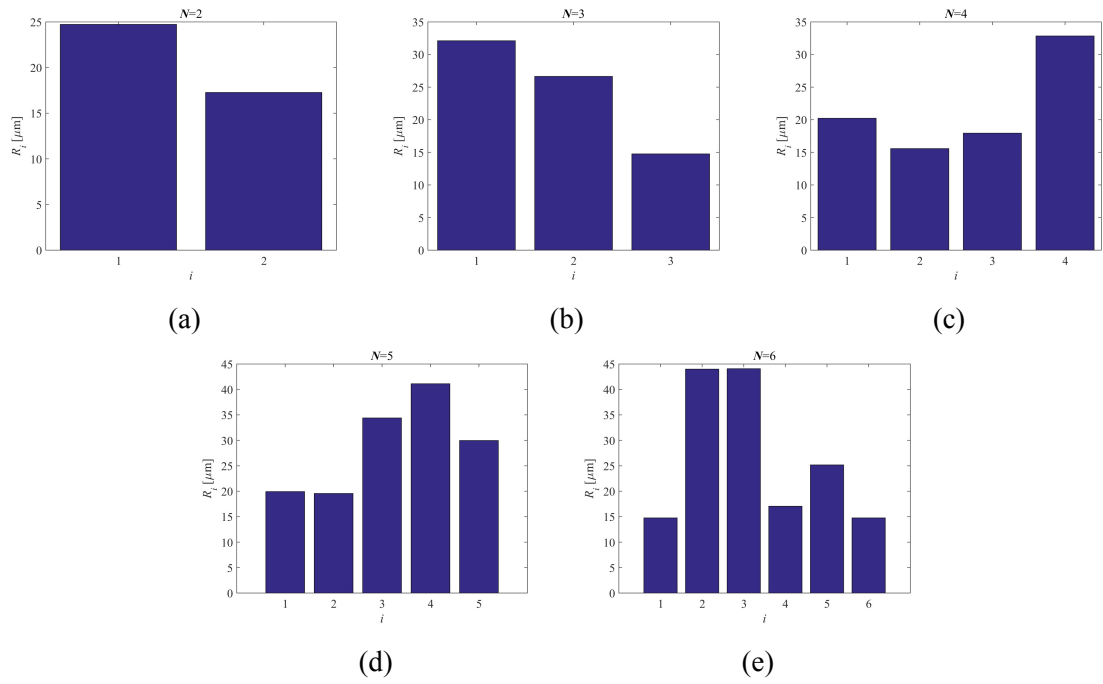


Figure 4.4: Ring radii  $R_i$  obtained for a)  $N = 2$ , b)  $N = 3$ , c)  $N = 4$ , d)  $N = 5$  and e)  $N = 6$  rings

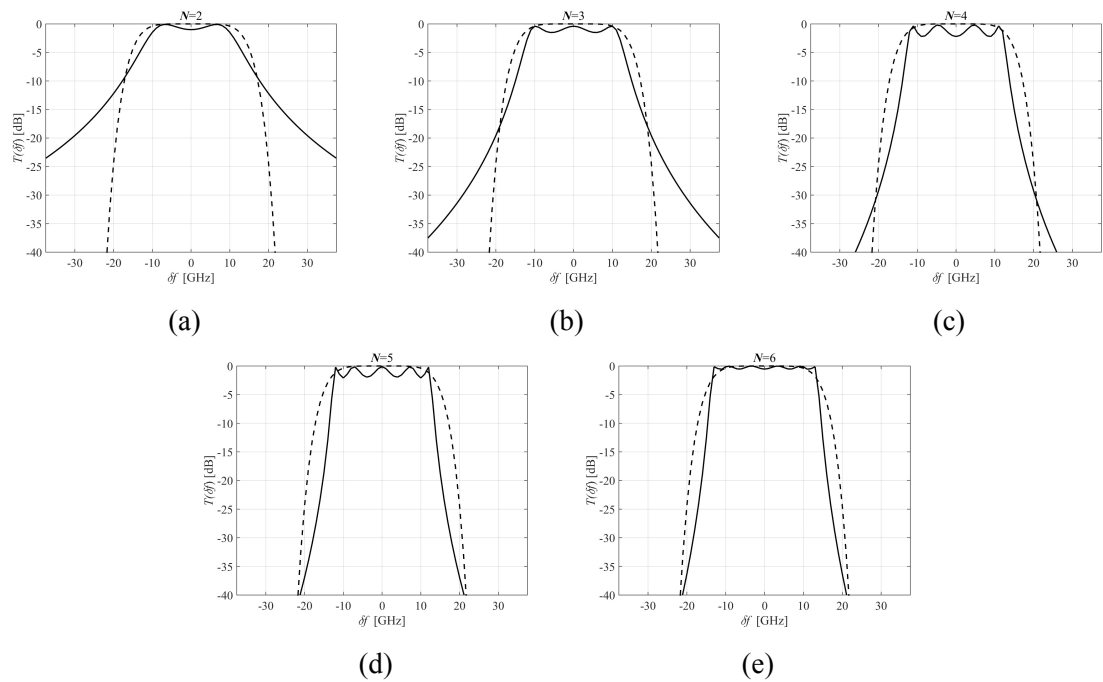


Figure 4.5: Transfer functions near the pass-band obtained for a)  $N = 2$ , b)  $N = 3$ , c)  $N = 4$ , d)  $N = 5$  and e)  $N = 6$  rings. Dashed lines indicate the weighting function  $w(f)$

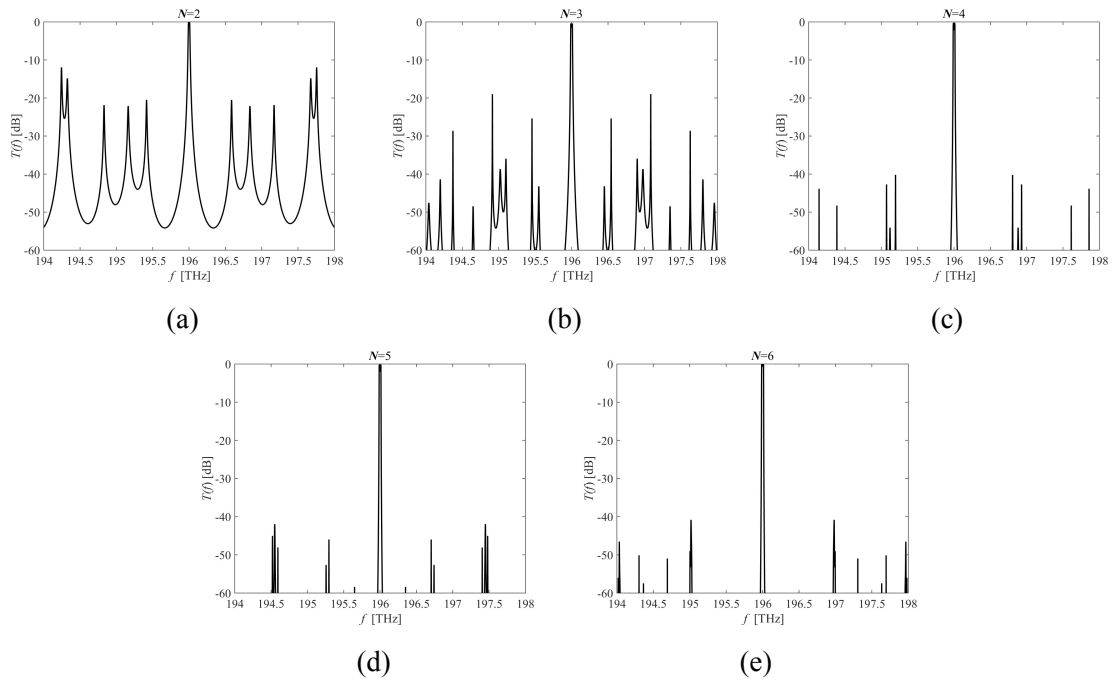


Figure 4.6: Transfer functions in a  $\pm 2$  THz frequency region obtained for a)  $N = 2$ , b)  $N = 3$ , c)  $N = 4$ , d)  $N = 5$  and e)  $N = 6$  rings

A number of interesting observations can be made. As shown in figure 4.3, the coupling coefficients are not symmetric with respect to the central coupling region which is the case for uniform coupled micro-ring structures as presented in [12], [117] and [118]. The outer coupling coefficients  $\kappa_1$  and  $\kappa_{N+1}$  are much larger than the inner coupling coefficients  $\kappa_i$ ,  $2 \leq i \leq N$  and are always fixed to a value of 0.3. In contrast to the necessity of having paired ring radii, as indicated in [117], [118], figure 4.4 suggests that the obtained designs are composed from rings of different sizes and hence we expect that the crosstalk away from the pass-band will be reduced. Regarding the transfer functions shown in figure 4.5 at the vicinity of  $f_0$ , we observe that as the number of rings is increased one gradually obtains sharper transitions from the pass-band to the stop-band. This is quantitatively shown in figure 4.7 where we have plotted the shape factor  $\rho = B_{30\text{dB}}/B_{5\text{dB}}$  of the 30 dB to the 5 dB bandwidth. A large  $\rho$  implies the need for increased channel separation. We deduce that  $\rho$  drops rapidly when increasing the number of rings from  $N = 2$  to  $N = 3$  but the reduction is smaller from then onwards. From  $N = 5$  to  $N = 6$ , the value of changes from  $\rho \approx 1.33$  to  $\rho \approx 1.31$  indicating that by increasing the number of  $N$  beyond 6 is not expected to yield further reductions in  $\rho$ .

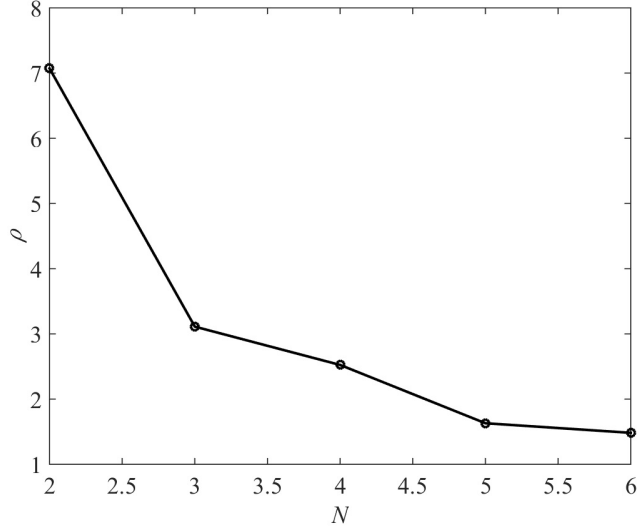


Figure 4.7: Ratio  $\rho$  of the 30 dB bandwidth to the 5 dB bandwidth for the designs in question as a function of the ring number  $N$

It is interesting to note that the definition of the shape factor varies in the literature. For example, in [119] the shape factor is defined as the ratio  $\rho_1 = B_{1\text{dB}}/B_{10\text{dB}}$  of the 1 dB bandwidth over the 10 dB bandwidth. In this case, a larger value for  $\rho_1$  is more favorable. Comparing our results with [119] for the same number of rings, we obtain a value of  $\rho_1 = 0.73$  for the three ring resonator design shown in figure 4.5b (instead of  $\rho_1 = 0.51$  in [119]) while for the four ring resonator design shown in figure 4.5c, we obtain  $\rho_1 = 0.86$  (instead of  $\rho_1 = 0.68$  in [119]). In [118], the shape factor is defined as the ratio  $\rho_2 = B_{20\text{dB}}/B_{3\text{dB}}$  of the 20 dB bandwidth over the 3 dB bandwidth. In this case, a smaller value for  $\rho_2$  is more desirable. Comparing the values of  $\rho_2$  for the two ring resonator designs considered in [118], we obtain  $\rho_2 = 2.69$  for the device shown in figure 4.5a (instead of  $\rho_2 = 3.16$  obtained in [118]).

The crosstalk at the stop-band is another key feature of the obtained designs. Figure 4.6 suggests that away from the vicinity of  $f = f_0$  the crosstalk quickly drops as the number of rings is increased. This stems from the fact that the rings have different radii and hence as the number of rings increases, it is much more difficult to obtain a constructive interference away from the central frequency, unlike the case of uniform structures where the transfer function is periodic [117], [118]. This is further quantified in figure 4.8 where we plot the average and maximum crosstalk  $C_{\text{avg}}$  and  $C_{\text{max}}$  respectively which are defined in the stop-band  $|f - f_0| \geq B_{30}$  as:

$$C_{\text{max}} = \max_{|f-f_0| \geq B_{30}} \{T_{\text{dB}}(f)\} \quad (4.18a)$$

$$C_{\text{avg}} = \langle T_{\text{dB}}(f) \rangle_{|f-f_0| \geq B_{30}} \quad (4.18b)$$

where  $\langle \rangle$  stands for average value. We see that increasing the number of rings quickly reduces both the average and the maximum crosstalk. The fact that the average crosstalk drops more rapidly than the maximum crosstalk suggests a gradual thinning of the side-lobes of the transfer function at the stop-band as a result of the progressive difficulty in obtaining constructive interference.

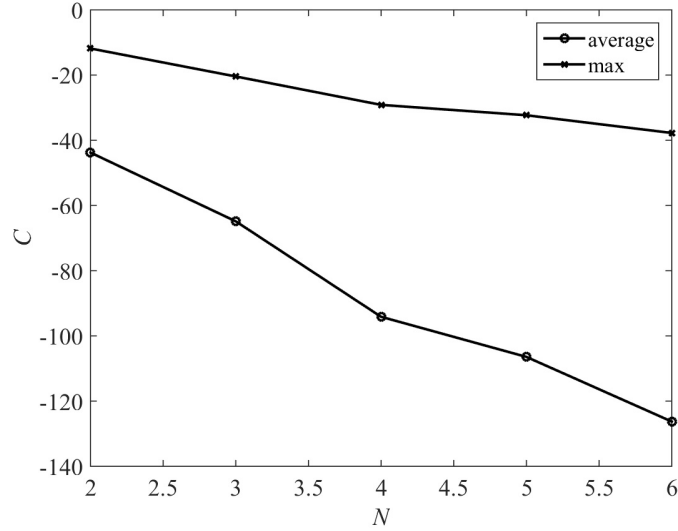


Figure 4.8: Average and maximum crosstalk for the designs as a function of the ring number  $N$

It is also interesting to consider how the progressive transfer functions are obtained at intermediate steps of the optimization process. In figure 4.9, we show these transfer functions at the  $n^{\text{th}}$  step of the minimization assuming  $N = 3$  micro-ring resonators. Initially the transfer function  $T(f)$  is most irregular since we start at a non-optimal point in the multi-parameter space. The minimization process results in the formation of the main lobe. The main lobe is gradually flattened near the desired frequency.

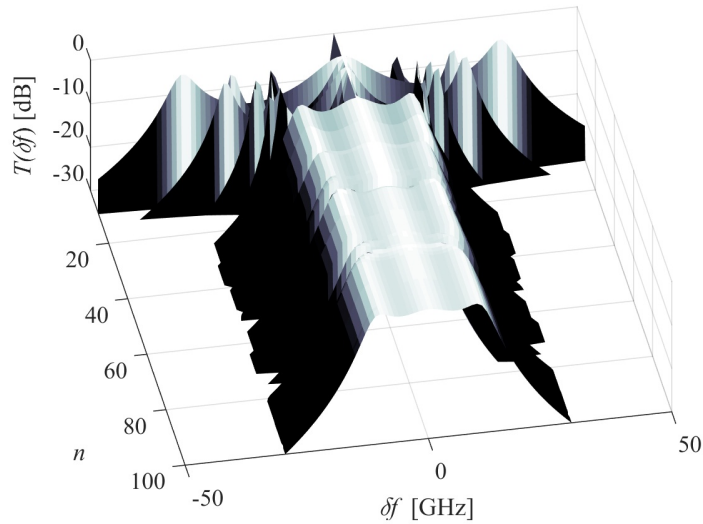


Figure 4.9: Intermediate transfer functions obtained during the minimization process for a three ring structure

In figure 4.10, we compare the chromatic dispersion coefficients  $\Delta\phi_2 = -2\pi c/\lambda^2 \partial^2 \phi / \partial \omega^2$  where  $\phi = \arg\{H\}$  and  $H = a_{4N+4}/a_1$  is the amplitude transfer function of the filter which can be calculated in the same way as  $T(f)$  in section 4.1 for the single-ring ( $N = 1$ ) and the six-ring design ( $N = 6$ ). We deduce that the six-ring design has higher chromatic dispersion. In

an attempt to further investigate the performance of the latter filter we have used the fast-Fourier transform (FFT) to numerically calculate the pulse broadening for an input Gaussian pulse with a 25 ps 1/e full-width and observed a pulse broadening of 12% for the single ring structure and 15% for the multi-ring structure ( $N = 6$ ) implying its suitability for high-speed optical communication applications. For pulses with 50 ps 1/e full-width, the pulse broadening was less than 1% in both cases.

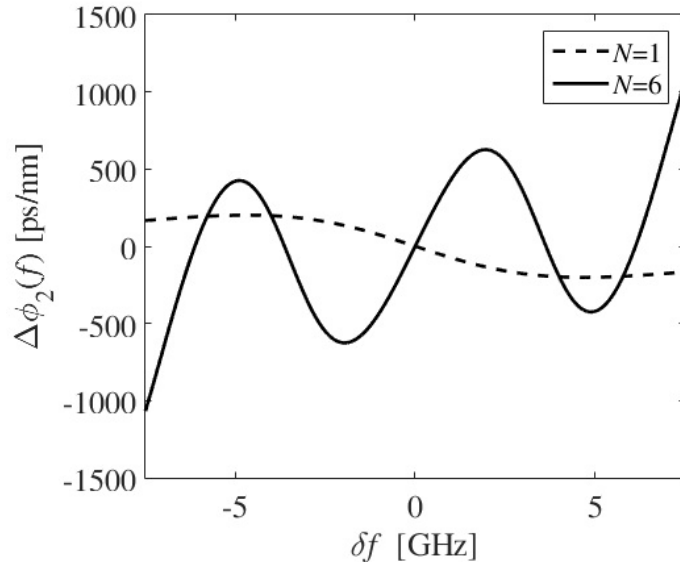


Figure 4.10: Chromatic dispersion of the single ring ( $N = 1$ ) and six ring ( $N = 6$ ) design

We also discuss the impact of the ring waveguide propagation losses on the spectral properties of the device. In practical silicon waveguides, losses may vary from 0.5 dB/cm to  $\sim 6$  dB/cm depending on the fabrication method [120], [121]. In order to assess the impact of the propagation loss on our ring structures we use (4.3) and recalculate the transfer functions taking into account the non-zero loss coefficient  $a$ . Figure 4.11 elaborates on the impact of propagation loss in the spectral characteristics of the six-ring design mentioned above. The figure shows that although ring waveguide propagation losses result in insertion losses for the optical filter, the shape of the transfer function remains flat even at high values of  $a$ . This is quantified in table 4.1, where the ratio  $\rho$  corresponds to the four loss coefficients mentioned in the legend of figure 4.11.

$a$	$\rho$
0 dB/cm	1.32
0.5 dB/cm	1.32
3 dB/cm	1.42
6 dB/cm	1.76

Table 4.1: Ratio  $\rho$  corresponding to the four loss coefficients

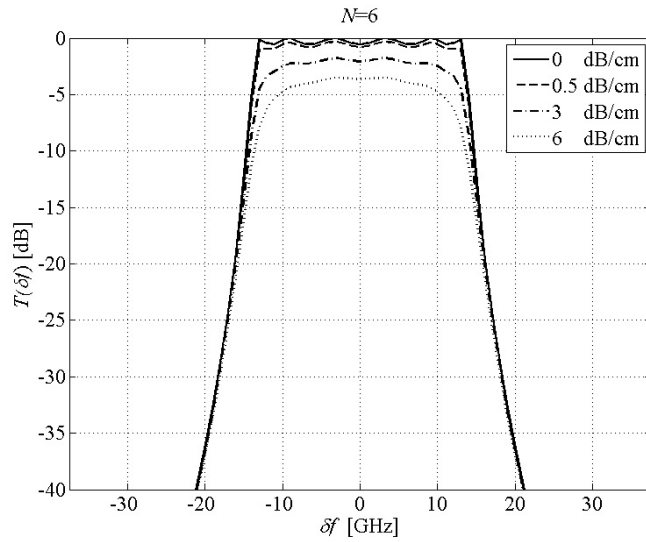


Figure 4.11: Comparison of the transfer function of a 6 ring design for different loss factors

## 4.4 Conclusions

In the analysis presented in this chapter, we discussed the tailoring of the spectral properties of coupled micro-ring structures. By allowing non-uniform resonator arrangements we show how standard minimization methods can be used to design the structure with desirable spectral characteristics without resorting to complex analytical schemes or exhaustive search in a multi-parameter space. The obtained transfer functions are relatively flat and are characterized by very low cross-talk unlike a uniform array of micro-ring resonators where the stop-band is limited by the periodic nature of the transfer function. Our technique may open up new paths for designing and implementing compact optical filters with tailored spectral properties.

## 5 Designing RR structures

In this chapter an analytical model for estimating the spectral properties of an active racetrack resonator/waveguide system, which directly involves all pertinent parameters, will be presented. Under reasonable approximations, we will show that the transfer function can be approximated by a rational function, the coefficients of which are determined by the parameters of the structure and whose poles significantly determine the spectral properties of the device. We also provide expressions for estimating the maxima and minima of the power transfer function  $T = |H|^2$ . The intra-cavity reflections arising at the interfaces between the straight and the curved waveguides of the racetrack, provide an additional degree of freedom in the design of the spectral properties of the device and under certain conditions Fano-type resonances appear which can be useful in a number of applications including optical sensing. Additionally, the conditions under which asymmetric transitions around a spectral peak can occur which are characteristic of Fano-type resonances will be identified. The accuracy of our model is verified by rigorous transfer matrix numerical simulations. Suitable metrics that can be used to optimize the design are identified along with a set of conditions that the transfer function must fulfill from an application point-of-view. We show how the design parameters involved in the transfer function calculation, can be used to determine the required structural and material parameters of the device and provide examples of structure designs that possess favorable spectral characteristics. We also discuss how the model can be applied for tailoring the transfer function in order to obtain sharper transitions from the spectral peaks to the minima and higher contrast between the minima and the maxima of  $T$ , as stated in chapter 2, in order for the structure to be used for sensing applications. To our knowledge, this is the first time an analytical model, which includes the effects of reflectivity, is presented. The results of this work were published in [122] and [123].

### 5.1 Transfer matrix analysis

Figure 5.1 shows the basic coupled racetrack/waveguide system. At the waveguide input, let  $A_{in}$  be the amplitude of the incident wave and  $A_r$  the amplitude of the reflected wave, while  $A'_{in}$  and  $A'_r$  denote the amplitudes of the incident and the output fields at the device output. We also assume that  $R'_{CCW}$  and  $R'_{CW}$  are the amplitudes of the counter-clockwise and clockwise propagating fields at the input of the coupling region while  $R_{CCW}$  and  $R_{CW}$  are the corresponding fields at the output of the coupling region.

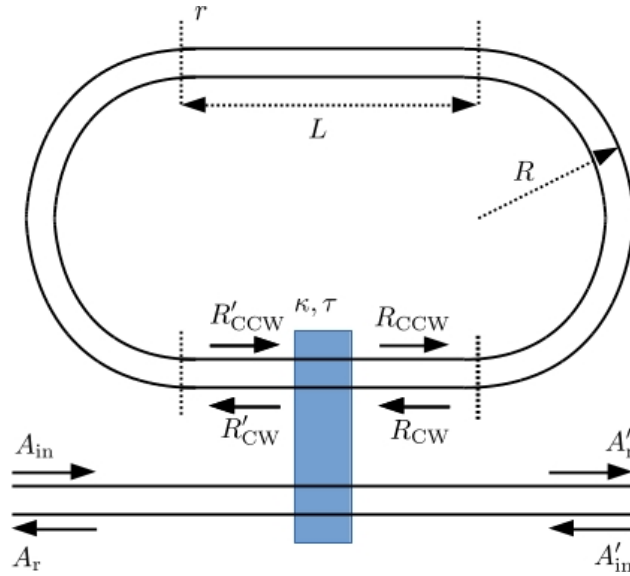


Figure 5.1: The coupled racetrack resonator / waveguide system. In the figure  $A_{in}$ ,  $A_r$  are the amplitudes of the incident and reflected waves at the input,  $A'_{in}$  and  $A'_r$  are the corresponding waves at the output, while  $R'_{CCW}$  and  $R'_{CW}$  are the amplitudes of the counter-clockwise and clockwise propagating fields at the input of the coupling region and  $R_{CCW}$  and  $R_{CW}$  are the corresponding fields at its output.

The device can be described by the total transfer matrix of the system  $\mathbf{M}$ , which relates the fields at the racetrack:

$$\begin{bmatrix} R'_{CCW} \\ R'_{CW} \end{bmatrix} = \mathbf{M} \begin{bmatrix} R_{CCW} \\ R_{CW} \end{bmatrix} \quad (5.1)$$

The *amplitude* transfer function of the device  $H(\omega)$  is given by the ratio  $\frac{A'_r}{A_{in}}$  of the input and output waveguide mode field and is calculated by the following equation according to the analysis presented in section 3.6 and [96]:

$$H(\omega) = \frac{A'_r}{A_{in}} = \frac{1}{\sqrt{\tau}} + \frac{\kappa}{\sqrt{\tau}} \times \frac{\sqrt{\tau} - m_{22}}{m_{12}m_{21}\sqrt{\tau} - (1 - m_{11}\sqrt{\tau})(\sqrt{\tau} - m_{22})} \quad (5.2)$$

where  $\omega = 2\pi f$  is the frequency. The power transfer function  $T(\omega)$  is simply determined as  $T(\omega) = |H(\omega)|^2$ .

In (5.2),  $\tau$  and  $\kappa$  denote the *power* transmission and coupling coefficient respectively, between the waveguide and the racetrack with  $\kappa + \tau = 1$ , while  $m_{pq}$  are the elements of the total transfer matrix of the system  $\mathbf{M}$ :

$$\mathbf{M} = \begin{bmatrix} m_{11} & m_{12} \\ m_{21} & m_{22} \end{bmatrix} \quad (5.3)$$

The coupling coefficient  $\kappa$  can be calculated using the coupled mode theory which may incorporate full-blown computational methods such as the finite difference time domain and the finite difference frequency domain methods as analytically described in chapter 3.

The total transfer matrix  $\mathbf{M}$  can be written as a product of the individual transfer matrices of the various device sections:

$$\mathbf{M} = \mathbf{M}_S \left(\frac{L}{2}\right) \mathbf{M}_T \mathbf{M}_C \mathbf{M}_T \mathbf{M}_S(L) \mathbf{M}_T \mathbf{M}_C \mathbf{M}_T \mathbf{M}_S \left(\frac{L}{2}\right) \quad (5.4)$$

In (5.4),  $L$  is the length of the straight waveguide section and the sub-matrices are defined in a manner analogous to the total matrix  $\mathbf{M}$ . The matrix  $\mathbf{M}_S(l)$  describes the propagation in a straight waveguide section of length  $l$  and is determined by:

$$\mathbf{M}_S(l) = \begin{bmatrix} e^{-j\beta_S l} & 0 \\ 0 & e^{j\beta_S l} \end{bmatrix} \quad (5.5)$$

where  $\beta_S$  is the propagation constant of the waveguide mode.  $\mathbf{M}_C$  is the matrix describing the propagation in the half-circle of radius  $R$ :

$$\mathbf{M}_C = \begin{bmatrix} e^{-j\beta_C \pi R} & 0 \\ 0 & e^{j\beta_C \pi R} \end{bmatrix} \quad (5.6)$$

where  $\beta_C$  is the propagation constant in the half-circle waveguide.  $\mathbf{M}_T$  is the matrix describing the transition from a curved to a straight interface and *vice-versa*:

$$\mathbf{M}_T = \frac{1}{j\sqrt{1-r^2}} \begin{bmatrix} -1 & -r \\ r & 1 \end{bmatrix} \quad (5.7)$$

where  $r$  is the power reflection coefficient at the interfaces between the straight and the curved sections. The propagation constants in (5.5) and (5.6) are determined by:

$$\beta_S = \frac{\omega n_S}{c} + j\frac{g_S}{2} \quad (5.8)$$

$$\beta_C = \frac{\omega n_C}{c} + j\frac{g_C}{2} \quad (5.9)$$

where  $g_S$  and  $g_C$  are the gain coefficients of the straight and curved section, which also include the various losses of the device, while  $n_S$  and  $n_C$  are the *effective* indices of the straight and curved section respectively and  $c$  the speed of light in vacuum. The transfer matrix model described by (5.2)-(5.9) can be used to estimate the spectral properties of the device taking into account the intracavity reflections described by the reflection coefficient  $r$ . In the next sections, we will develop an analytical model that can yield significant insight in the influence of the various parameters and study the spectral properties of the transfer function, paying particular attention to the formation of Fano-type resonances.

### 5.1.1 Transfer matrix elements approximations

We define the auxiliary phase differences in order to facilitate our calculations. The phase difference  $\phi$  when propagating in the straight waveguide section of length  $L$  is equal to:

$$\phi(\omega) = \beta_S L = \frac{\omega n_S}{c} L + j\frac{g_S}{2} L \quad (5.10)$$

The phase difference  $\theta$  when propagating in the half-circle section of the racetrack is given by:

$$\theta(\omega) = \beta_C \pi R = \frac{\omega n_C}{c} \pi R + j \frac{g_C}{2} \pi R \quad (5.11)$$

The round-trip phase difference  $\Psi$  is calculated as:

$$\begin{aligned} \Psi(\omega) &= 2(\phi(\omega) + \theta(\omega)) \\ &= \frac{\omega n_C}{c} 2L + \frac{\omega n_S}{c} 2\pi R + j g_S L + j g_C \pi R \end{aligned} \quad (5.12)$$

Taking into account (5.3)-(5.12), we obtain the following closed-form expressions for the elements of the transfer matrix:

$$m_{11} = -\frac{e^{-j\Psi}}{(r^2 - 1)^2} \left\{ r^2 e^{j2\phi} + 2r^2 e^{j2\theta} - r^4 e^{j4\theta} - 2r^2 e^{j\Psi} + r^2 e^{j\Psi+j2\theta} - 1 \right\} \quad (5.13)$$

$$m_{12} = -m_{21} = -\frac{r e^{-j\Psi+j\phi}}{(r^2 - 1)^2} \left\{ e^{j2\theta} - e^{j\Psi} + e^{j\Psi+j2\theta} + r^2 e^{j2\phi} + r^2 e^{j2\theta} - r^2 e^{j4\theta} - r^2 e^{j\Psi} - 1 \right\} \quad (5.14)$$

$$m_{22} = \frac{e^{-j\Psi}}{(r^2 - 1)^2} \left\{ e^{j2\Psi} + r^4 e^{j4\phi} + 2r^2 e^{j\Psi} - r^2 e^{j\Psi+j2\theta} - 2r^2 e^{j\Psi+j2\phi} - r^2 e^{j2\phi} \right\} \quad (5.15)$$

Equations (5.13)-(5.15) can be used in order to directly calculate the total matrix elements without resorting to matrix multiplications. For small reflectivity  $r$  ( $r \ll 1$ ), the matrix elements can be accurately approximated by:

$$m_{11} \cong e^{-j\Psi} \quad (5.16)$$

$$m_{12} = -m_{21} \cong -r e^{-j\Psi+j\phi} (e^{j2\theta} - e^{j\Psi+j2\theta} - 1) \quad (5.17)$$

$$m_{22} \cong e^{j\Psi} \quad (5.18)$$

Equations (5.16)-(5.18) show that to first order, only the non-diagonal elements  $m_{12}$  and  $m_{21}$  contain the influence of  $r$ . Multiple reflections giving rise to higher powers  $r^n$  of  $r$  with  $n > 1$  in the elements  $m_{pq}$  can be ignored in this case. Since Fano resonances are typically associated with low reflection values [96], we will consider the low reflectivity approximation for the remainder of our analytical treatments.

Let  $\omega = \omega_0 = 2\pi f_0$  be a resonant angular frequency of the racetrack resonator, measured in rad/s. In this case the real part of the round-trip phase  $\Psi_0 = \Psi(\omega_0) = 2\theta_0 + 2\phi_0$  where  $\theta_0 = \theta(\omega_0)$  and  $\phi_0 = \phi(\omega_0)$ , must be a multiple of  $2\pi$ , i.e.  $\Re\{\Psi_0\} = 2\mu\pi$  where  $\mu$  is an integer referred to as the resonance order, or equivalently,

$$\frac{2n_S f_0 L}{c} + \frac{2n_C f_0 \pi R}{c} = \mu \quad (5.19)$$

where  $f_0 = \omega_0/2\pi$  is the resonant frequency, measured in Hz. Also at resonance:

$$e^{j\Psi_0} = e^{-g_S L - g_C \pi R} e^{j2\mu\pi} = \frac{1}{\sqrt{G}} \quad (5.20)$$

where  $G$  is the roundtrip gain determined by:

$$G = e^{2g_S L + 2g_C \pi R} = e^{2g_{\text{avg}}(\pi R + L)} \quad (5.21)$$

In (5.21),  $g_{\text{avg}}$  is the average gain coefficient across the racetrack path. Using (5.20), (5.16)-(5.18) and assuming  $r \ll 1$  we obtain:

$$m_{11}(\omega_0) \cong \sqrt{G} \quad (5.22)$$

$$g \triangleq m_{12}(\omega_0) \cong -r e^{j\phi_0} \left( \sqrt{G} + 1 \right) \left( e^{j2\theta_0} - 1 \right) \quad (5.23)$$

$$m_{22}(\omega_0) \cong \frac{1}{\sqrt{G}} \quad (5.24)$$

where to simplify the notation we denoted the value of  $m_{12}$  at resonance as  $g$ .

Considering a small frequency detuning  $\Delta\omega = \omega - \omega_0$  around the resonant frequency  $\omega_0$ , we can expand the propagation constants in (5.8) and (5.9) around  $\omega = \omega_0$  as:

$$\beta_S(\omega) = \beta_S(\omega_0 + \Delta\omega) \cong \beta_S(\omega_0) + \beta_{S1} \Delta\omega \quad (5.25)$$

$$\beta_C(\omega) = \beta_C(\omega_0 + \Delta\omega) \cong \beta_C(\omega_0) + \beta_{C1} \Delta\omega \quad (5.26)$$

where  $\beta_{S1}$  and  $\beta_{C1}$  are the first-order derivatives of the propagation constants calculated at  $\omega = \omega_0$ . We may also write:

$$\Psi(\omega) = \Psi(\omega_0) + \Delta\Psi \quad (5.27)$$

with

$$\Delta\Psi = 2(\beta_{S1} L + \beta_{C1} \pi R) \Delta\omega \quad (5.28)$$

We define the frequency scaling factor  $S$  to be equal  $S = \beta_{S1} L + \beta_{C1} \pi R$  and the normalized frequency  $\Omega = S \Delta\omega$ . We choose to retain a first order expansion in terms of  $\Omega$  for the diagonal elements  $m_{11}$  and  $m_{22}$ . Using (5.16) and (5.18), we obtain the following first order expansion:

$$m_{11} \cong \sqrt{G} - j2\Omega\sqrt{G} \quad (5.29)$$

$$m_{22} \cong \frac{1}{\sqrt{G}} + \frac{j2\Omega}{\sqrt{G}} \cong \frac{m_{11}^*}{G} \quad (5.30)$$

Figure 5.2 shows the accuracy of the first-order approximation by comparing the values obtained for  $m_{11}$  by (5.4) and (5.29). The parameters chosen are adapted from [96]. We deduce that the first-order approximation accurately captures the variations of the imaginary part of  $m_{11}$ . The real part of  $m_{11}$  exhibits a maximum at  $\omega = \omega_0$  and can not be described using a first-order approximation. However the variations of the real part are much smaller than the imaginary part. Also, since the

non-diagonal elements  $m_{12}$  and  $m_{21}$  can be treated as perturbations we retain only the zero-order term and assume:

$$m_{12}(\omega) = -m_{21}(\omega) \cong g \quad (5.31)$$

where  $g$  is determined by (5.23). The validity of these approximations will further be discussed in the next section.

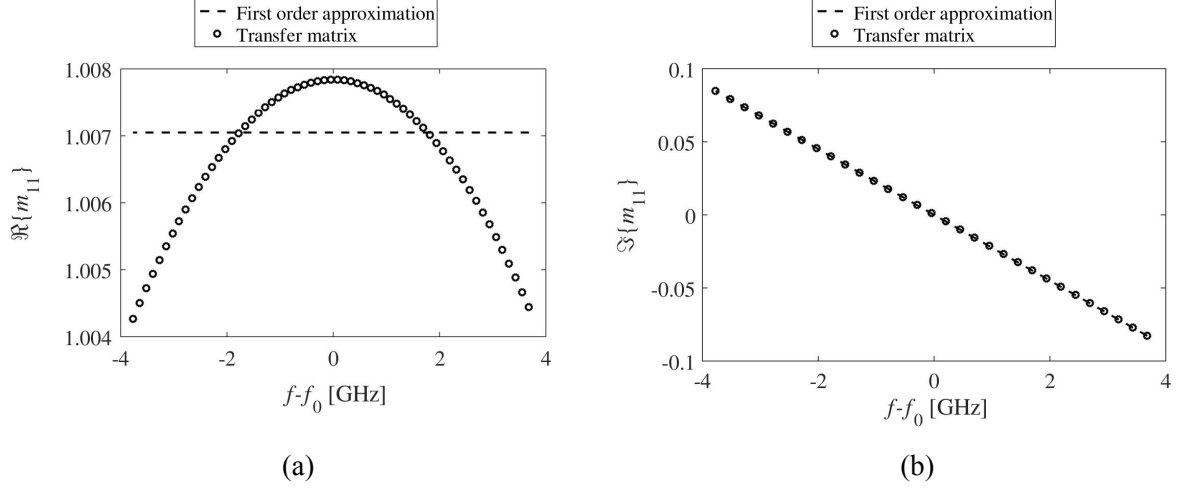


Figure 5.2: First order approximation for a) the real and b) the imaginary part of the diagonal matrix element  $m_{11}$  assuming the parameters of table 5.1.

## 5.2 Transfer function model

Using (5.29), (5.30) and (5.31) in (5.2), we obtain after some mathematical manipulation the following rational function for  $H$ :

$$H = \frac{1}{\sqrt{\tau}} \frac{A\Omega^2 + E\Omega + F}{A\Omega^2 + B\Omega + C} \quad (5.32)$$

where the following coefficients are used:

$$A = -4\sqrt{\tau} \quad (5.33)$$

$$B = 2j \left( \frac{1}{\sqrt{G}} - \tau\sqrt{G} \right) \quad (5.34)$$

$$C = -2\sqrt{\tau} + \frac{1}{\sqrt{G}} + \tau\sqrt{G} - g^2\sqrt{\tau} \quad (5.35)$$

$$E = \frac{2j\tau}{\sqrt{G}} - 2j\tau\sqrt{G} \quad (5.36)$$

$$F = \frac{\tau}{\sqrt{G}} + \kappa\sqrt{\tau} - 2\sqrt{\tau} + \tau\sqrt{G} - g^2\sqrt{\tau} \quad (5.37)$$

According to (5.32), the amplitude transfer function  $H$  can be written as a rational function where both the numerator and the denominator are second-order polynomials of the normalized frequency

$\Omega$ . The coefficients of the polynomials depend on three parameters: the roundtrip gain  $G$ , the power coupling coefficient  $\kappa = 1 - \tau$  and the off-diagonal element of the transfer matrix  $g = m_{12}(\omega_0)$  at resonance determined by (5.23). The material ( $n_C, n_S$ ) and structural parameters ( $L, R$ ) of the racetrack determine the resonant frequency  $f_0$  around which the transfer function is obtained and the value of  $g$  also contains the impact of the intra-cavity reflections. (5.32) is far more suitable for analytic manipulations than the transfer matrix model of section 5.1.

It is useful to write the rational function (5.32) in a slightly alternative form using only real coefficients, which is a form that will be used in the following sections:

$$H = \frac{1}{\sqrt{\tau}} \frac{\Omega^2 + ju_1\Omega + u_0}{\Omega^2 + jv_1\Omega + v_0} \quad (5.38)$$

with:

$$v_1 = \frac{Y^2 - 1}{2Y} \quad (5.39)$$

$$v_0 = \frac{g^2 + 2 - Y - \frac{1}{Y}}{4} \quad (5.40)$$

$$u_1 = \frac{Y^2 + \kappa - 1}{2Y} = v_1 + \frac{\kappa}{2Y} \quad (5.41)$$

$$u_0 = -\frac{(-\kappa + 1 - Y)(1 - Y) - g^2}{4Y} = v_0 + \frac{\kappa(1 - Y)}{4Y} \quad (5.42)$$

Before we apply the analytical model to describe the spectral properties of the device, it is useful to ascertain the accuracy of the analytical approximations. Figure 5.3 shows the transfer function calculated for both the full transfer matrix model described by (5.2) and (5.4) and its analytical approximation given by (5.32) for the set of parameters quoted in table 5.1. The material and structural parameters of the racetrack are adapted from [96]. We see that the low-reflectivity and first-order approximation accurately describes the shape of the power transfer function  $T = |H|^2$  at the frequency range of interest.

Parameter	Value	Parameter	Value
$n_S$	3.6	$G$	1.041
$n_C$	3.5	$g$	0.0397j
$g_S$	-0.2cm <sup>-1</sup>	$S$	1.78ps
$g_C$	3cm <sup>-1</sup>	$f_0$	193.02THz
$L$	120μm	$\mu$	1372
$R$	10μm	$e_\phi = e^{j\phi_0}$	0.11 + 0.99j
$r$	0.01	$e_\theta = e^{j\theta_0}$	0.11 - 0.98j
$\kappa$	0.025		

Table 5.1: Initial racetrack parameters

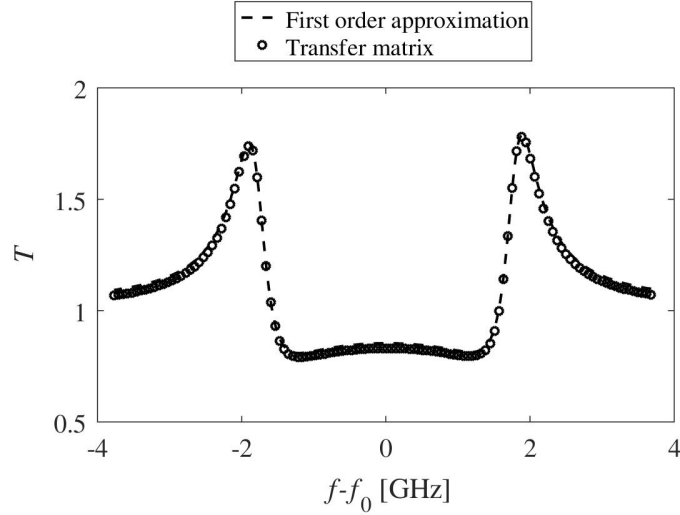


Figure 5.3: Comparison of the transfer functions calculated for by (5.2)-(5.4) and the rational approximation (5.32) for the set of parameters quoted in table 5.1.

The rational transfer function in (5.32) can be written in a more suitable form using partial fraction decomposition [124]. Let  $\Omega = \rho_1$  and  $\Omega = \rho_2$  be the poles of  $H$  in (5.32). The discriminant  $\Delta$  of the equation is determined by:

$$I_r^2 = \frac{\Delta G}{4} = -(Y - 1)^4 - 4g^2Y \quad (5.43)$$

where

$$Y = \sqrt{\tau G} \quad (5.44)$$

In the absence of reflections ( $r = 0$ ) one obtains  $g = 0$  and hence the discriminant  $\Delta_0$  is determined by:

$$I_0^2 = \frac{\Delta_0 G}{4} = -(Y - 1)^4 \quad (5.45)$$

and is negative. Since the sum of the poles,  $-B/A$ , is imaginary as suggested by (5.33) and (5.34), this implies that the poles  $\rho_1$  and  $\rho_2$  in this case will be purely imaginary. In the general case, the poles are given by:

$$\rho_{1,2} = \frac{j(1 - Y^2) \pm I_r}{4Y} \quad (5.46)$$

The roots  $\rho_1$  and  $\rho_2$  determine the poles of the partial fraction decomposition of the transfer function.

$$H = \frac{1}{\sqrt{\tau}} + \frac{c_1}{\Omega - \rho_1} + \frac{c_2}{\Omega - \rho_2} \quad (5.47)$$

where

$$c_1 = \frac{\kappa}{A\sqrt{Y}} \left( \frac{(Y - 1)^2}{I_r} - j \right) \quad (5.48)$$

$$c_2 = \frac{\kappa}{A\sqrt{Y}} \left( -\frac{(Y - 1)^2}{I_r} - j \right) \quad (5.49)$$

(5.47) shows that the transfer function of the device can be written as the sum of a constant term and two Lorentzian functions  $H_i$  determined by the poles  $\rho_i = \rho'_i + j\rho''_i$ :

$$H_i(\Omega) = \frac{c_i}{(\Omega - \rho'_i) - j\rho''_i} \quad (5.50)$$

The real part  $\rho'_i$  of the poles  $\rho_i$  is associated with the frequency detuning of the two spectral peaks of the transfer function, while the imaginary part  $\rho''_i$  determines the linewidth of the resonances.

### 5.3 Symmetric resonances

We next consider the special case where  $\rho_1 = -\rho_2^*$  which according to (5.46) occurs when  $I_r$  determined by (5.43) is real, i.e.:

$$-(Y - 1)^4 - 4g^2Y \geq 0 \quad (5.51)$$

In this case,  $\rho'_1 = -\rho'_2$  implying that the peaks of two Lorentzian functions occurring at  $\Omega = \rho'_1$  and  $\Omega = \rho'_2$  are placed symmetrically around  $\Omega = 0$ . Also, since  $\rho''_1 = \rho''_2$ , the linewidths of the two functions are the same. In addition using (5.48) and (5.49) given the fact that  $I_r$  is real, we obtain:

$$c_1 = -c_2^* \quad (5.52)$$

and hence the peak amplitude of the two Lorentzian components is determined by  $|H_i(\rho'_i)| = |c_i/\rho''_i|$ . Using (5.50) we deduce that the transfer components  $H_i(\Omega)$  are related through  $H_1(\Omega) = H_2^*(-\Omega)$  and hence:

$$H(\Omega) = H^*(-\Omega) \quad (5.53)$$

implying that the power transfer function  $T(\Omega) = |H(\Omega)|^2$  is symmetric around  $\Omega = 0$ . In this case, we can use (5.38) to derive a convenient form for  $T(\Omega) = |H(\Omega)|^2$ :

$$T(\Omega) = \frac{1}{\tau} \frac{(\Omega^2 + u_0)^2 + u_1^2\Omega^2}{(\Omega^2 + v_0)^2 + v_1^2\Omega^2} \quad (5.54)$$

The function  $T(\Omega)$  determined by (5.54) is a function of  $x = \Omega^2$  alone and one can find the extrema by differentiating  $T(x)$  with respect to  $x$ . After some mathematical manipulation, we can find that the extrema of  $T$  located at the positive  $\Omega$ -axis are  $\Omega = \Omega_{\text{ext}}$  where:

$$\Omega_{\text{ext}}^2 = \frac{v_0^2 - u_0^2 \pm \Theta}{u_1^2 - v_1^2 + 2(u_0 - v_0)} \quad (5.55)$$

The parameter  $\Theta$  is determined by:

$$\Theta^2 = ((u_0 - v_0)^2 - u_0v_1^2 - u_1^2v_0)^2 - (u_0u_1v_1 + u_1v_0v_1)^2 \quad (5.56)$$

Note that for the design of table 5.1, the parameter  $g^2$  is negative and  $I_r^2 \cong 6.28 \times 10^{-3} > 0$  implying that the transfer function is symmetric as already indicated by figure 5.3. Using (5.55) and (5.56) we can find the non-zero extrema of  $T$  that are located at  $\Omega_{\text{ext}} = \pm 0.0134$  and  $\Omega_{\text{ext}} = \pm 0.0212$ . The frequencies corresponding to  $\Omega_{\text{ext}}$  can be found through  $f_{\text{ext}} = \Omega_{\text{ext}}/(2\pi S)$ . For the parameters of table 5.1, we obtain  $f_{\text{ext}} = \pm 1.2\text{GHz}$  and  $f_{\text{ext}} = \pm 2.02\text{GHz}$  which is in excellent agreement with the extrema observed in figure 5.3.

### 5.3.1 Fano resonance tailoring in the symmetric case

In this section, we apply the analytical model presented in section 5.1.1 in order to design a race-track/waveguide system exhibiting asymmetric transfer function near the vicinity of its spectral peak. Such properties are useful in sensor applications where one seeks spectral regions where the transmittance exhibits sharp transitions from a maximum to a minimum value. We focus our attention to the symmetric case discussed in section 5.3. As pointed out at that section, the parameter  $g = jg''$  should be imaginary and (5.51) should be fulfilled so that the poles obey the condition  $\rho_1 = -\rho_2^*$ . Given the definition of  $g$  in (5.23), we deduce that:

$$e^{j\phi_0} (e^{j2\theta_0} - 1) = \pm \frac{jg''}{r} \frac{1}{\sqrt{G+1}}. \quad (5.57)$$

Taking into account (5.10) and (5.11), we deduce that (5.57) imposes certain restrictions on the parameters  $R$  and  $L$ . For the values of  $R$  and  $L$  in table 5.1, we see that  $g$  is almost purely imaginary and hence (5.57) already holds. Keeping  $R$  and  $L$  constant and varying  $r$  or  $G$  we can therefore change the value of  $g''$  at will. Since only  $g^2$  appears in the equations, the sign of  $g''$  is of no consequence. We therefore assume that  $g'' > 0$ . Given that (5.57) holds, there are three parameters that determine the transfer function:

- the *roundtrip power gain*  $G$  ( $G \geq 1$ ).
- the *power transmission coefficient*  $\tau$  ( $\tau < 1$ ).
- the parameter  $g = jg''$  assumed to be purely imaginary which is a necessary condition in order to fulfill (5.51).

In order to identify a suitable design we perform an exhaustive search over a three-dimensional uniform grid of values  $(m_G \Delta G, m_\tau \Delta \tau, m_g \Delta g)$  where  $\Delta G$ ,  $\Delta \tau$  and  $\Delta g$  denote the grid spacing for the parameters  $G$ ,  $\tau$  and  $g''$  and  $m_G$ ,  $m_\tau$ ,  $m_g$  are integers. In our application we have chosen  $\Delta G = 0.001$ ,  $\Delta \tau = 0.001$  and  $\Delta g = 0.001$  while the range of values considered is  $G \in [1.01, 1.2]$ ,  $\tau \in [0.8, 0.98]$  and  $g'' \in [0.02, 0.1]$  resulting in a  $191 \times 181 \times 81$  parameter grid. For each set of parameters  $(G_q, \tau_q, g''_q)$  in the grid we check to see whether the condition (5.51) is fulfilled. If this is the case, we calculate the two extrema  $\Omega_{\text{ext}} > 0$  lying in the positive  $\Omega$ -axis based on (5.55) and based on the value of  $T(\Omega_{\text{ext}})$ , we find which one of them is the location of the maximum  $\Omega_{\text{max}}$  and the minimum  $\Omega_{\text{min}}$  and estimate the spacing between the minimum and the maximum:

$$\Delta \Omega = |\Omega_{\text{max}} - \Omega_{\text{min}}| \quad (5.58)$$

We also calculate the contrast:

$$r_C[\text{dB}] = 10 \log_{10} \left( \frac{T(\Omega_{\text{max}})}{T(\Omega_{\text{min}})} \right) \quad (5.59)$$

We consider the designs for which  $r_C$  exceeds a threshold value  $r_{\text{min}}$ , in our case 5 dB, which offers sufficient contrast between the minimum and maximum values.  $\Delta \Omega$  can be considered

as a figure of merit in our design process. The lower the value of  $\Delta\Omega$ , the sharper transition we expect from the maximum to the minimum and hence the design will be more favorable for sensing applications. If for a set of parameters, the condition in (5.51) is not fulfilled or if  $r_C < r_{\min}$ , then we set  $\Delta\Omega = 0$ . After the exhaustive search is complete, we choose the design with the lowest non-zero value  $\Delta\Omega$ .

Figure 5.4 shows the optimized design. The design of table 5.1 is also included as a reference. Table 5.2 summarizes the parameters for the optimized design. Given the values of  $g''$ ,  $G$  and  $\tau$  obtained through exhaustive search we can calculate the rest of the parameters of the structure. We choose to retain the same values for  $n_C$ ,  $n_S$ ,  $R$  and  $L$  as in table 5.1. This implies that the resonant frequency  $f_0$  and the order  $\mu$  of the resonance are the same. We have also chosen the value  $g_C = 2.5\text{cm}^{-1}$  for the gain of the curved section in order to obtain a roundtrip gain value of  $G = 1.011$ . The power coupling coefficient is obtained through  $\kappa = 1 - \tau$  while the value of the reflectivity  $r$  is obtained by solving (5.57) with respect to  $r$ :

$$r = \left| \frac{jg''}{\sqrt{G} + 1} \frac{1}{e^{j\phi_0} (e^{j2\theta_0} - 1)} \right|. \quad (5.60)$$

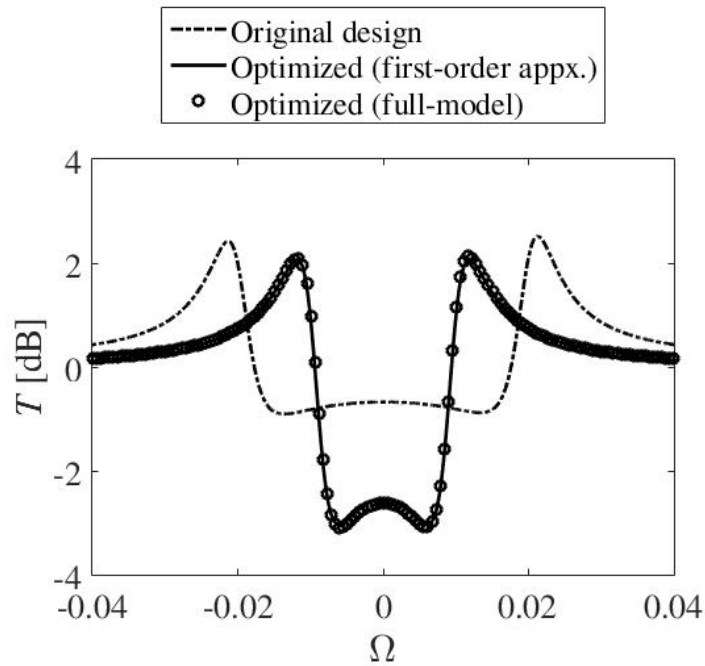


Figure 5.4: Transfer functions of the original designs outlined in table 5.1 and the optimized design of table 5.2, calculated by the rational first-order approximation and the full transfer matrix model.

Figure 5.4 includes the transfer function for the optimized design using just the values of  $g''$ ,  $G$  and  $\kappa$  obtained through exhaustive search based on the rational transfer function mode of (5.32) with a solid line and the transfer function obtained by applying the full transfer function model of section 5.1 with circles. We again obtain an excellent agreement for this case as well since the value of  $r$  is much smaller than unity. The optimized design has larger contrast ( $\cong 5.1$  dB) between the maximum and the minimum compared to the original design ( $\cong 3.4$  dB). For the

Parameter	Value	Parameter	Value
$n_S$	3.6	$G$	1.011
$n_C$	3.5	$g$	$0.02j$
$g_S$	$-0.2\text{cm}^{-1}$	$S$	1.78ps
$g_C$	$2.5\text{cm}^{-1}$	$f_0$	193.02THz
$L$	$120\mu\text{m}$	$\mu$	1372
$R$	$10\mu\text{m}$	$e_\phi = e^{j\phi_0}$	$0.11 + 0.99j$
$r$	0.005	$e_\theta = e^{j\theta_0}$	$0.11 - 0.98j$
$\kappa$	0.021		

Table 5.2: Parameters for optimized design

original design we have  $\Delta\Omega = 6.2 \times 10^{-3}$  while the optimized design yields  $\Delta\Omega = 5.5 \times 10^{-3}$ . Between the maximum and the minimum, the average rate of change, defined as:

$$r_{\text{ch}} = \frac{\Delta T}{\Delta f} = \frac{T(\Omega_{\text{max}}) - T(\Omega_{\text{min}})}{f_{\text{max}} - f_{\text{min}}} \quad (5.61)$$

where  $f_{\text{max}} = \Omega_{\text{max}}/S$  and  $f_{\text{min}} = \Omega_{\text{min}}/S$  are the frequencies corresponding to the maximum and the minimum respectively, is  $r_{\text{ch}} = 4.8 \text{ GHz}^{-1}$  for the initial design and  $r_{\text{ch}} = 9.8 \text{ GHz}^{-1}$  for the optimized design. We therefore deduce that the transition region between the peak and the minimum is shorter for the latter.

Figure 5.5 shows the effect of small perturbations  $\Delta n_S$  of the effective index  $n_S$  of the straight section. The transfer function is plotted as a function of  $f - f_0$  where  $f_0$  is the resonant frequency of the design with  $\Delta n_S = 0$ .

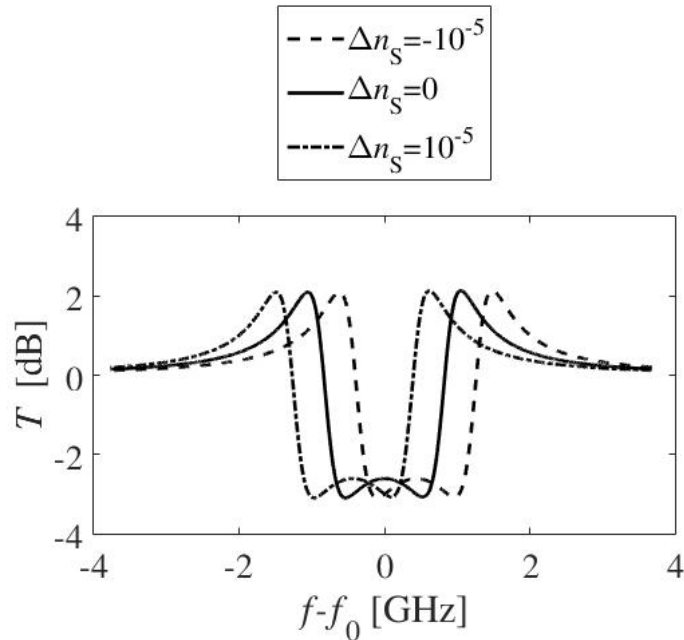


Figure 5.5: Influence of effective refractive index perturbations  $\Delta n_S$  in the power transfer function for the optimized design.

The figure illustrates that a positive  $\Delta n_S$  shifts the transfer function towards smaller frequencies while the reverse is true when  $\Delta n_S < 0$ . This behavior can be easily explained based on the condition at resonance (5.19). Perturbing the refractive index changes the value of the resonant frequency  $f_0$ . We can calculate the sensitivity of the power transfer function in terms of minute differences of the refractive indices of the straight or the curved racetrack sections  $n_S$  and  $n_C$  respectively. Considering the resonance condition (5.19), a small perturbation  $\Delta n_S$  in the former causes a resonant frequency shift  $\Delta f$  determined by:

$$\frac{\Delta f}{\Delta n_S} \cong \frac{-c\mu L}{2(n_S L + n_C \pi R)^2} \quad (5.62)$$

We can calculate the sensitivity  $s_n$  of the transmittance with respect to the refractive index sensitivity as:

$$s_n = \frac{\Delta T}{\Delta n_S} = \frac{\Delta T}{\Delta f} \frac{\Delta f}{\Delta n_S} = r_{\text{ch}} \frac{-c\mu L}{2(n_S L + n_C \pi R)^2} \quad (5.63)$$

Based on (5.63) we can calculate the sensitivity values per refractive index unit (RIU) change of  $s_n = -2.08 \times 10^5$  per RIU and  $s_n = -4.27 \times 10^5$  per RIU for the original and the optimized design respectively. The calculations carried out in this section, illustrate how our RR model can be applied for tailoring the device for various sensing applications.

## 5.4 Non-symmetric case

As stated earlier in this dissertation, racetrack resonators present an interesting alternative to implement waveguide/resonator coupling systems enabling accurate control of the power coupling. The intra-cavity reflections arising at the interfaces between the straight and the curved waveguides of the racetrack can, under certain conditions, lead to the creation of Fano-type resonances, which can be useful in a number of applications including optical sensing. In this section we present a comprehensive framework for engineering the spectral properties of these resonances. We define a set of conditions that the TF must fulfill along with suitable metrics which can be used to optimize the design, and then we show how the design parameters involved in the calculation of the TF, can be used to determine the required structural and material parameters of the device.

In the work presented in section 5.2, we have shown that the spectral properties of this device can, under certain conditions, be described by an analytical model. Based on realistic assumptions, we have shown that the amplitude  $H$  and power transfer function  $T = |H|^2$  can be described by rational functions (i.e. fraction of polynomials) of the frequency  $\omega$ . The power TF  $T(\omega)$  exhibits two peaks around the RR resonant frequency  $\omega = \omega_0$ . Under certain conditions, the variations of  $T$  around the peaks can be highly asymmetric exhibiting Fano-type behavior.

An example of such a behavior is illustrated in figure 5.6 as a function of the normalized frequency  $\Omega = S(\omega - \omega_0)$ . The TF possesses five extrema, three of which are maxima occurring at  $\Omega = \Omega_{\text{max}}^{(i)}$  and two minima at  $\Omega = \Omega_{\text{min}}^{(i)}$ . A Fano-type behavior is obtained around  $\Omega = \Omega_{\text{max}}^{(1)}$  where the TF is highly asymmetric exhibiting a sharp transition to the right (region  $A_2$ ) and a much smoother transition to the left (region  $A_1$ ). The TF is also relatively smooth in the valley region  $A_3$

between  $\Omega_{\min}^{(1)}$  and  $\Omega_{\min}^{(2)}$ . A similar situation is observed at the peak  $\Omega = \Omega_{\max}^{(3)}$ . Such a spectral behavior involving regions of low absorption followed by sharp transitions leading to smooth valleys of high absorption imply increased sensitivity of the transmittance in the intermediate range with respect to refractive index perturbations. The presence of a chemical substance (analyte) causes a change in the refractive index of the cladding of the racetrack waveguide and therefore the transmittance depends on the properties of the analyte. This is much sought after in applications such as bio-sensing [99]. Refractive index perturbations may also be due to non-linearity or the electro-optic effect which renders these devices very useful in optical gating [125] and modulation [126] applications.

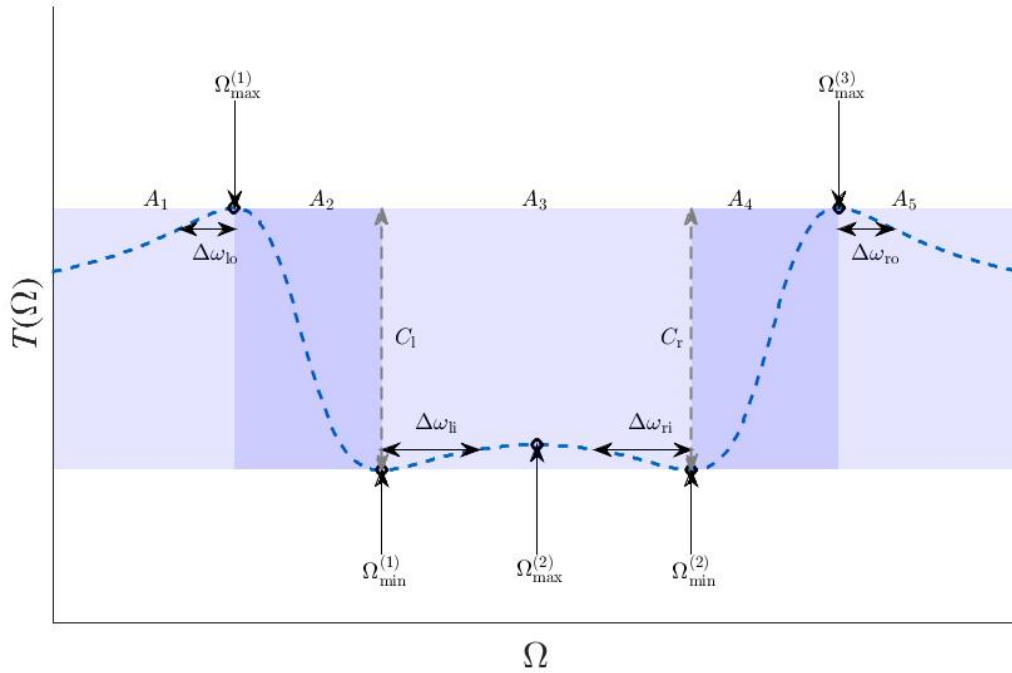


Figure 5.6: Example of a RR/waveguide system TF  $T = T(\Omega)$  which is symmetric around  $\Omega = 0$ . The TF exhibits sharp transitions in regions  $A_2$  and  $A_4$  switching from a regions of low absorption  $A_1$  and  $A_5$  to a valley of high absorption  $A_3$ .

We have also shown in section 5.3, that under certain conditions related to the phase of the cross-coupling coefficient  $g = g_r + jg_i$  between the clockwise (CW) and the counter-clockwise (CCW) wave inside the racetrack shown in figure 5.1, the TF can retain its asymmetric nature around the peaks but still be symmetric with respect to  $\Omega$ . More specifically if  $g_r = 0$  then one has  $T(\Omega) = T(-\Omega)$  (this is the case shown in figure 5.6). In this case, it is possible to calculate the position of the minima and maxima in closed form. We have used this model to tailor the properties of a symmetric  $T = T(\Omega)$  in section 5.3.1 in order for it to be suitable for sensing applications. Due to the closed form nature and the symmetry properties of the transfer function, the design process is relatively straight-forward since one simply needs to minimize the spectral distance between the maxima and minima of the transfer function in either side, e.g.  $\mathcal{M} = \Omega_{\min}^{(1)} - \Omega_{\max}^{(1)}$  and impose a condition for the contrast between the corresponding transfer function maximum  $T(\Omega_{\max}^{(1)})$  and

minimum  $T(\Omega_{\min}^{(1)})$ . This ensures that the transfer function has a sharp transition of considerable contrast to be used in sensing applications.

One expects to obtain better results, however, if one considers non-symmetric transfer functions occurring for  $g_r \neq 0$ . The general case requires special care since one is no longer aided by analytical expressions for the location of the minima and maxima of the transfer function. Hence the results presented in section 5.3 do not apply and one must come up with a different framework in order to optimize the asymmetric transfer functions. In the absence of analytical tools, one must ensure that both the metric  $\mathcal{M}$  and the set of conditions  $\mathcal{R}$  are chosen carefully in order to exclude unsuitable transfer functions, e.g. non-Fano transfer functions consisting of ultra-narrow Lorentzian-type resonances with very high gain-assisted peaks which are not useful for sensing applications where one prefers sharp transitions between otherwise smooth high and low transmittance regions as shown in figure 5.6.

In the following sections, we show how the design framework of section 5.2 can be extended to handle the asymmetric cases as well. In more detail,

- We introduce a more suitable albeit slightly more complex metric  $\mathcal{M}$  designed to handle the asymmetric transfer function case, considering the behavior of the transfer function on either side of  $\Omega = 0$ .
- We introduce an extended set of conditions  $\mathcal{R}$  that the transfer function must satisfy in order to be considered as suitable. Since most of the properties of the transfer function, including the positions of the minima and maxima can not be obtained in closed form, this set of conditions is carefully chosen so as to ensure that only meaningful designs are obtained through the optimization.
- We present an algorithm for calculating the metric  $\mathcal{M}$  taking into account  $\mathcal{R}$  that a component designer can apply to characterize each design in question.
- We clarify how the structural and material parameters are related to the optimal transfer function parameters in the general case where  $g_r \neq 0$ . We show that for a given resonance order  $\mu$  there are many possible values for the length of the straight and curved racetrack waveguide sections and the corresponding gain coefficients.
- We present the optimal designs obtained through exhaustive search on a specified parameter space. We show that the majority of these designs turn out to be asymmetric and discuss various application issues.

Applying the approximations discussed in section 5.2, it is evident that the device amplitude TF along with its spectral properties can be described by equations (5.38)-(5.42), which hold for both the symmetric case where  $g_r = 0$  and the asymmetric case  $g_r \neq 0$ , since no restriction is imposed on  $g$  in their derivation in the analysis presented in section 5.3. The round-trip gain  $G$  of equation 5.21 is alternatively given by:

$$G = e^{2g_s L + 2g_c \pi R} = G_S^2 G_C^2 \quad (5.64)$$

with  $G_S$  and  $G_C$  being the gain of a single straight and curved section respectively:

$$G_S = e^{g_S L} \quad (5.65)$$

$$G_C = e^{g_C \pi R} \quad (5.66)$$

The coefficients  $G$ ,  $G_S$  and  $G_C$  are net gain coefficients including the influence of both the active material gain and the propagation losses. Note that the round-trip gain can be adjusted with the aid of the gain tuning techniques mentioned in section 2.10, in order to compensate for excess optical loss at the waveguide.

As can be deduced from (5.39)-(5.42) there are three design parameters that completely determine the TF: the round-trip device gain  $G$ , the power coupling coefficient  $\kappa$  (or equivalently the transmission coefficient,  $\tau = 1 - \kappa$ ) and the CCW/CW coupling coefficient  $g = g_r + jg_i$ . We can therefore proceed with the design in two stages: in the first stage we estimate the required values of the three design parameters that correspond to the optimum design. This can be done through exhaustive search or by numerical optimization methods. Once the optimum design parameters are determined, then we need to translate them into structural and material parameters (radius of the curved section  $R$ , etc). This is the objective of section 5.5.

## 5.5 Relating the design and structural parameters

Before optimizing the transfer function of the device, we first need to relate the material and structural parameters of the device to the required values of the design parameters ( $G$ ,  $\kappa$ ,  $g$ ) of the transfer function. This has not been previously undertaken in the literature and is the subject of the current section.

### 5.5.1 Gain parameters

To relate the TF parameters ( $G$ ,  $\kappa$ ,  $g$ ) with the device structural and material parameters, we first use (5.12) to obtain:

$$\theta_0 = \frac{\Psi_0}{2} - \phi_0 \quad (5.67)$$

We also define  $\bar{g}$  as:

$$\bar{g} = \frac{1}{r(\sqrt{G} + 1)} (g_r + jg_i) \quad (5.68)$$

and rewrite (5.23) to read:

$$-\bar{g} = e^{j\phi_0} (e^{j2\theta_0} - 1) = e^{j\phi_0 + 2j\theta_0} - e^{j\phi_0} = e^{j\Psi_0 - j\phi_0} - e^{j\phi_0} \quad (5.69)$$

Taking into account (5.20) and (5.64) we use the transformation:

$$z = e^{j\phi_0} \quad (5.70)$$

Using (5.65), we can easily deduce that:

$$|z| = |e^{j\phi_0}| = \exp\left(-\frac{g_s L}{2}\right) = \frac{1}{\sqrt{G_s}} \quad (5.71)$$

and hence:

$$G_s = \exp(g_s L) = \frac{1}{|z|^2} \quad (5.72)$$

Using (5.70) we can rewrite (5.69) as:

$$z^2 - \bar{g}z - \frac{1}{\sqrt{G}} = 0 \quad (5.73)$$

According to (5.10),  $\phi_0$  and therefore  $z$ , depend on the length  $L$  and the gain  $g_s$  of the straight waveguide section. If the values of the reflectivity  $r$  and the TF parameters  $G$  and  $g$  are known, one can use (5.73) to obtain the values of  $\phi_0$ . The roots of this equation are:

$$z_{a,b} = \exp(j\phi_{0a,b}) = \frac{\bar{g} \pm \sqrt{\Delta}}{2} \quad (5.74)$$

where the discriminant  $\Delta$  is given by:

$$\Delta = \bar{g}^2 + \frac{4}{\sqrt{G}} \quad (5.75)$$

The roots in (5.74) correspond to two possible values  $z_{a,b} = \exp(j\phi_{0a,b})$  of  $\exp(j\phi_0)$  which in turn can be used to determine the length  $L$  and the gain coefficient  $g_s$  of the straight section. One can relate the gain of the straight section  $G_{S_a} = |z_a|^{-2}$  and  $G_{S_b} = |z_b|^{-2}$  corresponding to the two solutions, since the product of the two roots of (5.73) is readily given by:

$$z_a z_b = \frac{1}{\sqrt{G}} \quad (5.76)$$

We therefore deduce that:

$$G_{S_a} G_{S_b} = \frac{1}{|z_a|^2 |z_b|^2} = G \quad (5.77)$$

Using (5.64), we readily see that:

$$G_{S_a}^2 G_{S_b}^2 G_{C_a}^2 G_{C_b}^2 = G^2 \quad (5.78)$$

and substituting (5.77), we obtain:

$$G_{C_a} G_{C_b} = 1 \quad (5.79)$$

Equations (5.77) and (5.79) suggest that the gains of the single curved and straight section corresponding to the two solutions of (5.73) are closely related to each other. Once the necessary individual section gain values  $G_s = G_{S_a}, G_{S_b}$  and  $G_c = G_{C_a}, G_{C_b}$  are determined, we can proceed to estimate the structural and material parameters of the device.

## 5.5.2 Structural parameters

The length of the straight section is determined by the angle  $\phi_{\text{Ta,b}}$  of  $z_{\text{a,b}}$ :

$$\phi_{\text{Ta,b}} = \angle z_{\text{a,b}} \quad (5.80)$$

Since  $\exp(j\phi_{\text{Ta,b}}) = \exp(j\Re\{\phi_0\})$ , one obtains that  $\phi_0 = \phi_{\text{Ta,b}} + 2\nu\pi$  for any integer  $\nu$ . Using (5.10), we obtain:

$$\frac{n_S \omega_0 L_{\text{a,b}}}{c} = \phi_{\text{Ta,b}} + 2\nu\pi \quad (5.81)$$

Given the waveguide mode effective refractive index  $n_S$  which can be calculated using well known numerical techniques [127], [105], we can calculate the possible values of the length of the straight waveguide section,  $L_{\text{a,b}} = L_{\text{a,b}}(\nu)$  using (5.81). To calculate the radius  $R_{\text{a,b}}$  of the curved section we can use (5.12) to obtain:

$$\frac{n_C \omega_0 \pi R_{\text{a,b}}}{c} = \Re\left\{\frac{\Psi_0}{2}\right\} - \phi_{\text{Ta,b}} - 2\nu\pi = (\mu - 2\nu)\pi - \phi_{\text{Ta,b}} \quad (5.82)$$

The gain coefficients  $g_S$  and  $g_C$  of the straight and curved waveguide respectively are easily extracted through (5.65) and (5.66):

$$g_{\text{Sa,b}} = \frac{1}{L_{\text{a,b}}} \ln(G_{\text{Sa,b}}) \quad (5.83)$$

$$g_{\text{Ca,b}} = \frac{1}{\pi R_{\text{a,b}}} \ln(G_{\text{Ca,b}}) \quad (5.84)$$

To summarize, the first step in the calculation of the required structural and gain parameters  $L$ ,  $R$ ,  $g_C$  and  $g_S$  given the TF design parameters  $g$ ,  $\kappa$ ,  $G$  and a suitable value for the reflectivity  $r$ , is to calculate the parameter  $\bar{g}$  in (5.69). Next, the two roots  $z = z_a$  and  $z = z_b$  of the quadratic equation (5.73) have to be calculated. Each of the roots corresponds to sets of alternative structural parameters for the same design. The magnitude of the roots determines the required gain of the straight section  $G_{\text{Sa,b}}$  through (5.65) and the angle of the roots determines the required phase difference at the straight section through (5.80). The length of the straight section  $L_{\text{a,b}}$  is determined by (5.81). Note that there are several values  $L_{\text{a,b}} = L_{\text{a,b}}(\nu)$  that satisfy (5.81) corresponding to the different values of the integer  $\nu$ . The gain coefficient of the straight section  $g_{\text{Sa,b}} = g_{\text{Sa,b}}(\nu)$  is determined by (5.83). Subsequently, a suitable value of the order  $\mu$  has to be selected and then an estimation of the values of the curved waveguide radius  $R_{\text{a,b}} = R_{\text{a,b}}(\nu)$  and its gain coefficient  $g_{\text{Ca,b}} = g_{\text{Ca,b}}(\nu)$  through (5.82) and (5.84) respectively, can finally be extracted.

## 5.6 RR/waveguide structure design

This section presents the additional contribution of the dissertation by detailing the optimization of the transfer function  $T(\Omega)$  and presenting some useful device designs obtained by the optimization. As stated previously, the general case where  $T(\Omega)$  is not necessarily symmetric around  $\Omega = 0$  necessitates the introduction of a new metric  $\mathcal{M}$  and a new set of optimization conditions  $\mathcal{R}$ , followed by the introduction of an algorithm outlining the characterization of a specific design in

section 5.6.1. We discuss how  $\mathcal{M}$  and  $\mathcal{R}$  can be efficiently applied by further explaining this algorithm in 5.6.2. We also present the results obtained by the design framework proposed in 5.6.3, highlighting their applicability for sensing applications.

### 5.6.1 Metric and restrictions definition

In order to design a coupled RR/waveguide system we need to first identify a suitable metric  $\mathcal{M}$  which quantifies the appropriateness of the design in terms of its TF  $T(\Omega)$ . We can then either perform exhaustive search in a predefined design parameter search space  $\mathcal{S}$  or use some optimization method to identify the point in  $\mathcal{S}$  that minimizes  $\mathcal{M}$ . Given the values of  $(g, G, \kappa)$  of a point in  $\mathcal{S}$ , we calculate the TF using (5.38) inside the normalized frequency region  $\Omega \in [-10x_{\text{ext}}, 10x_{\text{ext}}]$  where  $x_{\text{ext}}$  is the far right extremum for the symmetric design ( $g_r = 0$ ) which is known in closed form. We assume a uniformly spaced 1000-point frequency grid and numerically calculate the TF. Based on the calculated values of  $T(\Omega)$ , we check whether a set of conditions  $\mathcal{R}$  are satisfied and if they are, we calculate a metric  $\mathcal{M}$  characterizing the suitability of the design. We assume that the metric is defined in such a way so that  $\mathcal{M}$  is minimized for the optimum design. Algorithm 1 summarizes the calculation of the metric  $\mathcal{M}$  insuring a suitable set of restrictions are met.

---

#### Algorithm 1 Characterization of an RR/waveguide design

---

```

1: procedure Characterize( $G, \kappa, g, C_{\min}, Q_T$ ) ▷ returns the metric  $\mathcal{M}$  of a design
2:   Calculate the TF  $T(\Omega)$  on the frequency grid based on (5.38)-(5.42).
3:   Numerically find the maxima  $\Omega_{\max}^{(i)}$  and the minima  $\Omega_{\min}^{(i)}$  of  $T(\Omega)$ .
4:   if there are three maxima and two minima and  $\Omega_{\max}^{(1)} < \Omega_{\min}^{(1)} < \Omega_{\max}^{(2)} < \Omega_{\min}^{(2)} < \Omega_{\max}^{(3)}$  then
5:     Calculate the 1 dB bandwidths  $\Delta\Omega_{\text{lo}}, \Delta\Omega_{\text{ro}}, \Delta\Omega_{\text{li}}$  and  $\Delta\Omega_{\text{ri}}$ .
6:      $Q_l \leftarrow \Delta\Omega_{\text{lo}}/\Delta\Omega_{\text{li}}, Q_r \leftarrow \Delta\Omega_{\text{ro}}/\Delta\Omega_{\text{ri}}$ .
7:     Calculate the contrast levels  $C_l$  and  $C_r$ .
8:     if  $Q_l > Q_T$  and  $C_l > C_{\min}$  then ▷ is left peak suitable?
9:        $\delta\omega_l \leftarrow \Omega_{\min}^{(1)} - \Omega_{\max}^{(1)}$ 
10:    else
11:       $\delta\omega_l \leftarrow +\infty$ 
12:    if  $Q_r > Q_T$  and  $C_r > C_{\min}$  then ▷ is right peak suitable?
13:       $\delta\omega_r \leftarrow \Omega_{\max}^{(3)} - \Omega_{\min}^{(2)}$ 
14:    else
15:       $\delta\omega_r \leftarrow +\infty$ 
16:     $\mathcal{M} \leftarrow \min \{\delta\omega_r, \delta\omega_l\}$ 
17:  else
18:     $\mathcal{M} \leftarrow +\infty$ 
19:  return  $\mathcal{M}$ 

```

---

Regarding the restrictions  $\mathcal{R}$  we impose in the design process, these relate to the contrast between the peak and the minima and the flatness of the low and high absorption regions in the

frequency ranges adjacent to each transition. We also impose the condition that the TF must have five extrema and specifically three maxima  $\Omega_{\max}^{(i)}$ ,  $i = 1, 2, 3$  with two minima  $\Omega_{\min}^{(i)}$ ,  $i = 1, 2$  in between, which is the case of the TF shown in figure 5.6 with  $\Omega_{\max}^{(1)} < \Omega_{\min}^{(1)} < \Omega_{\max}^{(2)} < \Omega_{\min}^{(2)} < \Omega_{\max}^{(3)}$ . Referring to the figure, we also define the following bandwidths:

- the 1 dB bandwidth  $\Delta\Omega_{l_0}$  to the left of  $\Omega_{\max}^{(1)}$  (frequency region  $A_1$ ).
- the 1 dB bandwidth  $\Delta\Omega_{r_0}$  to the right of  $\Omega_{\max}^{(3)}$  (frequency region  $A_5$ ).
- the 1 dB bandwidth  $\Delta\Omega_{l_i}$  to the right of  $\Omega_{\min}^{(1)}$  (frequency region  $A_3$ ).
- the 1 dB bandwidth  $\Delta\Omega_{r_i}$  to the left of  $\Omega_{\min}^{(2)}$  (frequency region  $A_3$ ).

The ratio  $Q_l = \Delta\Omega_{l_0}/\Delta\Omega_{l_i}$  measures the width of the low absorption region  $A_1$  compared to the width of the valley region  $A_3$  in figure 5.6. We have empirically verified that  $Q_l$  should be larger than  $Q_T = 0.3$ , in order to have a reasonably flat region of low absorption to the left of  $\Omega_{\max}^{(1)}$ . In the same manner, we calculate the ratio  $Q_r = \Delta\Omega_{r_0}/\Delta\Omega_{r_i}$  around the transition region  $A_4$  and check whether this is also larger than  $Q_T$ . We also calculate the contrast levels  $C_l$  and  $C_r$  of the transition regions shown in figure 5.6 as:

$$C_l = 10 \log_{10} \frac{T\left(\Omega_{\max}^{(1)}\right)}{T\left(\Omega_{\min}^{(1)}\right)} \quad (5.85)$$

$$C_r = 10 \log_{10} \frac{T\left(\Omega_{\max}^{(3)}\right)}{T\left(\Omega_{\min}^{(2)}\right)} \quad (5.86)$$

and assume a minimum contrast value  $C_{\min}$  that is deemed acceptable for the transition regions. The metric  $\mathcal{M}$  must be related to the spectral width of the transition regions which we seek to minimize in order for the designs to be suitable for sensing applications. The metric  $\mathcal{M}$  calculated by the algorithm is related to the spectral ranges of the transition regions  $A_2$  and  $A_4$  in figure 5.6 which are:

$$\delta\omega_l = \Omega_{\min}^{(1)} - \Omega_{\max}^{(1)} \quad (5.87)$$

$$\delta\omega_r = \Omega_{\max}^{(3)} - \Omega_{\min}^{(2)} \quad (5.88)$$

## 5.6.2 Design characterization

We now clarify the manner in which we calculate the conditions  $\mathcal{R}$  and the metric  $\mathcal{M}$  for a given design using algorithm 1. According to the algorithm, we calculate the values of  $T(\Omega)$  and then proceed to numerically locate the minima and the maxima. If these meet the conditions stated in line 4 of algorithm 1 then we proceed to calculate the 1 dB bandwidths around each transition region and the corresponding contrast level. If the conditions regarding the contrast and the bandwidth are met then we calculate the spectral width of the transition region  $\delta\omega_i$  otherwise we set  $\delta\omega_i = +\infty$  in which case the corresponding transition region is ignored in calculating  $\mathcal{M}$  in line 16. If both

transition regions do not meet the conditions then this will result in setting  $\mathcal{M} = +\infty$  in the same line. Also if the conditions regarding the minima and maxima positions are not satisfied in line 4, then we set  $\mathcal{M} = +\infty$  in line 18.

### 5.6.3 Results and discussion

Based on the values of  $C_{\min}$  and  $Q_T$ , the metric  $\mathcal{M}$  can be calculated for many different values of  $(G, \kappa, g)$  and the optimum design can be identified by minimizing  $\mathcal{M}$  using exhaustive search or some other optimization method. In our case, we performed exhaustive search in the four-dimensional parameter space  $(G, \kappa, g_r, g_i)$  assuming a uniform  $41 \times 51 \times 101 \times 81$  grid contained within  $1.01 \leq G \leq 1.05$ ,  $0 \leq g_r \leq 10^{-4}$ ,  $0.02 \leq g_i \leq 0.1$  and  $0.01 \leq \kappa \leq 0.06$  with corresponding grid spacing  $\Delta G = 10^{-3}$ ,  $\Delta g_r = 10^{-6}$ ,  $\Delta g_i = 10^{-3}$  and  $\Delta \kappa = 10^{-3}$ . The range of these parameters was selected so that corresponding gain values can be achieved in typical III-V materials and can be adjusted depending on the material platform considered. Given that the number of parameters to be varied is equal to four, we have chosen to carry out exhaustive search rather than more elaborate optimization methods. Exhaustive search has the advantage of being able to locate the global minima for a small number of search variables. However, if more design variables come into play as in the case of multiple coupled racetrack structures, more elaborate optimization methods [128] should be adopted, since the dimension of the search space will increase and this will render exhaustive search inefficient. The ratio  $Q_T$  was set equal to 0.3 while various values for the minimum contrast  $C_{\min}$  were assumed ranging from 7 dB to 15 dB.

Figure 5.7 shows the TFs of the optimal designs obtained using exhaustive search while table 5.3 shows the corresponding parameters of each TF. As shown in the figure, the transfer functions exhibit a typical Fano-type resonance behavior which is much desired in sensing applications. In all cases, a relatively flat frequency region of high and low transmittance is obtained for large  $|\Omega|$  and small  $|\Omega|$  respectively with very sharp transition regions in between. Depending on the required values of  $C_{\min}$  one can obtain large contrasts at the expense of a smaller valley region near  $\Omega \cong 0$ . Figure 5.8 shows the values of  $\mathcal{M} = \delta\omega$  obtained in each case. There are several interesting conclusions to be drawn from table 5.3. First of all, the majority of optimum designs for the various values of  $C_{\min}$  considered in the table have a non-zero  $g_r$ . We also note that as  $C_{\min}$  increases, a larger  $\kappa$  is needed in order to enhance the cavity/waveguide interaction. Also all designs have  $g_i = 0.02$  implying that the Fano-type behavior is favored for relative weak CCW/CW wave coupling inside the RR. Another interesting conclusion can be drawn from figure 5.8 where we see that the optimum transition region  $\mathcal{M} = \delta\omega$  varies linearly with  $C_{\min}$  expressed in dBs. This implies that the structure can be designed with transitions of larger contrast but this comes at the expense of a larger spectral width for the transition region and a smaller valley region  $A_3$ . This is evident in figure 5.7. Given the TF parameters  $(G, \kappa, g_r, g_i)$ , we calculate the possible gain coefficients and lengths for two designs of table 5.3. We apply the framework of section 5.5 to obtain these structural and material parameters for each design. Figure 5.9a shows the TF obtained from the optimization process as a function of the frequency detuning  $\Delta f = f - f_0$  from the central resonant frequency  $f_0 = 193.55\text{THz}$  corresponding to a free-space wavelength

$\lambda_0 = 1.55\mu\text{m}$ , assuming a resonance order  $\mu = 686$  and a reflectivity coefficient  $r = -20$  dB. For the purposes of our design, typical refractive index values  $n_S = 3.6$  and  $n_C = 3.5$  for III-V materials (e.g. AlGaInAs or InGaAsP) were used [129], [130]. The half width half max for our design was calculated 0.4362 GHz for the first peak and 0.4216 GHz for the second peak.

$C_{\min}$	$\kappa$	$G$	$g_i$	$g_r$
7 dB	0.025	1.011	0.020	$8.1 \times 10^{-5}$
8 dB	0.029	1.015	0.020	$5.2 \times 10^{-5}$
9 dB	0.029	1.012	0.020	$9.3 \times 10^{-5}$
10 dB	0.032	1.014	0.020	0.0
11 dB	0.033	1.014	0.020	$1.6 \times 10^{-5}$
12 dB	0.034	1.014	0.020	$6.8 \times 10^{-5}$
13 dB	0.035	1.014	0.020	0.0
14 dB	0.036	1.014	0.020	$3.9 \times 10^{-5}$
15 dB	0.036	1.013	0.020	$9.4 \times 10^{-5}$

Table 5.3: Optimal TF parameters

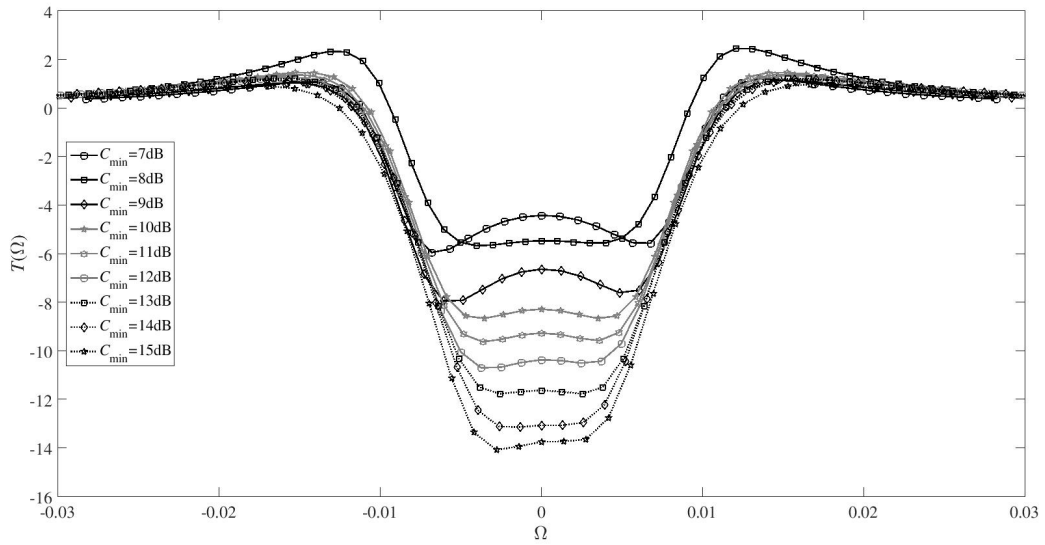


Figure 5.7: Optimized TFs obtained through exhaustive search and for various values of  $C_{\min}$ . The corresponding design parameters are included in Table 5.3.

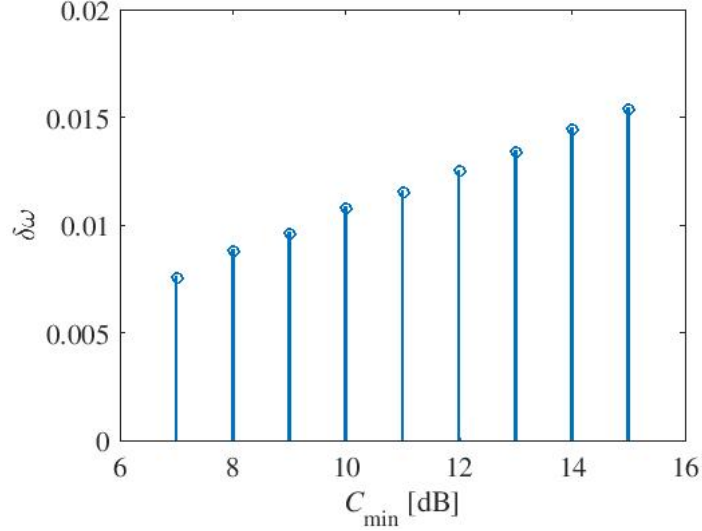


Figure 5.8: Values of  $\mathcal{M} = \delta\omega$  obtained for the various values of  $C_{\min}$ .

Figure 5.9b shows the values of the length  $L_{a,b} = L_{a,b}(\nu)$  and the radius  $R_{a,b} = R_{a,b}(\nu)$  obtained by (5.81) and (5.82) while figure 5.9c shows the values of the gain coefficients  $g_{S_{a,b}} = g_{S_{a,b}}(\nu)$  and  $g_{C_{a,b}} = g_{C_{a,b}}(\nu)$  of the straight and curved sections of the RR, calculated by (5.72) and (5.64). As discussed in section 5.5, we have to account for the two roots  $z = z_a$  and  $z = z_b$  of (5.73) which lead to two sets of values for each parameter designated by the subscripts "a" and "b" in the figures. It is interesting to note that for each integer  $\nu$ , the lengths  $L_a$  and  $L_b$  are approximately equal  $L_a \cong L_b$  and this holds for the radii  $R_a$  and  $R_b$  as well. This is because, according to (5.81), the lengths  $L_a = L_a(\nu)$  and  $L_b = L_b(\nu)$  differ only in the values of the phase  $\phi_{T_{a,b}}$  of  $z_{a,b}$  which lies inside  $[-\pi, \pi]$ . As  $\nu$  increases one has  $2\nu\pi \gg \phi_{T_{a,b}}$  and hence  $L_a \cong L_b$ . This is also the case for  $R_a$  and  $R_b$ . Another interesting conclusion is that  $L_{a,b}$  is increasing with  $\nu$  while  $R_{a,b}$  is decreasing. This is also evident in (5.81) and (5.82) and is due to the fact that the round-trip phase difference at resonance,  $\Re\{\Psi_0\}$ , is kept constant and equal to  $2\mu\pi$ . The gain coefficients in figure 5.9c are also of interest: the first root (black lines) corresponds to an active curved section ( $g_{C_a} > 0$ ) and a straight waveguide section with very small gain  $g_{S_a} \cong 0$ . The other root corresponds to an active straight waveguide section  $g_{S_b} > 0$  and a passive curved section  $g_{C_b} < 0$ . The figure illustrates the manner in which the gain parameters must be chosen accordingly in order to achieve the desired Fano-type behavior in the transition regions.

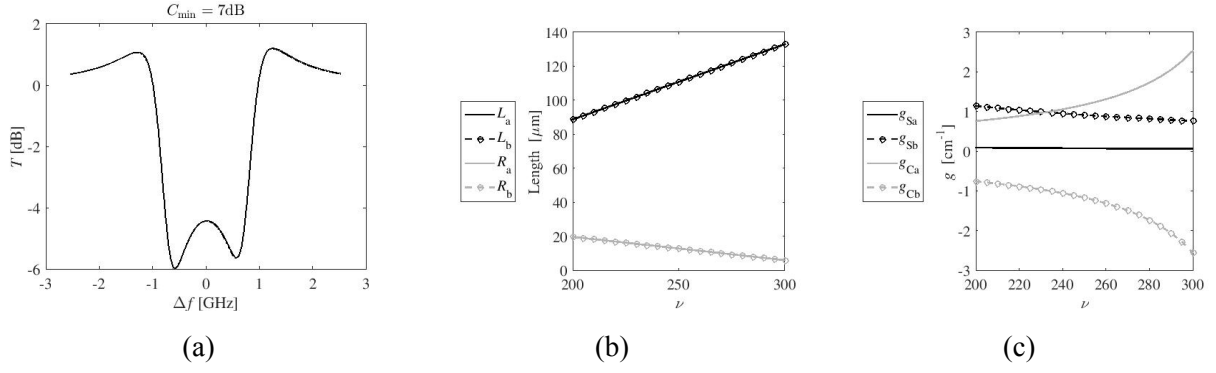


Figure 5.9: Design obtained for  $C_{\min} = 7$  dB: a) the TF in terms of the frequency detuning  $\Delta f$  from the resonant frequency, b) the lengths of the straight and the radii of the curved section corresponding to the two roots of (5.73) and c) the gain coefficients corresponding to the roots.

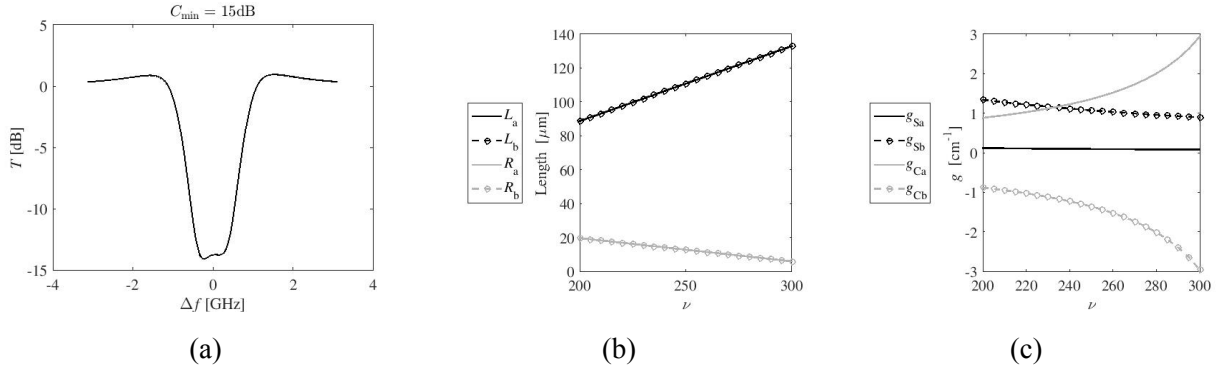


Figure 5.10: Design obtained for  $C_{\min} = 15$  dB: a) the TF in terms of the frequency detuning  $\Delta f$  from the resonant frequency, b) the lengths of the straight and the radii of the curved section corresponding to the two roots of (5.73) and c) the gain coefficients corresponding to the roots.

Similar conclusions can be drawn for the case where  $C_{\min}$  is chosen equal to 15 dB, where the half width half max is 0.8917 GHz for the first peak and 0.8735 GHz for the second peak. The waveguide lengths for the two roots are again approximately equal and similar to the case of  $C_{\min} = 7$  dB, since only the phase  $\phi_T$  is different. The gain coefficients exhibit a similar behavior as well but their values are somewhat different. This opens up an interesting possibility of being able to fine-tune the TF properties of the RR/waveguide system by changing the values of the gain coefficients and achieving higher contrast at the expense of a smaller valley region  $A_3$ .

It is useful to quantify the effect of small refractive index perturbations on the power transfer function. Assume that the value of the refractive index  $n_S$  is perturbed by  $\Delta n_S$  then this causes a frequency shift on the resonant frequency  $f_0 = \omega_0/(2\pi)$  determined by (5.12). In figure 5.11 we demonstrate how a small change in the refractive index of  $\Delta n_S = \pm 10^{-5}$ , shifts the transfer function, because of this resonant frequency detuning. In section 5.3.1, we have shown that the frequency shift  $\Delta f$  is determined by,

$$s_f = \frac{\Delta f}{\Delta n_S} \approx \frac{-c\mu L}{2(n_S L + n_C \pi R)^2} \quad (5.89)$$

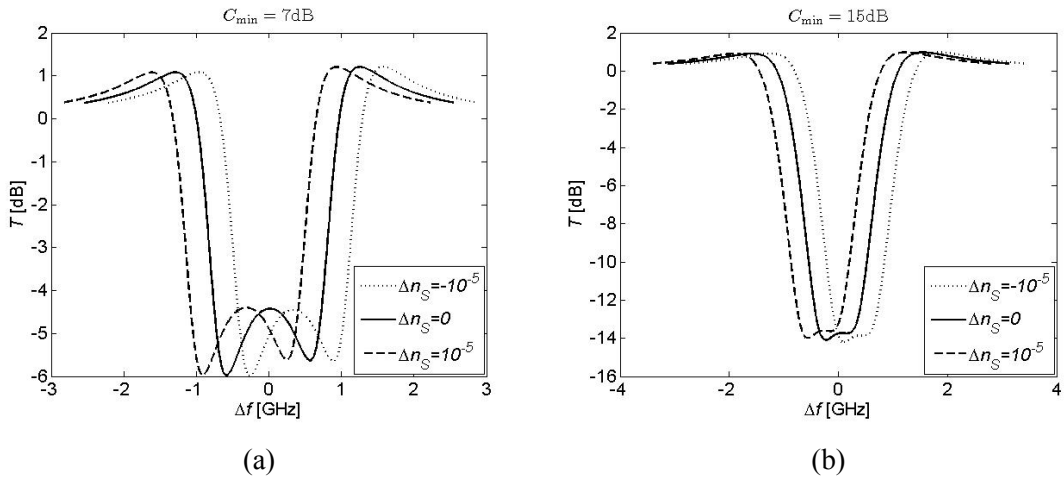


Figure 5.11: The effect of the effective index perturbations  $\Delta n_S$  in the power transfer function for: a)  $C_{\min} = 7\text{dB}$  and b)  $C_{\min} = 15\text{dB}$ .

At the transition regions  $A_2$  and  $A_4$  in figure 5.6, the transfer function has a contrast equal to  $C_1$  and  $C_r$  respectively while the size of the transition region is  $\delta\omega_1/(2\pi)$  and  $\delta\omega_r/(2\pi)$  respectively. The transmittance rate of change with respect to frequency is therefore  $s_1 = 2\pi C_1/\delta\omega_1$  and  $s_r = 2\pi C_r/\delta\omega_r$  in  $A_2$  and  $A_4$  respectively. The sensitivities of the transmittance with respect to the change in the refractive index are calculated as  $S_1 = s_1 s_f$  and  $S_r = s_r s_f$ . Table 5.4 summarizes the transmittance sensitivity for the designs of figure 5.11 as well as the lengths and the gain coefficients of the racetrack sections assumed. The length  $L$  of the straight section was chosen from the possible values of figures 5.9b and 5.10b so that it is the closest to  $100\mu\text{m}$ . We have also chosen the corresponding gain coefficients from figures 5.9c and 5.10c so that both sections are active ( $g_S > 0$ ,  $g_C > 0$ ). The table quotes the sensitivity values  $S_1$  for region  $A_2$  since in both designs this transition region had the largest contrast. The obtained  $S_1$  values are both in the order of  $10^5$  dB/RIU which suggests that such structures can indeed be used in sensing applications due to their high sensitivity in refractive index changes. Such high sensitivity values also imply that the structures can be used in signal processing applications based on the non-linear Kerr effect.

$C_{\min}$	$L[\mu\text{m}]$	$R[\mu\text{m}]$	$g_S[\text{cm}^{-1}]$	$g_C[\text{cm}^{-1}]$	$s_f[\text{THz}/\text{RIU}]$	$S_1[\text{dB}/\text{RIU}]$
7	100.1	16.0	0.079	0.929	36.44	$3.78 \times 10^5$
15	100.1	16.0	0.103	1.078	36.44	$3.96 \times 10^5$

Table 5.4: Transfer function sensitivity

We should note that the manner in which these parameters are chosen in table 5.4 is by no means optimal and different values of  $L$  could achieve better sensitivities. We have verified that choosing a different target for  $L$  say  $50\mu\text{m}$  did not change the order of magnitude for  $S_1$ .

## 5.7 Conclusions

In the previous sections, an analytical model that can be used in order to calculate the spectral properties of an active coupled racetrack/waveguide system was demonstrated in detail. The model takes into account intra-cavity reflections that can provide additional degree of freedom for tailoring the spectral response of the device. We have shown that the transfer function can be accurately described by a rational transfer function, the coefficients of which directly depend on the parameters of the structure. We further discussed the applicability of the model in tailoring of Fano-like resonances for various applications for both the symmetric and non-symmetric case. In the symmetric case, we presented the optimal design, calculated after an exhaustive search was performed, inside the parameter's range imposed by the restrictions that have to apply in the design process of such a device. In the non-symmetric case, we have shown how one can obtain different types of TFs with different contrast levels and spectral widths in the transition regions between low and high transmittance. We have also related the design parameters determining the TF to the structural and material parameters of the device. The design process can be achieved by an exhaustive search sweeping in the design parameter space. We have identified a suitable metric  $\mathcal{M}$  and a set of restrictions  $\mathcal{R}$  that can be used in order to quantify the suitability of any given design encountered in the search space. We have presented examples of suitable designs along with their design and structural parameters.

Our results for both cases, can serve as a guide for the realization of compact optical sensors based on RR/waveguide coupling and can be also interesting for other applications that demand sharp spectral transitions between regions of high and low transmittance such as optical modulation and signal processing. As a final note, we mention that it is also very interesting to extend the analytical transfer function model and design framework in order to investigate the incorporation of multiple racetrack cavities and/or multiple bus waveguides in order to obtain better performance. This could be the subject of further research.

## 6 Conclusions and outlook

The final chapter of this thesis, summarizes the main results of our research work and provides some ideas for possible extension of the work in new domains of photonics.

### 6.1 Contribution of this thesis

This thesis mainly focused on the design problem of figure 1.1b, i.e. finding the optimum values for both structural and material parameters taking into account possible constraints imposed by the device implementation methods. Towards this end, we applied optimization methods and efficient numerical simulation tools based on the coupled-mode theoretic framework. The main contribution of this thesis to the existing state-of-the-art is outlined as follows:

- In the work presented in chapter 4, we analyzed a new approach for tailoring the spectral properties of coupled micro-ring resonator optical filters using numerical optimization methods. By allowing the micro-rings to have different radii, we showed that considerably lesser crosstalk levels in a wide frequency region can be obtained, unlike the uniform ring case commonly found in literature, where the stop-band is limited by the periodic nature of the transfer function. We proved that a variation of the coupled-mode approach can be applied, for efficiently calculating the transfer function at each optimization step, scalable to an arbitrary number of rings. Using standard optimization methods, transfer functions with relatively flat pass-band and small cross-talk have been obtained for various ring numbers. Our technique may open up new paths for designing and implementing compact optical filters with pre-defined requirements on their spectral properties. This work was published in **L. Dogkas, T. Kamalakis, P. Kanakis, and D. Alexandropoulos, “Engineering the spectral properties of non-uniform coupled micro-ring resonator optical filters using numerical optimization,” *Journal of Optics*, vol. 19, no. 6, p. 065703, 2017.**
- Having completed the multi-MR design optimization method, we focused on RRs because of the unique characteristics they present in the sensing field. The first outcome of this effort was analyzed in chapter 5 and published in **L. Dogkas, T. Kamalakis, and D. Alexandropoulos, “Analytical model for active racetrack resonators with intracavity reflections and its application in Fano resonance tailoring,” *Applied Optics*, vol. 57, no. 17, pp. 4824–4831, 2018,** where we presented an analytical model for estimating the spectral properties of an active racetrack resonator/waveguide system. Under reasonable approximations, we have proved that the transfer function can be approximated by a rational function, the coefficients of which are determined by the parameters of the structure. Our model takes into account intra-cavity reflections which can provide additional degrees of freedom in the design. We also identified the conditions under which asymmetric transitions around a spectral peak can occur which are characteristic of Fano-type resonances. The accuracy of our model is verified by rigorous transfer matrix numerical simulations. We also suggested that

this model can be applied for tailoring the transfer function in order to obtain sharper transitions from the spectral peaks to the minima in order for the structure to be used for sensing applications.

- Subsequently, in the rest of chapter 5, we also presented a comprehensive framework for engineering the spectral properties of the Fano-type resonances in a RR system. Suitable metrics can be used to optimize the design were identified along with a set of conditions that the transfer function must fulfill, from an application point-of-view. We showed how the parameters involved in the transfer function calculation, can be used to determine the required structural and material parameters of the structure and provide examples of structure designs that possess favorable spectral characteristics. The findings were published in **L. Dogkas, T. Kamalakis, and D. Alexandropoulos, “Engineering the spectral properties of fano-type resonances in active racetrack-waveguide coupled structures,” *Optics Communications*, vol. 450, pp. 39–47, 2019.**

In order to validate our conditional optimization research, MATLAB’s optimization tool, was intensively utilized in order to minimize the performance metric set in the beginning of the design process, taking into consideration any restrictions imposed. The non-linear constrained minimization algorithm used by the tool, is the interior-point algorithm which solves non linear problems by traversing the interior of the feasible region and finally finds the best solution.

The methods we developed can in general be applied in order to solve almost any design problem, given that a tractable device/system model exists and suitable performance metrics can be identified along with a list of constraints which are usually derived through intuition and trial-and-error.

## 6.2 Outlook

In this section we point out some possible areas of photonics where our work can be extended.

The main characteristic of the periodic optical nano-structure called photonic crystal, is that it can affect the motion of photons in a similar way to the one that ionic lattices affect electrons in solids [131]. Photonic crystals exist in nature in the form of structural coloration and animal reflectors (opal changing color, patterns on butterfly wings etc). They compose of periodic dielectric, metallo-dielectric or even superconductor micro-structures or nano-structures that have a major effect in electromagnetic wave propagation [132]. They contain regularly repeating regions of higher and lower dielectric constant. As a consequence, some photons propagate through this structure (modes) and some do not (band gaps), depending on their wavelength [133]. This feature, can be exploited in order to discover various applications which include spontaneous emission, high-reflecting omni-directional mirrors, Fabry-Perot cavities, optical filters and distributed feedback lasers [134]. Using appropriate mathematical models in combination with a suitable minimization metric, our method could be utilized in order to obtain the optimum photonic crystal characteristics which would lead to the implementation of unique devices, appropriate for filtering and other

applications. The challenge here is to identify accurate models for photonic crystals that can be applied in the optimization schemes. Efficient block conjugate gradient algorithms can be used in combination with plane wave expansion [135] to calculate the modal fields and dispersion properties of bulk photonic crystals, while interior point Jacobi/Davidson methods can also speed-up estimation in the case of photonic crystal waveguides [136]. As a result, there is high hope of applying optimization methods in order to tailor the loss and dispersion properties of such devices. Preliminary work indicates that this is indeed feasible [137] for limited degrees of freedom, i.e. assuming only a small set of parameters of the crystal that can change. It is interesting to investigate the optimal photonic crystal design extending the search space to find the optimal photonic crystal building cell.

Additionally, structures such as photonic crystal waveguides, may possess remarkable properties including slow light propagation. The term "slow light" represents a dramatic reduction in the group velocity of light, which originates from the way in which the refractive index of a material changes with frequency. If the refractive index changes rapidly over a small range of frequencies, then the group velocity might become very low [138]. Many mechanisms which can generate slow light exist, all of which lead to the aforementioned procedure, i.e. create narrow spectral regions with high dispersion. These mechanisms can be grouped into two major categories: material dispersion and waveguide dispersion. The first mechanism involves the modification of the temporal component of a propagating wave, by using a nonlinear effect to modify the dipole response of a medium to a signal or "probe" field. Some examples of this procedure include electromagnetically induced transparency, coherent population oscillation, and various four-wave mixing (FWM) schemes [139]. The other mechanism involves the modification of the spatial component ( $k$ -vector) of a propagating wave. This can be met in photonic crystals, coupled resonator optical waveguides, and other micro-resonator structures. Slow light could be used as a means to control optical switches or even used in interferometers that are far more sensitive to frequency shift as compared to conventional interferometers, which is a property that can be used to build better, smaller frequency sensors and compact high resolution spectrometers [140]. The methods could be adjusted to facilitate the designing process of such devices. The key problem here is to maintain the desirable properties of slow light such as the slow group velocity that can be used for photonic buffering applications and non-linearity enhancement while at the same time reducing optical losses which are also enhanced due to slow light to an acceptable level [141]. This is an important task, since slow light devices are typically highly lossy and this prohibits their commercialization. Reducing the optical losses using proper device design can pave the way for a new generation of highly functional slow light devices [142].

In 2004 the attention of researchers turned towards two-dimensional semiconductors, which are natural semiconductors with thicknesses on the atomic scale. The cause of this turn was the discovery of a new semiconducting material called "graphene" [143]. Graphene can be described as a flat monolayer of carbon atoms arranged in a 2D lattice which very much reassembles a honeycomb [144]. It was then proved that a 2D monolayer semiconductor exhibits stronger piezoelectric coupling than traditionally employed bulk forms, which in turn enables and encourages the testing of 2D materials applications in new electronic components used for sensing and actuating [145],

[146]. Our method could be utilized in order to design a sensing device made of graphene, which will demonstrate optimum characteristics, given that an appropriate mathematical models in combination with a suitable minimization metric is used.

The last few years the development of photonics reservoir computing (PRC) has proved to be a suitable candidate technology in the field of machine learning. The reason for this is related to its ability to perform typical tasks of artificial neural-networks which include pattern generation, emulation of simple boolean operations, bit-sequences or chaotic time series prediction, detection of epileptic seizures, speech recognition, robot localization and more. Different technologies of photonic implementations have been proposed. The most popular of them are namely a single nonlinear node with delayed feedback such as optoelectronic oscillators and laser diode with optical feedback, integrated photonic reservoirs using passive nodes made of delay lines and splitters, coupled photonic crystal cavities, networks of semiconductor optical amplifiers and networks of InGaAsP/InP-based ring resonators [147]. Recently, a novel photonics architecture of reservoir computing integrated on a silicon chip, using silicon-on-insulator MRs as nonlinear nodes, has been presented. In order to tune the reservoir dynamics into an appropriate regime for the task at hand, only a few global parameters, such as the overall gain in the system, the magnitude of the inputs, and the network size have to be optimized [148]. Our method can be utilized in an effort to achieve this task.

### **6.3 Thesis publications**

The following publications have been carried out within this dissertation:

- **L.Dogkas, T. Kamalakis, P. Kanakis, and D. Alexandropoulos, “Engineering the spectral properties of non-uniform coupled micro-ring resonator optical filters using numerical optimization,” *Journal of Optics*, vol. 19, no. 6, p. 065703, 2017**
- **L. Dogkas, T. Kamalakis, and D. Alexandropoulos, “Analytical model for active race-track resonators with intracavity reflections and its application in Fano resonance tailoring,” *Applied Optics*, vol. 57, no. 17, pp. 4824–4831, 2018**
- **L. Dogkas, T. Kamalakis, and D. Alexandropoulos, “Engineering the spectral properties of fano-type resonances in active racetrack-waveguide coupled structures,” *Optics Communications*, vol. 450, pp. 39–47, 2019**

## References

- [1] R. Ramaswami, K. Sivarajan, and G. Sasaki, *Optical networks: a practical perspective*. Morgan Kaufmann, 2009.
- [2] “standing.” [https://www.rp-photonics.com/optical\\_resonators.html](https://www.rp-photonics.com/optical_resonators.html). Accessed: 2019-06-20.
- [3] D. Liang, X. Huang, G. Kurczveil, M. Fiorentino, and R. Beausoleil, “Integrated finely tunable microring laser on silicon,” *Nature Photonics*, vol. 10, no. 11, p. 719, 2016.
- [4] A. Arbabi, S. M. Kamali, E. Arbabi, B. G. Griffin, and L. L. Goddard, “Grating integrated single mode microring laser,” *Optics express*, vol. 23, no. 4, pp. 5335–5347, 2015.
- [5] A. Godbole, P. P. Dali, V. Janyani, T. Tanabe, and G. Singh, “All optical scalable logic gates using si 3 n 4 microring resonators,” *IEEE Journal of Selected Topics in Quantum Electronics*, vol. 22, no. 6, pp. 326–333, 2016.
- [6] Q. Xu, S. Manipatruni, B. Schmidt, J. Shakya, and M. Lipson, “12.5 gbit/s carrier-injection-based silicon micro-ring silicon modulators,” *Optics express*, vol. 15, no. 2, pp. 430–436, 2007.
- [7] A. Roshan-Zamir, B. Wang, S. Telaprolu, K. Yu, C. Li, M. A. Seyedi, M. Fiorentino, R. Beausoleil, and S. Palermo, “A 40 gb/s pam4 silicon microring resonator modulator transmitter in 65nm cmos,” in *IEEE Optical Interconnects Conference (OI), 2016*, pp. 8–9, IEEE, 2016.
- [8] A. M. Prabhu, V. Van, W. N. Herman, and P.-T. Ho, “Compact silicon microring-assisted directional couplers for wdm and optical signal processing applications,” in *Optical Fiber Communication-includes post deadline papers, 2009. OFC 2009. Conference on*, pp. 1–3, IEEE, 2009.
- [9] W. S. Fegadolli, L. Feng, M. M.-U. Rahman, J. E. Oliveira, V. R. Almeida, and A. Scherer, “Experimental demonstration of a reconfigurable silicon thermo-optical device based on spectral tuning of ring resonators for optical signal processing,” *Optics express*, vol. 22, no. 3, pp. 3425–3431, 2014.
- [10] H. Jung, M. Poot, and H. X. Tang, “In-resonator variation of waveguide cross-sections for dispersion control of aluminum nitride micro-rings,” *Optics express*, vol. 23, no. 24, pp. 30634–30640, 2015.
- [11] “2017 integrated photonic systems roadmap.” <http://photonicsmanufacturing.org/>. Accessed: 2019-03-20.
- [12] B. E. Little, S. T. Chu, H. A. Haus, J. Foresi, and J.-P. Laine, “Microring resonator channel dropping filters,” *Journal of lightwave technology*, vol. 15, no. 6, pp. 998–1005, 1997.

- [13] V. Cisco, “Cisco visual networking index: Forecast and trends, 2017–2022,” *White Paper*, 2018.
- [14] M. Saruwatari, N. Grote, and H. Venghaus, “Fiber optic communication devices,” 2001.
- [15] G. P. Agrawal, *Fiber-optic communication systems*, vol. 222. John Wiley & Sons, 2012.
- [16] P. E. Green, *Fiber optic networks*, vol. 992. Prentice Hall Englewood Cliffs, NJ, 1993.
- [17] G. Papen, “Optical components for datacenters,” in *Optical Fiber Communication Conference*, pp. M3K–1, Optical Society of America, 2017.
- [18] H. J. Dutton, “Understanding optical communications (international technical support organization),” 1998.
- [19] S. V. Kartalopoulos, *DWDM: networks, devices, and technology*. IEEE Press Wiley, 2003.
- [20] “Optical add/drop multiplexers information.” [https://www.globalspec.com/learnmore/optics\\_optical\\_components/fiber\\_optics/optical\\_adddrop\\_multiplexers](https://www.globalspec.com/learnmore/optics_optical_components/fiber_optics/optical_adddrop_multiplexers). Accessed: 2019-03-20.
- [21] “Optical add/drop multiplexing architecture for metro area networks.” <http://spie.org/newsroom/0950-optical-add-drop-multiplexing-architecture-for-metro-area-networks?ArticleID=x19262&SSO=1>. Accessed: 2019-03-20.
- [22] X. Fan, I. M. White, H. Zhu, J. D. Suter, and H. Oveys, “Overview of novel integrated optical ring resonator bio/chemical sensors,” in *Laser Resonators and Beam Control IX*, vol. 6452, p. 64520M, International Society for Optics and Photonics, 2007.
- [23] J. Homola, “Surface plasmon resonance sensors for detection of chemical and biological species,” *Chemical reviews*, vol. 108, no. 2, pp. 462–493, 2008.
- [24] V. Passaro, C. Tullio, B. Troia, M. Notte, G. Giannoccaro, and F. Leonardis, “Recent advances in integrated photonic sensors,” *Sensors*, vol. 12, no. 11, pp. 15558–15598, 2012.
- [25] “Types of optical sensors.” <https://sciencing.com/types-optical-sensors-5454698.html>. Accessed: 2019-03-20.
- [26] K. B. Gylfason, C. F. Carlborg, A. Kazmierczak, F. Dortu, H. Sohlström, L. Vivien, G. Ronan, C. A. Barrios, W. v. d. Wijngaart, and G. Stemme, “A packaged optical slot-waveguide ring resonator sensor array for multiplex assays in labs-on-chip,” in *13th International Conference on Miniaturized Systems for Chemistry and Life Sciences, MicroTAS 2009, Jeju, South Korea, 1 November 2009 through 5 November 2009*, pp. 2004–2006, Chemical and Biological Microsystems Society, 2009.

- [27] A. Yalcin, K. C. Papat, J. C. Aldridge, T. A. Desai, J. Hryniewicz, N. Chbouki, B. E. Little, O. King, V. Van, S. Chu, *et al.*, “Optical sensing of biomolecules using microring resonators,” *IEEE Journal of Selected Topics in Quantum Electronics*, vol. 12, no. 1, pp. 148–155, 2006.
- [28] H. Sohlström, K. B. Gylfason, and D. Hill, “Real-time label-free biosensing with integrated planar waveguide ring resonators,” in *Silicon Photonics and Photonic Integrated Circuits II*, vol. 7719, p. 77190B, International Society for Optics and Photonics, 2010.
- [29] “iupac.” <https://iupac.org/>. Accessed: 2019-06-20.
- [30] B. Zeng, Y. Gao, and F. J. Bartoli, “Rapid and highly sensitive detection using fano resonances in ultrathin plasmonic nan gratings,” *Applied Physics Letters*, vol. 105, no. 16, p. 161106, 2014.
- [31] H. Yi, D. Citrin, and Z. Zhou, “Highly sensitive silicon microring sensor with sharp asymmetrical resonance,” *Optics Express*, vol. 18, no. 3, pp. 2967–2972, 2010.
- [32] C. Li, S. Li, Y. Wang, R. Jiao, L. Wang, and L. Yu, “Multiple fano resonances based on plasmonic resonator system with end-coupled cavities for high-performance nanosensor,” *IEEE Photonics Journal*, vol. 9, no. 6, pp. 1–9, 2017.
- [33] C.-Y. Chao and L. J. Guo, “Biochemical sensors based on polymer microrings with sharp asymmetrical resonance,” *Applied Physics Letters*, vol. 83, no. 8, pp. 1527–1529, 2003.
- [34] X. Zhou, L. Zhang, A. M. Armani, D. Zhang, X. Duan, J. Liu, H. Zhang, and W. Pang, “On-chip biological and chemical sensing with reversed fano lineshape enabled by embedded microring resonators,” *IEEE Journal of Selected Topics in Quantum Electronics*, vol. 20, no. 3, pp. 35–44, 2014.
- [35] S. Bogdanov, M. Shalaginov, A. Boltasseva, and V. M. Shalaev, “Material platforms for integrated quantum photonics,” *Optical Materials Express*, vol. 7, no. 1, pp. 111–132, 2017.
- [36] A. Politi, J. C. Matthews, M. G. Thompson, and J. L. O’Brien, “Integrated quantum photonics,” *IEEE Journal of Selected Topics in Quantum Electronics*, vol. 15, no. 6, pp. 1673–1684, 2009.
- [37] A. Politi, M. J. Cryan, J. G. Rarity, S. Yu, and J. L. O’Brien, “Silica-on-silicon waveguide quantum circuits,” *Science*, vol. 320, no. 5876, pp. 646–649, 2008.
- [38] G. Masada, K. Miyata, A. Politi, T. Hashimoto, J. L. O’Brien, and A. Furusawa, “Continuous-variable entanglement on a chip,” *Nature Photonics*, vol. 9, no. 5, p. 316, 2015.
- [39] B. J. Metcalf, J. B. Spring, P. C. Humphreys, N. Thomas-Peter, M. Barbieri, W. S. Kolthammer, X.-M. Jin, N. K. Langford, D. Kundys, J. C. Gates, *et al.*, “Quantum teleportation on a photonic chip,” *Nature photonics*, vol. 8, no. 10, p. 770, 2014.

- [40] J. W. Silverstone, D. Bonneau, J. L. O'Brien, and M. G. Thompson, "Silicon quantum photonics," *IEEE Journal of Selected Topics in Quantum Electronics*, vol. 22, no. 6, pp. 390–402, 2016.
- [41] C. M. Gentry, J. M. Shainline, M. T. Wade, M. J. Stevens, S. D. Dyer, X. Zeng, F. Pavanello, T. Gerrits, S. W. Nam, R. P. Mirin, *et al.*, "Quantum-correlated photon pairs generated in a commercial 45 nm complementary metal-oxide semiconductor microelectronic chip," *Optica*, vol. 2, no. 12, pp. 1065–1071, 2015.
- [42] L. Pavesi, D. J. Lockwood, *et al.*, "Silicon photonics iii," *Topics in applied physics*, vol. 119, 2016.
- [43] K. Yamada, "Photonic integration and photonics–electronics convergence on silicon platform," *Frontiers in Materials*, vol. 2, p. 65, 2015.
- [44] M. Glick, L. C. Kimmerling, and R. C. Pfahl, "A roadmap for integrated photonics," *Opt. Photon. News*, vol. 29, pp. 36–41, Mar 2018.
- [45] X.-C. Yao, T.-X. Wang, H.-Z. Chen, W.-B. Gao, A. G. Fowler, R. Raussendorf, Z.-B. Chen, N.-L. Liu, C.-Y. Lu, Y.-J. Deng, *et al.*, "Experimental demonstration of topological error correction," *Nature*, vol. 482, no. 7386, p. 489, 2012.
- [46] F. Boitier, A. Orioux, C. Autebert, A. Lemaître, E. Galopin, C. Manquest, C. Sirtori, I. Favero, G. Leo, and S. Ducci, "Electrically injected photon-pair source at room temperature," *Physical review letters*, vol. 112, no. 18, p. 183901, 2014.
- [47] C. P. Dietrich, A. Fiore, M. G. Thompson, M. Kamp, and S. Höfling, "Gaas integrated quantum photonics: Towards compact and multi-functional quantum photonic integrated circuits," *Laser & Photonics Reviews*, vol. 10, no. 6, pp. 870–894, 2016.
- [48] J. Wang, A. Santamato, P. Jiang, D. Bonneau, E. Engin, J. W. Silverstone, M. Lermer, J. Beetz, M. Kamp, S. Höfling, *et al.*, "Gallium arsenide (gaas) quantum photonic waveguide circuits," *Optics Communications*, vol. 327, pp. 49–55, 2014.
- [49] J. Sprengers, A. Gaggero, D. Sahin, S. Jahanmirinejad, G. Frucci, F. Mattioli, R. Leoni, J. Beetz, M. Lermer, M. Kamp, *et al.*, "Waveguide superconducting single-photon detectors for integrated quantum photonic circuits," *Applied Physics Letters*, vol. 99, no. 18, p. 181110, 2011.
- [50] G. Reithmaier, M. Kaniber, F. Flassig, S. Lichtmannecker, K. Müller, A. Andrejew, J. Vuckovic, R. Gross, and J. Finley, "On-chip generation, routing, and detection of resonance fluorescence," *Nano letters*, vol. 15, no. 8, pp. 5208–5213, 2015.
- [51] M.-C. Oh, W.-S. Chu, J.-S. Shin, J.-W. Kim, K.-J. Kim, J.-K. Seo, H.-K. Lee, Y.-O. Noh, and H.-J. Lee, "Polymeric optical waveguide devices exploiting special properties of polymer materials," *Optics Communications*, vol. 362, pp. 3–12, 2016.

- [52] M.-C. Oh, K.-J. Kim, W.-S. Chu, J.-W. Kim, J.-K. Seo, Y.-O. Noh, and H.-J. Lee, “Integrated photonic devices incorporating low-loss fluorinated polymer materials,” *Polymers*, vol. 3, no. 3, pp. 975–997, 2011.
- [53] W. Groh, “Overtone absorption in macromolecules for polymer optical fibers,” *Die Makromolekulare Chemie: Macromolecular Chemistry and Physics*, vol. 189, no. 12, pp. 2861–2874, 1988.
- [54] A. Yeniay, R. Gao, K. Takayama, R. Gao, and A. F. Garito, “Ultra-low-loss polymer waveguides,” *Journal of lightwave technology*, vol. 22, no. 1, pp. 154–158, 2004.
- [55] P. Rath, S. Ummethala, C. Nebel, and W. H. Pernice, “Diamond as a material for monolithically integrated optical and optomechanical devices,” *physica status solidi (a)*, vol. 212, no. 11, pp. 2385–2399, 2015.
- [56] T. Schröder, S. L. Mouradian, J. Zheng, M. E. Trusheim, M. Walsh, E. H. Chen, L. Li, I. Bayn, and D. Englund, “Quantum nanophotonics in diamond,” *JOSA B*, vol. 33, no. 4, pp. B65–B83, 2016.
- [57] I. Aharonovich, S. Castelletto, D. Simpson, C. Su, A. Greentree, and S. Prawer, “Diamond-based single-photon emitters,” *Reports on progress in Physics*, vol. 74, no. 7, p. 076501, 2011.
- [58] S. Tanzilli, A. Martin, F. Kaiser, M. P. De Micheli, O. Alibart, and D. B. Ostrowsky, “On the genesis and evolution of integrated quantum optics,” *Laser & Photonics Reviews*, vol. 6, no. 1, pp. 115–143, 2012.
- [59] M. Bazzan and C. Sada, “Optical waveguides in lithium niobate: Recent developments and applications,” *Applied Physics Reviews*, vol. 2, no. 4, p. 040603, 2015.
- [60] S. Castelletto, B. C. Johnson, and A. Boretti, “Quantum effects in silicon carbide hold promise for novel integrated devices and sensors,” *Advanced Optical Materials*, vol. 1, no. 9, pp. 609–625, 2013.
- [61] S. Castelletto, L. Rosa, and B. C. Johnson, “Silicon carbide for novel quantum technology devices,” in *Advanced Silicon Carbide Devices and Processing*, IntechOpen, 2015.
- [62] J.-M. Liu, *Photonic devices*. Cambridge University Press, 2009.
- [63] V. Van, *Optical microring resonators: theory, techniques, and applications*. CRC Press, 2016.
- [64] A. W. Snyder and J. Love, *Optical waveguide theory*. Springer Science & Business Media, 2012.
- [65] W. V. McLevige, T. Itoh, and R. Mittra, “New waveguide structures for millimeter-wave and optical integrated circuits,” *IEEE Transactions on microwave theory and techniques*, vol. 23, no. 10, pp. 788–794, 1975.

- [66] D. Marcuse, *Theory of dielectric optical waveguides*. Elsevier, 2013.
- [67] R. März, *Integrated optics: design and modeling*. Artech House on Demand, 1995.
- [68] “Optical resonators.” [https://www.rp-photonics.com/optical\\_resonators.html](https://www.rp-photonics.com/optical_resonators.html). Accessed: 2019-04-20.
- [69] “Cavities.” <https://www.rp-photonics.com/cavities.html>. Accessed: 2019-04-20.
- [70] R. Paschotta *et al.*, *Encyclopedia of laser physics and technology*, vol. 1. Wiley-vch Berlin, 2008.
- [71] A. Photonics, “Apss apollo application note on micro ring resonator,” *Apollo Inc. Canadá*, 2003.
- [72] T. Kamalakis and T. Sphicopoulos, “Frequency dependence of the coupling coefficients and resonant frequency detuning in a nanophotonic waveguide-cavity system,” *IEEE journal of quantum electronics*, vol. 42, no. 7/8, p. 827, 2006.
- [73] W. Bogaerts, P. De Heyn, T. Van Vaerenbergh, K. De Vos, S. Kumar Selvaraja, T. Claes, P. Dumon, P. Bienstman, D. Van Thourhout, and R. Baets, “Silicon microring resonators,” *Laser & Photonics Reviews*, vol. 6, no. 1, pp. 47–73, 2012.
- [74] D. G. Rabus and M. Hamacher, “Mmi-coupled ring resonators in gainasp-inp,” *IEEE Photonics Technology Letters*, vol. 13, no. 8, pp. 812–814, 2001.
- [75] T.-J. Wang, C.-H. Chu, and C.-Y. Lin, “Electro-optically tunable microring resonators on lithium niobate,” *Optics letters*, vol. 32, no. 19, pp. 2777–2779, 2007.
- [76] J. Scheuer, G. T. Paloczi, and A. Yariv, “All optically tunable wavelength-selective reflector consisting of coupled polymeric microring resonators,” *Applied Physics Letters*, vol. 87, no. 25, p. 251102, 2005.
- [77] A. Yariv, Y. Xu, R. K. Lee, and A. Scherer, “Coupled-resonator optical waveguide: a proposal and analysis,” *Optics letters*, vol. 24, no. 11, pp. 711–713, 1999.
- [78] J. K. Poon, J. Scheuer, S. Mookherjea, G. T. Paloczi, Y. Huang, and A. Yariv, “Matrix analysis of microring coupled-resonator optical waveguides,” *Optics express*, vol. 12, no. 1, pp. 90–103, 2004.
- [79] F. B. Hildebrand, *Introduction to numerical analysis*. Courier Corporation, 1987.
- [80] J. E. Heebner, P. Chak, S. Pereira, J. E. Sipe, and R. W. Boyd, “Distributed and localized feedback in microresonator sequences for linear and nonlinear optics,” *JOSA B*, vol. 21, no. 10, pp. 1818–1832, 2004.
- [81] F. Xia, L. Sekaric, M. O’Boyle, and Y. Vlasov, “Coupled resonator optical waveguides based on silicon-on-insulator photonic wires,” *Applied physics letters*, vol. 89, no. 4, p. 041122, 2006.

- [82] R. Grover, V. Van, T. Ibrahim, P. Absil, L. Calhoun, F. Johnson, J. Hryniewicz, and P.-T. Ho, "Parallel-cascaded semiconductor microring resonators for high-order and wide-fsr filters," *Journal of Lightwave Technology*, vol. 20, no. 5, p. 872, 2002.
- [83] H. Simos, C. Mesaritakis, D. Alexandropoulos, and D. Syvridis, "Intraband crosstalk properties of add-drop filters based on active microring resonators," *IEEE Photonics Technology Letters*, vol. 19, no. 20, pp. 1649–1651, 2007.
- [84] T. Barwicz, M. A. Popovic, P. T. Rakich, M. R. Watts, H. A. Haus, E. P. Ippen, and H. I. Smith, "Microring-resonator-based add-drop filters in sin: fabrication and analysis," *Optics express*, vol. 12, no. 7, pp. 1437–1442, 2004.
- [85] F. Xia, M. Rooks, L. Sekaric, and Y. Vlasov, "Ultra-compact high order ring resonator filters using submicron silicon photonic wires for on-chip optical interconnects," *Optics express*, vol. 15, no. 19, pp. 11934–11941, 2007.
- [86] V. Van, T. Ibrahim, K. Ritter, P. Absil, F. Johnson, R. Grover, J. Goldhar, and P.-T. Ho, "All-optical nonlinear switching in gaas-algaas microring resonators," *IEEE Photonics Technology Letters*, vol. 14, no. 1, pp. 74–76, 2002.
- [87] B. G. Lee, A. Biberman, N. Sherwood-Droz, C. B. Poitras, M. Lipson, and K. Bergman, "High-speed  $2 \times 2$  switch for multi-wavelength message routing in on-chip silicon photonic networks," in *Optical Communication, 2008. ECOC 2008. 34th European Conference on*, pp. 1–2, IEEE, 2008.
- [88] T. A. Ibrahim, K. Amarnath, L. Kuo, R. Grover, V. Van, and P.-T. Ho, "Photonic logic nor gate based on two symmetric microring resonators," *Optics letters*, vol. 29, no. 23, pp. 2779–2781, 2004.
- [89] J. Scheuer, "Slow propagation of externally injected light pulses in coupled semiconductor laser array," *EPL (Europhysics Letters)*, vol. 77, no. 4, p. 44004, 2007.
- [90] D. Rabus, M. Hamacher, U. Troppenz, and H. Heidrich, "High-q channel-dropping filters using ring resonators with integrated soas," *IEEE Photonics Technology Letters*, vol. 14, no. 10, pp. 1442–1444, 2002.
- [91] V. Van, P. P. Absil, J. Hryniewicz, and P.-T. Ho, "Propagation loss in single-mode gaas-algaas microring resonators: measurement and model," *Journal of Lightwave Technology*, vol. 19, no. 11, p. 1734, 2001.
- [92] M. Chin and S. Ho, "Design and modeling of waveguide-coupled single-mode microring resonators," *Journal of Lightwave Technology*, vol. 16, no. 8, p. 1433, 1998.
- [93] Y. Yanagase, S. Suzuki, Y. Kokubun, and S. T. Chu, "Box-like filter response and expansion of fsr by a vertically triple coupled microring resonator filter," *Journal of Lightwave Technology*, vol. 20, no. 8, p. 1525, 2002.

- [94] S. T. Chu, B. E. Little, W. Pan, T. Kaneko, and Y. Kokubun, “Second-order filter response from parallel coupled glass microring resonators,” *IEEE Photonics Technology Letters*, vol. 11, no. 11, pp. 1426–1428, 1999.
- [95] J. Hohimer, G. Vawter, and D. Craft, “Unidirectional operation in a semiconductor ring diode laser,” *Applied physics letters*, vol. 62, no. 11, pp. 1185–1187, 1993.
- [96] D. Alexandropoulos, J. Scheuer, and N. A. Vainos, “Spectral properties of active racetrack semiconductor structures with intracavity reflections,” *IEEE Journal of Selected Topics in Quantum Electronics*, vol. 15, no. 5, pp. 1420–1426, 2009.
- [97] L. Huang, H. Yan, X. Xu, S. Chakravarty, N. Tang, H. Tian, and R. T. Chen, “Low detection limit sensor based on subwavelength grating racetrack resonator,” in *Nanoscale Imaging, Sensing, and Actuation for Biomedical Applications XIV*, vol. 10077, p. 100770M, International Society for Optics and Photonics, 2017.
- [98] M. F. Limonov, M. V. Rybin, A. N. Poddubny, and Y. S. Kivshar, “Fano resonances in photonics,” *Nature Photonics*, vol. 11, no. 9, p. 543, 2017.
- [99] K.-L. Lee, H.-Y. Hsu, M.-L. You, C.-C. Chang, M.-Y. Pan, X. Shi, K. Ueno, H. Misawa, and P.-K. Wei, “Highly sensitive aluminum-based biosensors using tailorable fano resonances in capped nanostructures,” *Scientific reports*, vol. 7, p. 44104, 2017.
- [100] C. Helmberg, F. Rendl, R. J. Vanderbei, and H. Wolkowicz, “An interior-point method for semidefinite programming,” *SIAM Journal on Optimization*, vol. 6, no. 2, pp. 342–361, 1996.
- [101] R. H. Byrd, M. E. Hribar, and J. Nocedal, “An interior point algorithm for large-scale nonlinear programming,” *SIAM Journal on Optimization*, vol. 9, no. 4, pp. 877–900, 1999.
- [102] P. Venkataraman, *Applied optimization with MATLAB programming*. John Wiley & Sons, 2009.
- [103] C. Lopez, *MATLAB optimization techniques*. Apress, 2014.
- [104] K. Yee, “Numerical solution of initial boundary value problems involving maxwell’s equations in isotropic media,” *IEEE Transactions on antennas and propagation*, vol. 14, no. 3, pp. 302–307, 1966.
- [105] Z. Zhu and T. G. Brown, “Full-vectorial finite-difference analysis of microstructured optical fibers,” *Optics Express*, vol. 10, no. 17, pp. 853–864, 2002.
- [106] J.-P. Berenger, “A perfectly matched layer for the absorption of electromagnetic waves,” *Journal of computational physics*, vol. 114, no. 2, pp. 185–200, 1994.
- [107] A. Taflove and S. C. Hagness, *Computational electrodynamics: the finite-difference time-domain method*. Artech house, 2005.

- [108] S. Guo, F. Wu, S. Albin, H. Tai, and R. S. Rogowski, "Loss and dispersion analysis of microstructured fibers by finite-difference method," *Optics Express*, vol. 12, no. 15, pp. 3341–3352, 2004.
- [109] A. F. Oskooi, D. Roundy, M. Ibanescu, P. Bermel, J. D. Joannopoulos, and S. G. Johnson, "Meep: A flexible free-software package for electromagnetic simulations by the fdtd method," *Computer Physics Communications*, vol. 181, no. 3, pp. 687–702, 2010.
- [110] T. Kamalakis, D. Alexandropoulos, and N. Vainos, "Efficient design of polymer micro-ring resonator filters based on coupled mode theory and finite difference mode solver," *Optics Communications*, vol. 339, pp. 123–128, 2015.
- [111] L. Dogkas, T. Kamalakis, P. Kanakis, and D. Alexandropoulos, "Engineering the spectral properties of non-uniform coupled micro-ring resonator optical filters using numerical optimization," *Journal of Optics*, vol. 19, no. 6, p. 065703, 2017.
- [112] T. Kamalakis and T. Spicopoulos, "An efficient technique for the design of an arrayed-waveguide grating with flat spectral response," *Journal of lightwave technology*, vol. 19, no. 11, pp. 1716–1725, 2001.
- [113] E. A. Marcatili, "Dielectric rectangular waveguide and directional coupler for integrated optics," *Bell System Technical Journal*, vol. 48, no. 7, pp. 2071–2102, 1969.
- [114] T. Kamalakis and T. Spicopoulos, "Analytical expressions for the resonant frequencies and modal fields of finite coupled optical cavity chains," *IEEE journal of quantum electronics*, vol. 41, no. 11, pp. 1419–1425, 2005.
- [115] Ó. G. López, D. Van Thourhout, D. Lasoasa, M. López-Amo, R. Baets, and M. Galarza, "Vertically coupled microring resonators using one epitaxial growth step and single-side lithography," *Optics Express*, vol. 23, no. 4, pp. 5317–5326, 2015.
- [116] P. Girault, N. Lorrain, L. Poffo, M. Guendouz, J. Lemaitre, C. Carré, M. Gadonna, D. Bosc, and G. Vignaud, "Integrated polymer micro-ring resonators for optical sensing applications," *Journal of Applied Physics*, vol. 117, no. 10, p. 104504, 2015.
- [117] K. Oda, N. Takato, and H. Toba, "A wide-fsr waveguide double-ring resonator for optical fdm transmission systems," *Journal of lightwave technology*, vol. 9, no. 6, pp. 728–736, 1991.
- [118] X. Gu, D. Zhu, Y. Zhao, and S. Pan, "Series-coupled double-ring resonators with asymmetric radii for use in channelizer," in *Optoelectronic Devices and Integration V*, vol. 9270, p. 927010, International Society for Optics and Photonics, 2014.
- [119] D. Zhang, Y. Huang, X. Ren, X. Duan, B. Shen, Q. Wang, X. Zhang, and S. Cai, "Add-drop filters based on asymmetric high-order microring resonators," in *Optoelectronic Devices and Integration IV*, vol. 8555, p. 85550U, International Society for Optics and Photonics, 2012.

- [120] K. P. Yap, A. Delâge, J. Lapointe, B. Lamontagne, J. H. Schmid, P. Waldron, B. A. Syrett, and S. Janz, “Correlation of scattering loss, sidewall roughness and waveguide width in silicon-on-insulator (soi) ridge waveguides,” *Journal of Lightwave Technology*, vol. 27, no. 18, pp. 3999–4008, 2009.
- [121] Y. A. Vlasov and S. J. McNab, “Losses in single-mode silicon-on-insulator strip waveguides and bends,” *Optics express*, vol. 12, no. 8, pp. 1622–1631, 2004.
- [122] L. Dogkas, T. Kamalakis, and D. Alexandropoulos, “Analytical model for active racetrack resonators with intracavity reflections and its application in fano resonance tailoring,” *Applied Optics*, vol. 57, no. 17, pp. 4824–4831, 2018.
- [123] L. Dogkas, T. Kamalakis, and D. Alexandropoulos, “Engineering the spectral properties of fano-type resonances in active racetrack-waveguide coupled structures,” *Optics Communications*, vol. 450, pp. 39–47, 2019.
- [124] J. Stewart, *Calculus*. Cengage Learning, 2011.
- [125] A. Salmanpour, S. Mohammadnejad, and P. T. Omran, “All-optical photonic crystal not and or logic gates using nonlinear kerr effect and ring resonators,” *Optical and Quantum Electronics*, vol. 47, no. 12, pp. 3689–3703, 2015.
- [126] P. P. Absil, P. Verheyen, P. De Heyn, M. Pantouvaki, G. Lepage, J. De Coster, and J. Van Campenhout, “Silicon photonics integrated circuits: a manufacturing platform for high density, low power optical i/o’s,” *Optics express*, vol. 23, no. 7, pp. 9369–9378, 2015.
- [127] A. B. Fallahkhair, K. S. Li, and T. E. Murphy, “Vector finite difference modesolver for anisotropic dielectric waveguides,” *Journal of Lightwave Technology*, vol. 26, no. 11, pp. 1423–1431, 2008.
- [128] J. Nocedal and S. Wright, *Numerical optimization*. Springer Science & Business Media, 2006.
- [129] D. Alexandropoulos, H. Simos, S. Mikroulis, and D. Syvridis, “Polarization properties of active semiconductor micro-ring structures,” *Optics Communications*, vol. 281, no. 3, pp. 421–425, 2008.
- [130] A. Kapsalis, I. Stamataki, S. Mikroulis, D. Syvridis, and M. Hamacher, “Widely tunable all-active microring lasers,” *IEEE photonics technology letters*, vol. 18, no. 24, pp. 2641–2643, 2006.
- [131] J. Winn, J. Joannopoulos, S. Johnson, and R. D. Meade, “Photonic crystals: Molding the flow of light,” *Princeton University Press, Princeton, NJ*, vol. 6, pp. 2059–2062, 1995.
- [132] S. J. McNab, N. Moll, and Y. A. Vlasov, “Ultra-low loss photonic integrated circuit with membrane-type photonic crystal waveguides,” *Optics express*, vol. 11, no. 22, pp. 2927–2939, 2003.

- [133] C.-C. Chen, C.-Y. Chen, W.-K. Wang, F.-H. Huang, C.-K. Lin, W.-Y. Chiu, and Y.-J. Chan, "Photonic crystal directional couplers formed by InGaAs nano-rods," *Optics express*, vol. 13, no. 1, pp. 38–43, 2005.
- [134] D.-K. Hwang, B. Lee, and D.-H. Kim, "Efficiency enhancement in solid dye-sensitized solar cell by three-dimensional photonic crystal," *RSC Advances*, vol. 3, no. 9, pp. 3017–3023, 2013.
- [135] S. G. Johnson and J. D. Joannopoulos, "Block-iterative frequency-domain methods for Maxwell's equations in a planewave basis," *Optics express*, vol. 8, no. 3, pp. 173–190, 2001.
- [136] T. Kamalakis, "An GNU-Octave implementation of Jacobi–Davidson style QR method for interior eigenvalue calculations using plane-wave expansion in photonic crystal structures," *Optical and Quantum Electronics*, vol. 50, no. 2, p. 89, 2018.
- [137] P. Kanakis, T. Kamalakis, and T. Sphicopoulos, "Designing slow-light photonic crystal waveguides for four-wave mixing applications," *Optics letters*, vol. 39, no. 4, pp. 884–887, 2014.
- [138] N. S. Ginsberg, S. R. Garner, and L. V. Hau, "Coherent control of optical information with matter wave dynamics," *Nature*, vol. 445, no. 7128, p. 623, 2007.
- [139] M. Lee, M. E. Gehm, and M. A. Neifeld, "Systematic design study of an all-optical delay line based on Brillouin scattering enhanced cascade coupled ring resonators," *Journal of Optics*, vol. 12, no. 10, p. 104012, 2010.
- [140] M. Wan, Y. Song, L. Zhang, and F. Zhou, "Broadband plasmon-induced transparency in terahertz metamaterials via constructive interference of electric and magnetic couplings," *Optics express*, vol. 23, no. 21, pp. 27361–27368, 2015.
- [141] P. Kanakis, T. Kamalakis, and T. Sphicopoulos, "Optimization of the storage capacity of slow light photonic crystal waveguides," *Optics letters*, vol. 37, no. 22, pp. 4585–4587, 2012.
- [142] J. B. Khurgin and R. S. Tucker, *Slow light: Science and applications*. CRC press, 2008.
- [143] K.-I. Ho, M. Boutchich, C.-Y. Su, R. Moreddu, E. S. R. Marianathan, L. Montes, and C.-S. Lai, "A self-aligned high-mobility graphene transistor: Decoupling the channel with fluorographene to reduce scattering," *Advanced Materials*, vol. 27, no. 41, pp. 6519–6525, 2015.
- [144] Z. Li, L. Chen, S. Meng, L. Guo, J. Huang, Y. Liu, W. Wang, and X. Chen, "Field and temperature dependence of intrinsic diamagnetism in graphene: Theory and experiment," *Physical Review B*, vol. 91, no. 9, p. 094429, 2015.
- [145] D. E. Sheehy and J. Schmalian, "Optical transparency of graphene as determined by the fine-structure constant," *Physical Review B*, vol. 80, no. 19, p. 193411, 2009.
- [146] X. Song, J. Hu, and H. Zeng, "Two-dimensional semiconductors: recent progress and future perspectives," *Journal of Materials Chemistry C*, vol. 1, no. 17, pp. 2952–2969, 2013.

- [147] M. A. A. Fiers, T. Van Vaerenbergh, F. Wyffels, D. Verstraeten, B. Schrauwen, J. Dambre, and P. Bienstman, “Nanophotonic reservoir computing with photonic crystal cavities to generate periodic patterns,” *IEEE transactions on neural networks and learning systems*, vol. 25, no. 2, pp. 344–355, 2013.
- [148] F. Denis-Le Coarer, M. Sciamanna, A. Katumba, M. Freiberger, J. Dambre, P. Bienstman, and D. Rontani, “All-optical reservoir computing on a photonic chip using silicon-based ring resonators,” *IEEE Journal of Selected Topics in Quantum Electronics*, vol. 24, no. 6, pp. 1–8, 2018.